https://ntrs.nasa.gov/search.jsp?R=19870009918 2020-03-20T11:13:09+00:00Z

NASA Technical Paper 2667

April 1987

Numerical Simulation of Channel Flow Transition

Resolution Requirements and Structure of the Hairpin Vortex

Steven E. Krist
and Thomas A. Zang

(NASA-TP-2607) NUMERICAL SIMULATION OF CHANNEL FLOW TRANSITION, RESOLUTION REQUIREMENTS AND STRUCTURE OF THE HAIRPIN VORTEX (NASA) 71 p CSCL 01A

N87-19351

Unclas
H1/02 43643

NASA

NASA Technical Paper 2667

1987

Numerical Simulation of Channel Flow Transition

Resolution Requirements and Structure of the Hairpin Vortex

Steven E. Krist
The George Washington University
Joint Institute for Advancement of Flight Sciences
Langley Research Center
Hampton, Virginia

Thomas A. Zang
Langley Research Center
Hampton, Virginia

National Aeronautics and Space Administration

Scientific and Technical Information Branch

Introduction

The instabilities responsible for the first two stages of transition to turbulence in wall-bounded shear flows are now quantitatively well understood. The first, or linear, stage is dominated by slowly growing Tollmien-Schlichting waves propagating in the streamwise direction, and the development of these waves is described quite accurately by the classical linear theory. The landmark experiment of Schubauer and Skramstad (1947) provided the confirmation of Tollmien-Schlichting waves in the Blasius boundary layer. Similar demonstrations for controlled boundary layers and for channel flow have been furnished by Strazisar, Reshotko, and Prahl (1977) and by Nishioka, Asai, and Iida (1980), respectively.

The second stage is characterized by the instability of finite amplitude, streamwise (or two-dimensional) Tollmien-Schlichting waves to infinitesimal, oblique (or three-dimensional) disturbances. Orszag and Patera (1983) and Herbert (1983a, 1983b) have used linear Floquet theory (see, for example, Coddington and Levinson 1955) to model these secondary instabilities. These instabilities induce strong vortical patterns in the boundary layer, the basic element of which is a lambda vortex. A regular pattern develops. It may be either ordered or staggered (see fig. 1). In the former case, the tips of successive lambda vortices are aligned in the streamwise direction of flow, and the distance between the tips corresponds to the streamwise wavelength of the finite amplitude, two-dimensional Tollmien-Schlichting (TS) wave. In the latter case, the tips of successive lambda vortices are offset in the spanwise direction by half the characteristic spanwise scale of the secondary instability. Thus, the streamwise wavelength of the staggered array of vortices is double the wavelength of the two-dimensional TS wave. The ordered pattern is a consequence of a fundamental instability, whereas the staggered pattern results from a subharmonic instability. The fundamental instability is called the K-type instability after Klebanoff, Tidstrom, and Sargent (1962). Craik (1971) and Herbert (1983b) have identified two classes of subharmonic instability, known as the C-type and the H-type, respectively. All three classes have been clearly observed in experiments (Saric, Kozlov, and Levchenko 1984). Floquet theory produces accurate quantitative predictions of the early (linear) development of these three-dimensional secondary instabilities.

Subsequent stages in the transition to turbulence are as yet understood only qualitatively if at all. The lambda vortices rise away from the wall and intensify rapidly into hairpin vortices with attendant highly localized, strong, detached shear layers. These register experimentally as one, then two, then three, etc., spikes in the velocity signals. After roughly the five-spike stage, turbulent spots occur and then fully developed turbulence ensues. Although the instability of a two-dimensional, unsteady, detached shear layer has been modeled qualitatively by Greenspan and Benney (1963), the actual shear layers are decidedly three-dimensional. The detailed flow field structure at these stages is difficult to ascertain experimentally because of the very small spatial scales involved, not only in the turbulent region but also near the sharp flow field gradients connected with the hairpin vortices.

Three-dimensional, nonlinear numerical calculations of the time-dependent Navier-Stokes equations have simulated many important features of transition and turbulence in wall-bounded shear flows. Such simulations have thus far resorted to the parallel flow assumption, in which the spatial growth of the boundary layer is ignored, in order to relax the extreme resolution demands in the streamwise direction that arise for a true, spatially developing flow. Both qualitative and quantitative agreement has been obtained between these full Navier-Stokes calculations and the Floquet theory predictions for the secondary instabilities of the K-type (Orszag and Patera 1983; Kleiser and Schumann 1984; and Spalart 1985) and of the H-Type (Spalart 1985; Zang and Hussaini 1985a; and Laurien 1986). Moreover, Wray and Hussaini (1984) demonstrated that numerical simulations based on the parallel flow assumption achieve good agreement with the detailed flow field structure of the Kovasznay, Komoda, and Vasudeva (1962) K-type boundary-layer experiment up to the two-spike stage. Likewise, Kleiser and Schumann (1984) replicated many salient features of the channel flow experiment of Nishioka, Asai, and Iida (1980).

Even with the parallel flow assumption, neither of these calculations possessed sufficient resolution to track reliably the details of the flow all the way through transition. Both calculations were ceased once the computed solution evinced appreciable oscillations on the scale of the computational grid. The danger, of course, in pushing a calculation beyond its resolution limits is that numerical artifacts may be mistaken for real physical effects. Orszag and Kells (1980) have characterized the artificial oscillations that arise in poorly resolved flows as "numerical turbulence." In problems such as Rayleigh-Bénard flow, for which bifurcation theory is reasonably successful, numerical turbulence may lead one to conclude erroneously that a given flow is chaotic (Curry et al. 1984). In transition problems, it could lead one to

mislocate the instant and region in which turbulence originates.

This paper has two objectives. The first one is to establish firmly, both for this and for subsequent work, the resolution requirements at various stages in the transition process. A single transition simulation is examined in detail. Comparisons are made between second-order finite-difference methods and spectral methods and between calculations made on different grids. The latter comparisons suggest a set of guidelines for when and in which directions grid refinements are required to maintain a physically meaningful calculation.

The second objective is to map out, at the latest stage currently feasible, the structure of the hairpin vortices that arise in K-type and H-type transitions in channel flow. Zang and Hussaini (1985b) have displayed this vortex structure at the one-spike stage for parallel boundary-layer transitions, including a case with wall heating control. Their results agreed with the general features measured by Williams, Fasel and Hama (1984). The focus here is on channel flow, in part to furnish a comparison between the channel and boundary-layer structures, but principally because current spectral numerical algorithms permit more efficient and accurate simulation of channel flow.

This investigation has been conducted for channel flow at a subcritical Reynolds number and at a supercritical Reynolds number. Secondary instabilities of both the K-type (Orszag and Patera 1983) and the H-type (Zang and Hussaini 1985a) have been exhibited under the subcritical conditions.

Although the present work is focused on the hairpin vortices that arise in the transition process, it is also relevant to the vortical structures that have been observed in turbulent boundary layers. Wallace (1982) has noted that the properties of the hairpin vortices in transitional and turbulent boundary-layer flows are similar. Smith (1984) has measured in detail hairpin vortices in turbulent boundary layers. Furthermore, several numerical simulations of turbulent channel flow have mapped out hairpin vortex structures (Moin and Kim 1982; and Moser, Moin, and Leonard 1983).

Formulation

The channel flow geometry is illustrated in figure 2. Lengths are scaled by the channel half-width h, velocities by the centerline velocity u_c, and the density by its constant value. The Reynolds number R is based on these scales; that is, $R = u_c h/\nu$, where ν is the kinematic viscosity. The flow is assumed to be fully developed with the parabolic profile $u_0(Y) = 1 - Y^2$. The incompressible Navier-Stokes equations for the dimensionless variables are used in the form

$$\mathbf{u}_t + \boldsymbol{\omega} \times \mathbf{u} = -\nabla P + \frac{1}{R}\nabla^2 \mathbf{u} \tag{1}$$

$$\nabla \cdot \mathbf{u} = 0 \tag{2}$$

with no-slip boundary conditions at the walls ($Y = \pm 1$) and periodic boundary conditions in X and Z. The velocity vector is denoted by $\mathbf{u}$, the vorticity $\boldsymbol{\omega} = \nabla \times \mathbf{u}$, and the total pressure $P = p + \frac{1}{2}|\mathbf{u}|^2$, where p is the static pressure.

Two related numerical methods have been used to obtain the results reported herein. Both use a Fourier collocation technique for the spatial discretization in the X- and Z-directions. One uses a second-order finite-difference scheme in Y, and the other uses Chebyshev collocation for that direction. The Fourier finite-difference method (FFDM) was devised by Moin and Kim (1982) for their large-eddy simulation and was used by Biringen (1984) for his transition calculations. The particular Fourier-Chebyshev method (FCBM) used here is the one developed by Zang and Hussaini (1986). The FCBM code uses the standard Chebyshev grid in Y, whereas the FFDM code uses the hyperbolic tangent transformation,

$$Y = \frac{1}{a}\tanh\left(\xi \tanh^{-1} a\right) \tag{3}$$

The computational variable $\xi \in [-1, 1]$, and the stretching parameter $a = 0.94175$ is used. Both methods employ an explicit time discretization for the advection and horizontal diffusion terms and an implicit time discretization for the vertical diffusion and pressure gradient terms as well as the continuity equation. The FCBM uses a splitting, or fractional step, technique for the time advancement: in the first half-step the advection and diffusion terms are accounted for, and in the second half-step a pressure correction is applied so that the final velocity field is divergence free. Boundary conditions are applied at the intermediate step to all three velocity components and for the pressure correction to the normal velocity component. The FFDM is unsplit; that is, all terms are accounted for simultaneously in a single step. Both codes employ a staggered grid for the pressure so that no artificial boundary conditions are required.

There are at least five other fully spectral algorithms for channel flow simulation—see Orszag and Kells (1980), Kleiser and Schumann (1984), Moin and Kim (1980), Moser, Moin, and Leonard (1983), and Zang and Hussaini (1985a). Only the first of these resorts to splitting. Zang and Hussaini's

(1985a) method is the unsplit counterpart to the FCBM used in the present work. The split FCBM code is more robust and requires less storage and CPU time than the unsplit code. Zang and Hussaini (1986) have confirmed that when appropriate intermediate boundary conditions are employed, the split FCBM code gives the same results (to at least four significant digits) as the unsplit version under the precise physical conditions simulated in the present work.

In these algorithms, both physical space and spectral space representations of the dependent variables are employed. The velocity has the Fourier series representation,

$$\mathbf{u}(X,Y,Z,t) = \sum_{\hat{k}_x=-N_x/2}^{N_x/2-1} \sum_{\hat{k}_z=-N_z/2}^{N_z/2-1} \hat{\mathbf{u}}_{\hat{k}_x,\hat{k}_z}(Y,t) \times e^{i\left[\left(\hat{k}_x/s_x\right)\alpha X+\left(\hat{k}_z/s_z\right)\beta Z\right]} \quad (4)$$

where α and β are the fundamental wave numbers in the streamwise and spanwise directions, respectively, and s_x and s_z denote the number of subharmonic modes which are included in these directions. The fundamental wavelengths in the X- and Z-directions are $L_x = 2\pi/\alpha$ and $L_z = 2\pi/\beta$, and the computational domains have lengths s_xL_x and s_zL_z. The individual Fourier modes are labeled by (k_x, k_z), where $k_x = \hat{k}_x/s_x$ and $k_z = \hat{k}_z/s_z$. Several of these Fourier components are illustrated in figure 3.

The initial conditions for the simulations reported in this work consist of the mean flow plus a two-dimensional TS wave and two oblique three-dimensional waves:

$$\begin{aligned}\mathbf{u}(X,Y,Z,0) = \mathrm{Re}\Big\{ & \mathbf{u}_0(Y) + \epsilon_{2D}\mathbf{u}_{2D}(Y)e^{i\alpha X} \\ & + \frac{1}{2}\epsilon_{3D}\mathbf{u}^+_{3D}(Y)e^{i[(\alpha/s_x)X+\beta Z]} \\ & + \frac{1}{2}\epsilon_{3D}\mathbf{u}^-_{3D}(Y)e^{i[(\alpha/s_x)X-\beta Z]}\Big\} \quad (5)\end{aligned}$$

where $\mathbf{u}_{2D}(Y)$ and $\mathbf{u}^{\pm}_{3D}(Y)$ are the least stable linear modes for the given real wave numbers α and β. These eigenfunctions are normalized so that their maximum streamwise amplitudes are 1. Thus, ϵ_{2D} and ϵ_{3D} measure the amplitudes of the initial streamwise velocity perturbations. For the K-type transition simulation the three-dimensional waves are TS waves and $s_x = 1$, whereas for the H-type transition the three-dimensional waves are Squire modes, that is, eigensolutions of the homogeneous vertical vorticity equation, and $s_x = 2$.

A useful measure of the strength of a given Fourier harmonic is the quantity

$$E_{k_x,k_z}(t) = \frac{15}{16}d_{k_x}d_{k_z}\int_{-1}^{1}|\hat{\mathbf{u}}_{k_x,k_z}(Y,t)|^2\,dY \quad (6)$$

where

$$d_k = 2 - \delta_{k,0}$$

This quantity is the kinetic energy of the mode normalized by the kinetic energy of the mean flow.

Similarly, the velocity has the Chebyshev series representation,

$$\mathbf{u}(X,Y,Z,t) = \sum_{n=0}^{N_y}\tilde{\mathbf{u}}_n(X,Z,t)T_n(Y) \quad (7)$$

where $T_n(Y)$ is the Chebyshev polynomial of degree n. The significance of these modes is measured by

$$E_n(t) = \frac{15}{16s_xL_xs_zL_z}\int_0^{s_xL_x}\int_0^{s_zL_z}|\tilde{\mathbf{u}}_n(X,Z,t)|^2\,dX\,dZ \quad (8)$$

The calculations were performed in 32-bit arithmetic on the Control Data Corporation VPS 32 at NASA Langley Research Center. The FFDM calculations took 0.65 sec per step on a $32 \times 50 \times 32$ grid and 2.5 sec per step on a $32 \times 200 \times 32$ grid. The FCBM code requires 0.96 sec per step on a $32 \times 64 \times 32$ grid and 2.7 sec, 7.50 sec, and 15.5 sec per step on 64^3, 96^3, and 128^3 grids, respectively. The largest grid used in the calculations reported here was $96 \times 128 \times 216$. This consumed 20.1 sec per time step.

Resolution Study

The particular subcritical K-type transition studied by Biringen (1984) is used here to illustrate the resolution demands of transition simulations. The Reynolds number is 1500. The horizontal wave numbers α and β are both unity. No subharmonics are included ($s_x = s_z = 1$). The temporal frequencies of the least rapidly damped modes are $\omega_{2D} = 0.326299 - 0.028206i$ and $\omega_{3D} = 0.401293 - 0.028230i$, as determined by a Chebyshev tau approximation to the Orr-Sommerfeld equation (Orszag 1971b). The initial amplitudes of the waves are $\epsilon_{2D} = 0.11$ and $\epsilon_{3D} = 0.10$. The primary two-dimensional wave has the period $T = 19.26$. The numerical computations are made in a frame with a streamwise velocity of 0.36. This is the average of the phase speeds of the two- and three-dimensional waves. The use of a moving frame improves the temporal accuracy of the calculation.

A straightforward test of the vertical resolution is the ability of a code to reproduce the time evolution of a linear eigenfunction. The computed growth rates and their errors at $t = 30$ are given in table I for several calculations. The initial condition for each case consisted of a three-dimensional TS wave at 0.01-percent amplitude. The Chebyshev calculation is accurate to better than five significant digits. The finite-difference calculations exhibit the expected second-order accuracy. Moreover, the finite-difference calculations are on the side of excessive damping of the wave. (This same effect was found by Malik, Zang, and Hussaini (1985) for a higher Reynolds number.)

The error in the $32 \times 50 \times 32$ FFDM growth rate might appear to be small. Nevertheless, it indicates uncomfortably large errors in the full transition simulation. These manifest themselves quite clearly in the time-dependent vortical flow field. Since the vorticity is obtained from the primitive variables by differentiation, it is a sensitive indicator of errors in the velocities themselves. Typical vorticity patterns are given in figure 4,[1] which shows the full three-dimensional fields in the lower half of the channel. (The features in the upper half are similar, but are displaced in X by $L_x/2$.) These color plots show the streamwise ($\omega_x = \partial w/\partial Y - \partial v/\partial Z$) and spanwise ($\omega_z = \partial v/\partial X - \partial u/\partial Y$) vorticity components in terms of two level surfaces each. To improve perception, the surfaces have been shaded to mimic the effect of light sources. Most of the hairpin vortex is traced out by the uppermost red-blue pair of surfaces in the ω_x plot. The tip, of course, is missing because ω_x vanishes there. The peak plane is the center of the spanwise (Z) direction. It lies between the two legs of the hairpin vortex. The uppermost surface in the ω_z plot is in the region of the detached shear layer. Note that in the spanwise direction, this shear layer is confined to the vicinity of the peak plane. For this resolution study, we focus on contour plots of a few key cross sections, including the peak plane ($Z = \pi$).

Errors in the $32 \times 50 \times 32$ FFDM calculation are reflected by oscillations in the contours of vertical shear ($\partial u/\partial Y$) in the peak plane even at the early time $t = 7.5$. These contours are plotted in figure 5, and the results from a $32 \times 200 \times 32$ calculation are given for comparison. The coarse grid results are already exhibiting the grid-scale oscillations which, in what is still laminar flow, are indicative of inadequate resolution. Figures 6 and 7 furnish a similar comparison at $t = 15$. The coarse grid result not only fails to pick up the full intensity of the detached shear layer but also misrepresents its speed. The fine grid result places the center of the shear layer at $X \approx 0.55L_x$, whereas it has reached only $X \approx 0.45L_x$ in the coarse grid calculation.

These figures also include a (Z-Y) contour plot of the streamwise vorticity (ω_x) at a streamwise station near the maximum of this vorticity component (roughly 1/2 of the distance along the x-axis at $t = 15$). (The features corresponding to the lambda-hairpin vortex are those whose centers are near $Y = -0.625$.) The vertical shear plots are indicative of the resolution in X and Y, whereas the streamwise vorticity plots highlight the Y and Z resolution. Even for the fine vertical grid FFDM calculations, there are noticeable oscillations in the streamwise vorticity. These are removed with increased spanwise resolution, as is demonstrated below.

The fully spectral FCBM result on a $32 \times 64 \times 32$ grid at $t = 15$ is given in the top half of figure 8. It agrees well with the $32 \times 200 \times 32$ FFDM result. The vertical shear plots differ only near the center of the detached shear layer, and the FFDM streamwise vorticity plots are slightly more oscillatory. Thus, the poor results of the $32 \times 50 \times 32$ FFDM calculation at $t = 7.5$ and $t = 15$ are due primarily to inadequate resolution in the vertical direction and not to any flaw in the code itself.

The results in the bottom half of figure 8 are for $t = 18.75$. The spanwise fluctuations in the streamwise vorticity have the unmistakable signature of a grid-scale oscillation with wavelength $2\Delta Z$. They evidently arise because the number of points in this direction is insufficient to resolve the sharp gradients in the vortex loop.

As is illustrated in figure 9, a 64^3 FCBM calculation eliminates the oscillations at $t = 15$, but is still too coarse at $t = 18.75$. Note the shorter scale (compared with fig. 8) of the fluctuations in the streamwise vorticity; it corresponds to the smaller spacing in Z.

After $t = 15$, the resolution demands increase rapidly. The results at $t = 18.75$ and 22.50 from a properly resolved calculation are displayed in figure 10. The computed flow field displays no grid-scale oscillations at these times. These results were obtained from a calculation on a 64^3 grid until $t = 15$; then the grid was refined to 96^3, refined further to $96 \times 128 \times 128$ at $t = 16.88$, refined yet again to $96 \times 128 \times 162$ at $t = 18.28$, refined to $96 \times 128 \times 192$ at $t = 19.22$, and refined to $96 \times 128 \times 216$ at $t = 21.10$. The grid was refined by Fourier-Chebyshev interpolation of the primitive variables from the coarser grid onto the finer one.

[1] The authors are grateful to Robert Weston, Langley Research Center, for supplying the three-dimensional color figures.

The Fourier-Chebyshev coefficients of the solution reveal when additional resolution is required. We used the quantities $E_{k_x}(t) = \max_{k_z} E_{k_x,k_z}(t), E_n(t)$, and $E_{k_z}(t) = \max_{k_x} E_{k_x,k_z}(t)$ to assess the resolution requirements in the X-, Y-, and Z-directions, respectively. Several such energy spectra are furnished in figure 11. The circles labeled X, for example, are a plot of E_{k_x} as a function of the streamwise mode k_x. Of these examples, only the 64^3 grid results at $t = 18.75$ represent an inadequately resolved calculation. The tail of the spanwise spectrum is only four orders of magnitude lower than the fundamental mode. This corresponds to a truncation error in the velocities themselves on the order of 1 percent. The consequences are clearly apparent in figure 9. In this instance, the resolution in Y is also inadequate, with truncation errors on the order of 0.1 percent. In no other case shown in figure 11 does the truncation error exceed 0.01 percent, that is, an eight-order-of-magnitude drop in the energy. These computations were performed in 32-bit arithmetic. Hence, one should expect no better than five-digit accuracy.

The grid refinements cited above were performed when the tail of the energy spectrum in any direction reached the 10^{-11} to 10^{-12} level. Moreover, refinements were performed in only those directions with spectral tails this large. For this transition simulation, the spanwise direction is clearly the most demanding because of the narrow spanwise dimensions of the vortex loop near its tip.

The $32 \times 50 \times 32$ FFDM results for $t = 22.5$ are presented in figure 12. Very little of the structure of the detached shear layer has been retained. The streamwise vorticity plot indicates why this computed flow field deserves to be characterized as "numerical turbulence".

Figure 13 gives the time evolution of several Fourier harmonics in the two FFDM calculations. The coarse grid fails to capture the full strength of the secondary instability, the principal component of which is the (1,1) mode. This is consistent with the earlier result for linear modes that the coarse grid calculation damped these modes excessively. Note that the energy contained in the (1,1) mode rises noticeably less rapidly in the coarse grid simulations.

The figures given in this section make it apparent that the use of a coarse finite-difference method in the vertical direction instead of either a fine-grid finite-difference method or a Chebyshev method produces results that differ visibly from the correct solution. Moreover, inadequate resolution in the Fourier directions clearly leads to numerical turbulence.

The $32 \times 50 \times 32$ FFDM calculation was performed to furnish a direct comparison of the present, highly resolved simulation with the results of Biringen (1984). He continued his simulation on this coarse grid all the way to $t = 80$. The results presented here indicate that nonphysical, numerical effects already invalidate such a calculation by $t = 20$.

We close this section with some comments on aliasing. Most reported transition calculations have been de-aliased, at least in the horizontal directions. (The only exceptions appear to be the results of Marcus (1984) and of Zang and Hussaini (1985a, 1985b).) Yet those rigorous numerical analysis results which are presently available all suggest that de-aliasing is not necessary. (Of course, the differential equations must be used in a form which guarantees conservation of some quadratic integral in ideal flow.) For a time-dependent, one-dimensional, linear model problem, Kriess and Oliger (1979) have shown that the aliasing error is of the same order as the truncation error. More importantly, Maday and Quarteroni (1982) have proven that aliased and de-aliased Fourier spectral approximations to the steady, three-dimensional, fully periodic Navier-Stokes equations have the same asymptotic rate of convergence. Our conclusion is that if aliasing is a problem, then the resolution of the calculation is marginal anyhow.

This conclusion is supported by the results given in figure 14 for a horizontally de-aliased version of the FCBM calculation on a $48 \times 64 \times 48$ grid. The highest 16 modes in each direction were forced to zero after every time step. This removes horizontal aliasing interactions (Orszag 1971a). The results here at $t = 15$ are slightly better than the corresponding results in figure 8. The de-aliased results at $t = 18.75$ are not reliable, but this is a problem of resolution. Figure 15 compares the resolution at $t = 15$.

All our experience with respect to de-aliasing of transition calculations may be summarized as follows: Both aliased and de-aliased calculations are valid until they lose resolution; the aliased calculation loses resolution slightly sooner than a de-aliased calculation with an equal number of active modes.

This experience is contrary to several opinions which are cited in the literature. The work of Schamel and Elsässer (1976) is frequently invoked by those averse to aliased calculations. We have repeated one of their examples (the Korteweg–de Vries equation) and do not reproduce their results. In fact, we find virtually no difference between the aliased and de-aliased results. Moreover, Fornberg and Whitham (1978) experienced no difficulty with aliased calculations of the Korteweg–de Vries equation. Moser, Moin, and Leonard (1983) claimed that

aliased calculations of Taylor-Couette flow give unacceptable results. However, the only conclusion that is warranted by their numerical examples is that a well-resolved de-aliased calculation is superior to a poorly resolved aliased calculation. (Their poorly resolved de-aliased calculation is just as bad as their single, poorly resolved aliased calculation.) Of course, Marcus (1984) performed aliased calculations for this problem with no discernible difficulty.

Hairpin Vortex Structure

This section is devoted to the detailed structure of the hairpin vortex. This is the principal (unsteady) intermediate state between the emergence of the lambda vortices and the first turbulent activity in the transition process. Numerical simulations have been performed at the supercritical Reynolds number of 8000 as well as at the subcritical Reynolds number of 1500. Both K- and H-type transitions have been computed. In all cases, the fundamental wave numbers α and β were unity. Table II lists the temporal eigenfrequencies of the least stable two-dimensional TS wave, three-dimensional TS wave, and subharmonic Squire mode under these conditions.

For each calculation, the grid was refined as needed to maintain a truncation error of less than 0.01 percent in the primitive variables. Some additional information on the vertical resolution is provided in table III. It lists the location of the (bottom) critical layer of the two-dimensional TS wave and the edge of viscous sublayer as estimated by $Y_\nu = -1 + 5Y_w$, where $Y_w = \nu/u_\tau = 1/\sqrt{2R}$ for the unperturbed laminar flow. The wall friction velocity u_τ is $\sqrt{\nu\, \partial u_0/\partial Y}$. The number of points between the wall and the critical layer is N_c; hence, N_c/N_y denotes the fraction of the vertical grid in this region. For the viscous sublayer, N_ν is defined similarly.

K-Type Vortex at $R = 1500$

Subcritical K-type transition at $R = 1500$ was discussed at length in the preceding section. The initial TS wave amplitudes were $\epsilon_{2D} = 0.11$ and $\epsilon_{3D} = 0.10$. These initial amplitudes, chosen to match those of Biringen (1984), are certainly quite large. However, at this low Reynolds number they need to be this large in order to trigger the formation of a hairpin vortex.

The time history of the kinetic energy in the lowest Fourier harmonics is indicated in figure 16. In the early stages ($t \leq 5$), the two- and three-dimensional TS waves decay linearly. Meanwhile, the flow field develops appreciable higher order components which are generated by nonlinear effects. The secondary instability is evident in the subsequent growth of the (1,1) mode. By $t = 18.75$, the flow has achieved the state illustrated in figure 4. This highly developed hairpin vortex (the two upper surfaces in fig. 4(a)) has evolved far past the stage which can be modeled by Floquet theory.

Although three-dimensional plots such as figure 4 readily depict the general flow field features, they are not capable of conveying detailed information. For this, we must resort to a collection of two-dimensional cross sections. The vertical shear and the perturbation velocities in the peak plane are displayed in figures 17 and 18. The velocity vectors are shown, for clarity, at only a subset of the computational grid. The full channel is displayed in figure 18 to illustrate the degree to which the shear layers in the two halves of the channel are interacting. By these late times, distinct kinks have developed in the shear layer. Some streamwise velocity profiles are given in figure 19. The detached shear layers clearly correspond to inflectional velocity profiles. Williams, Fasel, and Hama (1984) have argued that this shear is created as the fluid surrounding the hairpin vortex moves up and over it.

The evolution of the vertical shear is similar until $t = 22.5$ to that reported by Kovasznay, Komoda, and Vasudeva (1962) for controlled transition in a boundary layer. At about $t = 22.5$ (fig. 18), the shear layers which originate at the bottom and the top of the channel begin to overlap. This process does not occur in controlled transition in the boundary layer or in the channel at higher Reynolds numbers.

Figures 20 to 23 present detailed information on the hairpin vortex at $t = 18.75$. Its shape is most apparent in the plots of streamwise vorticity (fig. 20(a)). Solid lines denote fluid rotating clockwise, and dashed lines denote fluid rotating counterclockwise. The legs of the vortex appear to emerge near $X/L_x = 1/8$ in the vicinity of the critical layer of the two-dimensional TS wave. Since the spanwise direction has been compressed by a factor of 4.19 in these plots, the legs of the vortex are even flatter than they appear in figure 20(a). As X increases, the vortex becomes less flat, lifts away from the wall, and pinches toward the peak plane.

Two regions of enhanced spanwise vorticity (fig. 20(b)) can be identified: the detached shear layer, which is just above the tip of the hairpin vortex, and the region between the legs of the vortex and the wall. There is also a local minimum in the (absolute value of the) spanwise vorticity just underneath the detached shear layer. Thus, the hairpin vortex is characterized by a region of large streamwise vorticity and small spanwise vorticity. These are the same general features which were measured by Williams, Fasel, and Hama (1984) and observed numerically by

Zang and Hussaini (1985b) for the controlled boundary layer.

Figure 21, which displays velocity vectors in Y-Z cross sections, reinforces the picture of the hairpin vortex suggested by figure 20. Figure 22 does the same. It presents contour plots of the helicity, defined by

$$h = \mathbf{u} \cdot \boldsymbol{\omega} \tag{9}$$

Helicity has been proposed as one indication of coherent structures in turbulent flows (Levich and Tsinober 1983). (The universality of this has, however, been criticized by Speziale (1987) on the grounds that helicity is not a Galilean invariant quantity.) This quantity provides a less cluttered picture of the streamwise vorticity.

The effects of vortex stretching and diffusion are illustrated in figure 23. The equations of motion imply that

$$\frac{d}{dt}\int \tfrac{1}{2}|\omega|^2\,dV = \int \omega \cdot (\omega \cdot \nabla \mathbf{u})\,dV + \int -\nu \nabla\omega : \nabla\omega\,dV + \int \tfrac{1}{2}\nu \frac{\partial}{\partial n}|\omega|^2\,dS \tag{10}$$

The integrand of the first term on the right side measures the rate of vortex stretching and the second term measures the rate of vorticity diffusion. The surface integral accounts for the generation of vorticity at the walls. The first two integrands are plotted in figures 23(a) and 23(b). The most rapid stretching is clearly associated with the regions of most intense spanwise vorticity, while the diffusion is most significant at the edges of these regions. The net change in vorticity is dominated by stretching effects.

Figures 24 to 26 supply the vorticity contours at $t = 15$, 22.5, and 25.0. Together with figure 20, they provide a time history of the hairpin vortex and the detached shear layer. At all four of these times, the shear layer does indeed lie immediately above the vortex tip. Hence, it may be used to estimate the speed at which the vortex is traveling in the streamwise direction. Table IV summarizes information extracted from figures 17 and 18. The location of the shear layer in the peak plane is denoted by $(X_{\mathrm{SL}}, Y_{\mathrm{SL}})$. They are the coordinates of the center of the shear layer. The shear layer speed u_{SL} is calculated from this information, after taking into account the speed at which the coordinate system itself is moving (0.36 in this case). The speed of the unperturbed mean flow at the height of the shear layer is given for reference. The vortex moves faster as it rises away from the wall and slows down after it crosses the center of the channel. It is indeed moving slower than the surrounding fluid, as suggested by Williams, Fasel, and Hama (1984).

By $t = 22.5$, (fig. 25) a counterrotating vortex has emerged inside the hairpin vortex. At $X/L_x = 1/2$ and 3/4 the spanwise vorticity inside the neck of the hairpin vortex is so small that the streamwise vorticity is dominant. Hence, this is a second region, in addition to the hairpin vortex itself, where the streamwise vorticity is large and the spanwise vorticity is small. This feature is still present at $t = 25$. At this stage, it appears that the neck of the hairpin vortex is in the process of splitting into two parts. The appendix contains additional data on the flow field at these times.

H-Type Vortex at $R = 1500$

The initial conditions for the H-type transition at $R = 1500$ again were $\epsilon_{2D} = 0.11$ and $\epsilon_{3D} = 0.10$, but the three-dimensional wave was the subharmonic Squire mode (with $s_x = 2$). The simulation started on a $64 \times 64 \times 32$ grid and was refined as needed—by $t = 32.5$, a $96 \times 96 \times 162$ grid was in use.

The energy history is provided in figure 27. The initial three-dimensional wave is denoted by (1/2,1), indicating that its streamwise wave number is only half that of the two-dimensional TS wave. Both modes decay linearly in the early stages, but by $t = 8$ the secondary instability has asserted itself and is reflected by the growth of the (1/2,1) mode.

The structure at $t = 30$ is typical of the later stages. Figure 28 gives a three-dimensional picture of the vorticity. The vortices are, of course, arranged in the familiar staggered pattern. The vertical shear in a peak (and one other) plane is given in figure 29. This shear layer is roughly equal in strength and height to the K-type one at $t = 15$. (Note that the X-axis has been compressed by a factor of 2 relative to the K-type plots.) Vorticity contours are provided in figure 30. The structures here are similar to those for the K-type vortex, albeit more complicated due to the substantial interference effects of neighboring vortices. Helicity, stretching, and diffusion contours are supplied in the appendix.

The hairpin vortex evolves much less rapidly for the subharmonic instability than for the fundamental one. The vorticity structure is qualitatively similar and only slightly more intense at $t = 40$ than at $t = 30$. The K-type vortex, however, undergoes a very rapid evolution between $t = 15$ and $t = 25$. Indeed, the relative weakness of the subharmonic vortex system is responsible for its less stringent resolution requirements.

K-Type Vortex at $R = 8000$

The next two simulations were performed under conditions much closer to those of actual transition—the Reynolds number was supercritical ($R = 8000$),

the initial two-dimensional TS wave began at the 2-percent level and the initial three-dimensional wave had the very low amplitude of 0.02 percent. The resolution requirements, especially in the normal direction, were more severe at the higher Reynolds number. Hence, the simulations were carried to a less advanced state than those for $R = 1500$.

The harmonic energy history of the K-type transition is furnished in figure 31. This simulation was conducted for more than seven periods of the two-dimensional TS wave. For at least the first six periods ($t \leq 153$), the growth of the two-dimensional wave is described very well by linear theory. The secondary instability induces the growth of the three-dimensional wave after one period, but because of the low initial amplitude of the three-dimensional disturbance, the hairpin vortex does not emerge until roughly 6 1/2 periods ($t > 165$). The subsequent evolution is extremely rapid. The simulation was halted at $t = 182.21$ (7 1/6 periods) when the $72 \times 162 \times 192$ grid had just become inadequate.

Several illustrations of the resulting structure at $t = 182.21$ are provided here in figures 32 and 33. A comparison of figure 32 with figure 17 and of figure 33 with figures 20, 24, 25, and 26 suggests that the $t = 18.75$ state of the low Reynolds number vortex is the closest match to the $R = 8000$ vortex. (In comparing these figures, note that the $R = 8000$ vortex is shifted forward by $1/8\ L_x$ in the streamwise direction.)

Clearly, the only substantial difference between these two vortices are in scale and intensity. The $R = 8000$ structures are narrower and closer to the wall. Despite streamwise velocity perturbations which are 20 percent smaller, the detached shear layer is 100 percent more intense for $R = 8000$ than for $R = 1500$. This is a result of larger gradients at the higher Reynolds number. The streamwise vorticities for the two cases, however, have comparable amplitudes. Helicity and vortex stretching plots are supplied in the appendix.

H-Type Vortex at $R = 8000$

The harmonic energy history of the H-type transition at $R = 8000$ is supplied in figure 34. Like its $R = 1500$ counterpart, the instability is slightly weaker than the K-type secondary instability, judged by the rate at which grid refinements were required. This simulation was halted at $t = 186.45$ (7 1/3 periods). The final grid was $64 \times 128 \times 128$.

The structure of this vortex is illustrated in figures 35 and 36. It resembles its lower Reynolds number counterpart in all essential respects but one: the vortices are less intertwined at $R = 8000$.

Discussion

The structure of the hairpin vortex is difficult to resolve, even at low Reynolds numbers. A detailed description of the resolution requirements of one case was reported at length in an earlier section. These results, and similar studies for the other three cases, lead us to the following conclusions. (1) The streamwise direction requires by far the least resolution. Only in the later stages of transition, when the detached shear layer develops kinks, does high resolution in this direction become necessary. (2) Even at low Reynolds number, the spanwise direction is very demanding. (3) The resolution in the vertical direction is the most sensitive to Reynolds number. (4) A grid refinement is needed in any direction when the tail of the energy spectrum reaches 10^{-8} of the low-frequency value.

These remarks are buttressed by figure 37, which presents resolution plots for each of the four simulations at the last stages reported here. The only case with substantial high-frequency content in the X-direction is the $R = 1500$, K-type vortex at $t = 25$. This is the only simulation in which there are at least two streamwise kinks. At the slightly earlier time of $t = 22.5$, the second kink is absent and so is the streamwise high-frequency content (fig. 11). The high spanwise resolution is needed because of the sharp gradient and complex structures which develop at the tip of the vortex.

The difficulties presented by higher Reynolds number calculations are exemplified by the $R = 8000$, K-type vortex. The vertical frequency spectrum (fig. 37) has a very long tail at $t = 182.21$. In fact, this direction fails the eight-decade guideline. Indeed, this marginal lack of resolution is responsible for the oscillations in the 0.2 vertical shear contour underneath the detached shear layer in figure 32. These calculations were all performed on standard Chebyshev grids ($Y_j = -\cos(\pi j/N_y)$, $j = 0, 1, \ldots, N_y$). Numerical simulations such as these would surely benefit from a more highly tuned vertical grid. A mapping can be readily incorporated into both spectral algorithms used for these calculations (Zang and Hussaini 1985a and 1986) for at most a 50-percent increase in running time. Mappings do, however, make algorithms which rely on direct solution techniques for special basis functions (Moser, Moin, and Leonard 1983) impractical. Moreover, they necessitate the more expensive matrix diagonalization versions of the Orszag-Kells (1980) and Kleiser-Schumann (1984) methods.

Another useful modification to the algorithm would involve using a nonuniform grid in the Z-direction that clustered the points near the peak

plane. This would complicate the solution of the implicit equations for pressure and for normal diffusion. The spectral multigrid approach suggested by Zang and Hussaini (1986) would be able to handle this complication.

The K- and H-type transitions produce similar hairpin vortices, although the K-type vortices appear to be more intense. Conceivably, the H-type vortices are stronger at different spanwise wave numbers.

The vortices which arise at higher Reynolds numbers are less diffuse and closer to the wall than those at lower Reynolds numbers. Vortex stretching effects predominate over vortex diffusion in most of the hairpin vortex. The streamwise and spanwise vorticity patterns conform to the large-scale measurements of Williams, Fasel, and Hama (1984) for a K-type boundary-layer transition. Examination of the vorticity patterns displayed in this report reveals that the detached shear layer is in fact two separate shear layers above the legs of the vortex which merge into a single shear layer above the vortex tip.

The most surprising result was the robustness of the time-dependent hairpin vortex. None of the transitional flows simulated here became turbulent before all the available resolution (nearly 3 million grid points) was exhausted. There were no signs of violent inflectional instabilities emanating from the detached shear layer. (Several additional runs of the $R = 1500$, K-type vortex included a random component in the initial velocity field. These were damped very rapidly by the high viscosity of this flow. Even for an initial streamwise root-mean-square amplitude of 0.2 percent, these fluctuations decayed so much that by $t = 18.75$ they could no longer be detected in flow-field plots. Evidently larger amplitudes and higher Reynolds numbers are required for these instabilities to occur.) Seemingly chaotic behavior was achievable only by resorting to an obviously inadequate grid.

NASA Langley Research Center
Hampton, VA 23665-5225
December 18, 1986

Appendix

Supplementary Illustrations

This appendix is directed toward those interested in additional details from these four simulations.

Figures 38 to 43 pertain to the $R = 1500$, K-type transition. The first three present a more complete picture of the vorticity fields at $t = 15$, 22.5, and 25. The last case is especially complex. Figure 41 contains cross-stream velocity vectors at $t = 22.5$. The last four frames indicate that the hairpin vortex actually dips back down to the wall (near $X/L_x = 5/8$) just before the tip. Figure 42 presents the helicity at $t = 22.5$. Figure 43 supplies not only the vortex stretching and diffusion rates at $t = 22.5$ but also their sum. (Because of the intensity of the stretching, the contours in the most intense regions have been omitted.) The net change of vorticity is conveyed by the last part of figure 43. Note that between $X/L_x = 0$ and $X/L_x = 1/2$, there is a substantial region along the wall in which there is a net decrease of vorticity. Elsewhere, however, vortex stretching dominates the diffusion effects.

Figures 44 to 49 are self-explanatory and pertain to the other three simulations. Vortex diffusion plots have not been supplied for the $R = 8000$ cases because of plotting difficulties arising from very large gradients near the wall.

References

Biringen, S. 1984: Final Stages of Transition to Turbulence in Plane Channel Flow. *J. Fluid Mech.*, vol. 148, Nov., pp. 413–442.

Coddington, Earl A.; and Levinson, Norman 1955: *Theory of Ordinary Differential Equations.* McGraw-Hill Book Co.

Craik, Alex D. D. 1971: Non-Linear Resonant Instability in Boundary Layers. *J. Fluid Mech.*, vol. 50, pt. 2, Nov. 29, pp. 393–413.

Curry, James H.; Herring, Jackson R.; Loncaric, Josip; and Orszag, Steven A. 1984: Order and Disorder in Two- and Three-Dimensional Bénard Convection. *J. Fluid Mech.*, vol. 147, Oct., pp. 1–38.

Fornberg, B.; and Whitham, G. B. 1978: A Numerical and Theoretical Study of Certain Nonlinear Wave Phenomena. *Philos. Trans. R. Soc. London*, ser. A, vol. 289, no. 1361, May 2, pp. 373–404.

Greenspan, H. P.; and Benney, D. J. 1963: On Shear-Layer Instability, Breakdown and Transition. *J. Fluid Mech.*, vol. 15, pt. 1, Jan., pp. 133–153.

Herbert, Thorwald 1983a: Stability of Plane Poiseuille Flow—Theory and Experiment. *Fluid Dyn. Trans.*, vol. 11, pp. 77–126.

Herbert, Thorwald 1983b: Secondary Instability of Plane Channel Flow to Subharmonic Three-Dimensional Disturbances. *Phys. Fluids*, vol. 26, no. 4, Apr., pp. 871–874.

Klebanoff, P. S.; Tidstrom, K. D.; and Sargent, L. M. 1962: The Three-Dimensional Nature of Boundary-Layer Instability. *J. Fluid Mech.*, vol. 12, pt. 1, Jan., pp. 1–34.

Kleiser, L.; and Schumann, U. 1984: Spectral Simulations of the Laminar-Turbulent Transition Process in Plane Poiseuille Flow. *Spectral Methods for Partial Differential Equations*, Robert G. Voigt, David Gottlieb, and M. Yousuff Hussaini, eds., Soc. Industrial & Applied Mathematics, pp. 141–163.

Kovasznay, L. S. G.; Komoda, H.; and Vasudeva, B. R. 1962: Detailed Flow Field in Transition. *Proceedings of the 1962 Heat Transfer and Fluid Mechanics Institute*, F. Edward Ehlers, James J. Kauzlarich, Charles A. Sleicher, Jr., and Robert E. Street, eds., Stanford University Press, pp. 1–26.

Kriess, Heinz-Otto; and Oliger, Joseph 1979: Stability of the Fourier Method. *SIAM J. Numer. Anal.*, vol. 16, no. 3, June, pp. 421–433.

Laurien, Eckart 1986: *Numerische Simulation zur aktiven Beeinflussung des laminar-turbulenten Übergangs in der Plattengrenzschichtströmung.* DFVLR-FB 86-05, Jan.

Levich, E.; and Tsinober, A. 1983: On the Role of Helical Structures in Three-Dimensional Turbulent Flow. *Phys. Lett.*, vol. 93A, no. 6, Jan. 24, pp. 293–297.

Maday, Y.; and Quarteroni, A. 1982: Spectral and Pseudo-Spectral Approximations of the Navier-Stokes Equations. *SIAM J. Numer. Anal.*, vol. 19, no. 4, Aug., pp. 761–780.

Malik, M. R.; Zang, T. A.; and Hussaini, M. Y. 1985: A Spectral Collocation Method for the Navier-Stokes Equations. *J. Comput. Phys.*, vol. 61, no. 1, Oct., pp. 64–88.

Marcus, Philip S. 1984: Simulation of Taylor-Couette Flow. Part 1. Numerical Methods and Comparison With Experiment. *J. Fluid Mech.*, vol. 146, Sept., pp. 45–64.

Moin, P.; and Kim, J. 1980: On the Numerical Solution of Time-Dependent Viscous Incompressible Fluid Flows Involving Solid Boundaries. *J. Comput. Phys.*, vol. 35, no. 3, May, pp. 381–392.

Moin, Parviz; and Kim, John 1982: Numerical Investigation of Turbulent Channel Flow. *J. Fluid Mech.*, vol. 118, pp. 341–377.

Moser, R. D.; Moin, P.; and Leonard, A. 1983: A Spectral Numerical Method for the Navier-Stokes Equations With Applications to Taylor-Couette Flow. *J. Comput. Phys.*, vol. 52, no. 3, Dec., pp. 524–544.

Nishioka, M.; Asai, M.; and Iida, S. 1980: An Experimental Investigation of the Secondary Instability. *Laminar-Turbulent Transition*, R. Eppler and H. Fasel, eds., Springer-Verlag, pp. 37–46.

Orszag, Steven A. 1971a: On the Elimination of Aliasing in Finite-Difference Schemes by Filtering High-Wavenumber Components. *J. Atmos. Sci.*, vol. 28, no. 6, Sept., p. 1074.

Orszag, Steven A. 1971b: Accurate Solution of the Orr-Sommerfeld Stability Equation. *J. Fluid Mech.*, vol. 50, pt. 4, pp. 689–703.

Orszag, Steven A.; and Kells, Lawrence C. 1980: Transition to Turbulence in Plane Poiseuille and Plane Couette Flow. *J. Fluid Mech.*, vol. 96, pt. 1, Jan. 16, pp. 159–205.

Orszag, Steven A.; and Patera, Anthony T. 1983: Secondary Instability of Wall-Bounded Shear Flows. *J. Fluid Mech.*, vol. 128, Mar., pp. 347–385.

Saric, William S.; Kozlov, Victor V.; and Levchenko, Victor Ya. 1984: Forced and Unforced Subharmonic Resonance in Boundary-Layer Transition. AIAA-84-0007, Jan.

Schamel, Hans; and Elsässer, Klaus 1976: The Application of the Spectral Method to Nonlinear Wave Propagation. *J. Comput. Phys.*, vol. 22, no. 4, Dec., pp. 501–516.

Schubauer, Galen B.; and Skramstad, Harold K. 1947: Laminar Boundary-Layer Oscillations and Transition on a Flat Plate. *J. Res. Natl. Bur. Stand.*, vol. 38, no. 2, Feb., pp. 251–292.

Smith, C. R. 1984: A Synthesized Model of the Near-Wall Behavior in Turbulent Boundary Layers. *Proceedings of Eighth Symposium on Turbulence*, X. B. Reed, Jr., G. K. Patterson, and J. L. Zakin, eds., Univ. of Missouri-Rolla, pp. 299–327.

Spalart, P. R. 1985: Numerical Simulation of Boundary-Layer Transition. *Ninth International Conference on Numerical Methods in Fluid Dynamics, Volume 218 of Lecture Notes in Physics*, Soubbaramayer and J. P. Boujot, eds., Springer-Verlag, pp. 531–535.

Speziale, Charles G. 1987: On Helicity Fluctuations in Turbulence. Quart. Appl. Math., vol. 45, no. 1, Apr.

Strazisar, A. J.; Reshotko, E.; and Prahl, J. M. 1977: Experimental Study of the Stability of Heated Laminar Boundary Layers in Water. *J. Fluid Mech.*, vol. 83, pt. 2, Nov. 22, pp. 225–247.

Wallace, James M. 1982: On the Structure of Bounded Turbulent Shear Flow: A Personal View. *Developments in Theoretical and Applied Mechanics, Volume XI*, T. J. Chung and G. R. Karr, eds., Univ. of Alabama, pp. 509–521.

Williams, D. R.; Fasel, H.; and Hama, F. R. 1984: Experimental Determination of the Three-Dimensional Vorticity Field in the Boundary-Layer Transition Process. *J. Fluid Mech.*, vol. 149, Dec., pp. 179–203.

Wray, A.; and Hussaini, M. Y. 1984: Numerical Experiments in Boundary-Layer Stability. *Proc. R. Soc. London*, ser. A, vol. 392, no. 1803, Apr. 9, pp. 373–389.

Zang, Thomas A.; and Hussaini, M. Yousuff 1985a: Numerical Experiments on Subcritical Transition Mechanisms. AIAA-85-0296, Jan.

Zang, Thomas A.; and Hussaini, M. Yousuff 1985b: Numerical Experiments on the Stability of Controlled Shear Flow. AIAA-85-1698, July.

Zang, Thomas A.; and Hussaini, M. Yousuff 1986: On Spectral Multigrid Methods for the Time-Dependent Navier-Stokes Equations. *Appl. Math. & Comput.*, vol. 19, pp. 359–372.

Nomenclature

a	vertical grid stretching parameter
E_{k_x,k_z}	kinetic energy in (k_x, k_z) Fourier component
E_n	kinetic energy in nth Chebyshev component
h	dimensional channel half-width
k_x	scaled streamwise Fourier harmonic
k_z	scaled spanwise Fourier harmonic
$\hat{k}_x$	streamwise Fourier harmonic
$\hat{k}_z$	spanwise Fourier harmonic
L_x	periodicity length in X-direction
L_z	periodicity length in Z-direction
N_c	number of grid points inside critical layer
N_x	number of grid points in X-direction
N_y	number of grid points in Y-direction
N_z	number of grid points in Z-direction
N_ν	number of grid points inside viscous sublayer
P	total pressure
p	pressure
R	Reynolds number, $u_c h/\nu$
s_x	number of subharmonics in X-direction
s_z	number of subharmonics in Z-direction
T_n	Chebyshev polynomial of degree n
t	time
$\mathbf{u}$	total velocity vector
$\hat{\mathbf{u}}_{k_x,k_z}$	velocity after transforms in X and Z
$\tilde{\mathbf{u}}_n$	velocity after transform in Y
u	streamwise velocity component
u_c	dimensional centerline velocity
u_{SL}	mean flow at shear layer height
u_0	mean flow
$\mathbf{u}_{2D}$	two-dimensional eigenfunction
$\mathbf{u}_{3D}$	three-dimensional eigenfunction
v	normal velocity component
w	spanwise velocity component
X	streamwise coordinate
X_{SL}	X position of shear layer
Y	normal coordinate
Y_c	Y position of critical layer of two-dimensional TS wave
Y_{SL}	Y position of shear layer
Y_ν	Y position of edge of viscous sublayer
Z	spanwise coordinate
α	streamwise wave number
β	spanwise wave number
$\delta_{k,\ell}$	Kronecker delta function
ΔZ	grid spacing in spanwise direction
ϵ_{2D}	initial amplitude of two-dimensional TS wave
ϵ_{3D}	initial amplitude of three-dimensional TS wave
ν	dimensional kinematic viscosity
ξ	computational coordinate in normal direction
ω	vorticity
ω_{Sqr}	temporal frequency of subharmonic squire mode
ω_{2D}	temporal frequency of two-dimensional TS wave
ω_{3D}	temporal frequency of three-dimensional TS wave

Abbreviations:

FCBM	Fourier-Chebyshev method
FFDM	Fourier finite-difference method
TS	Tollmien-Schlichting

Table I. Effect of Vertical Resolution on Growth Rate

[$R = 1500$, three-dimensional TS wave]

Algorithm	N_y	Calculated $\mathrm{Im}(\omega_{3D})$	Error in $\mathrm{Im}(\omega_{3D})$
Exact		−0.028230	
FCBM	64	−.028226	−0.000004
FFDM	50	−.032030	−.003800
FFDM	100	−.029230	−.001000
FFDM	200	−.028482	−.000252

Table II. Eigenfrequencies of the Least Stable Linear Waves

R	ω_{2D}	ω_{3D}	ω_{Sqr}
1500	0.326299 − 0.028206i	0.401293 − 0.028230i	0.171386 − 0.092617i
8000	0.247075 + 0.002664i	0.292106 − 0.022388i	0.099426 − 0.055327i

Table III. Resolution Information

R	Y_c	N_c/N_y	Y_ν	N_ν/N_y
1500	−0.821	0.193	−0.982	0.061
8000	−.868	.166	−.992	.040

Table IV. Position and Speed of Detached Shear Layer for the $R = 1500$, K-Type Transition

t	X_{SL}/L_x	Y_{SL}	u_{SL}	$\bar{u}_0(Y_{\mathrm{SL}})$
15.000	0.56	−0.31	0.69	0.90
18.750	.78	−.16	.78	.98
20.625	.92	−.06	.83	1.00
22.500	1.06	.12	.81	.98
25.000	1.23	.31	.79	.90

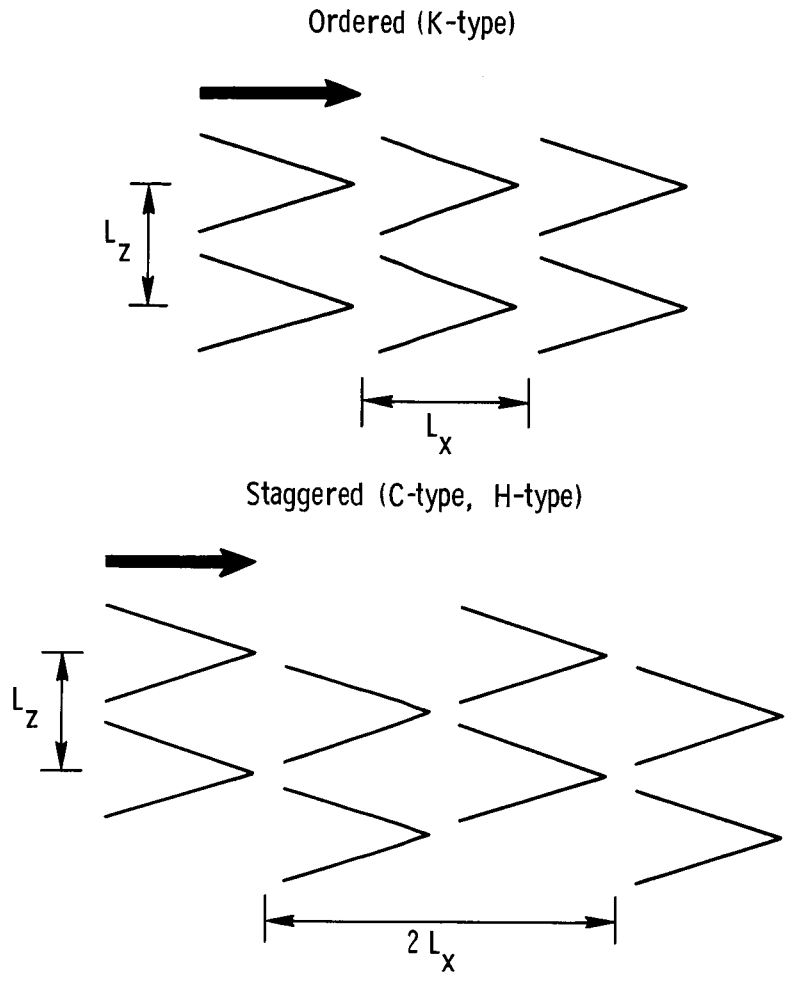

Figure 1. Lambda vortex patterns in transitional flows.

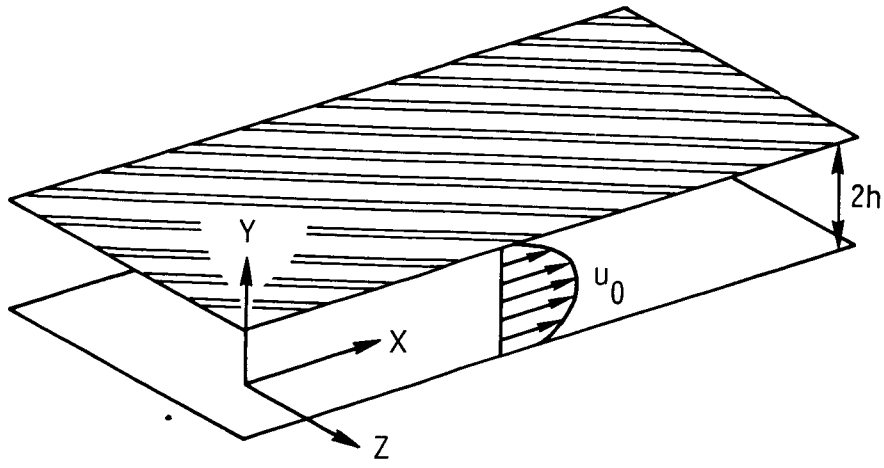

Figure 2. Channel flow geometry. The streamwise coordinate is X, the spanwise Z, and the normal (or vertica coordinate is Y.

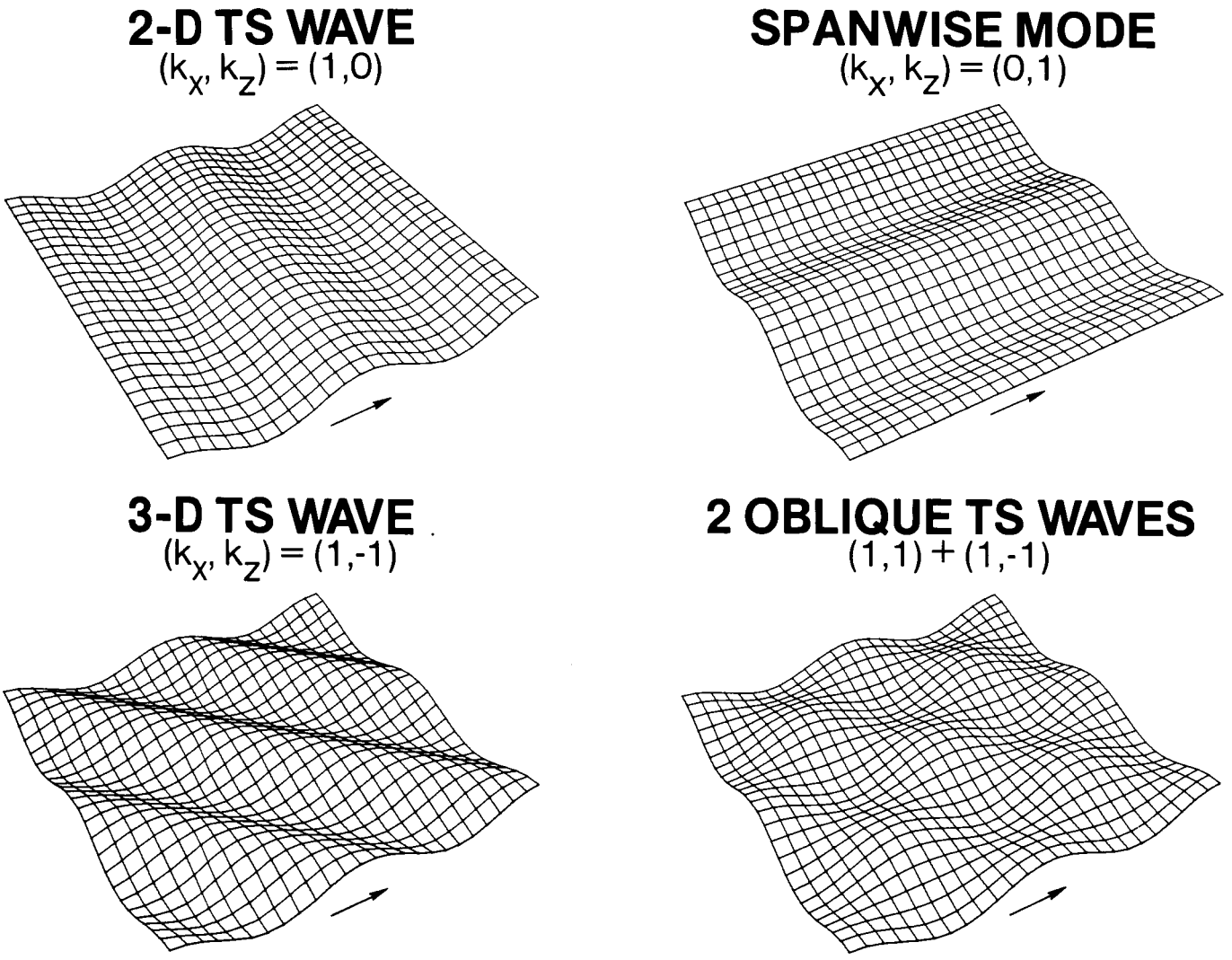

Figure 3. Horizontal structure of several Fourier components. The flow direction is indicated by the arrows. Two fundamental wavelengths are plotted in both streamwise and spanwise directions.

ORIGINAL PAGE
COLOR PHOTOGRAPH

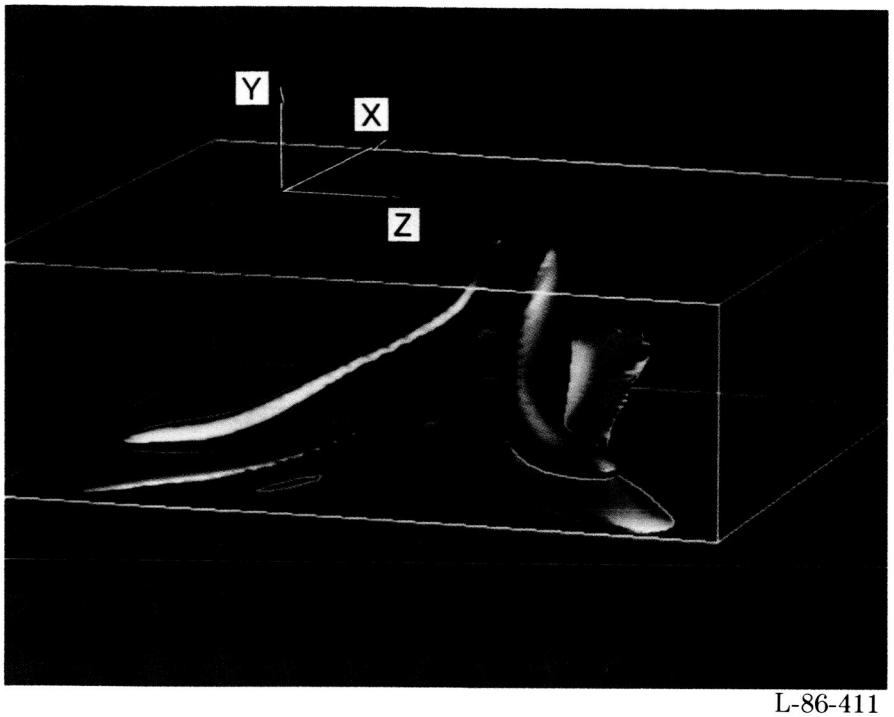

L-86-411

(a) Streamwise vorticity component.

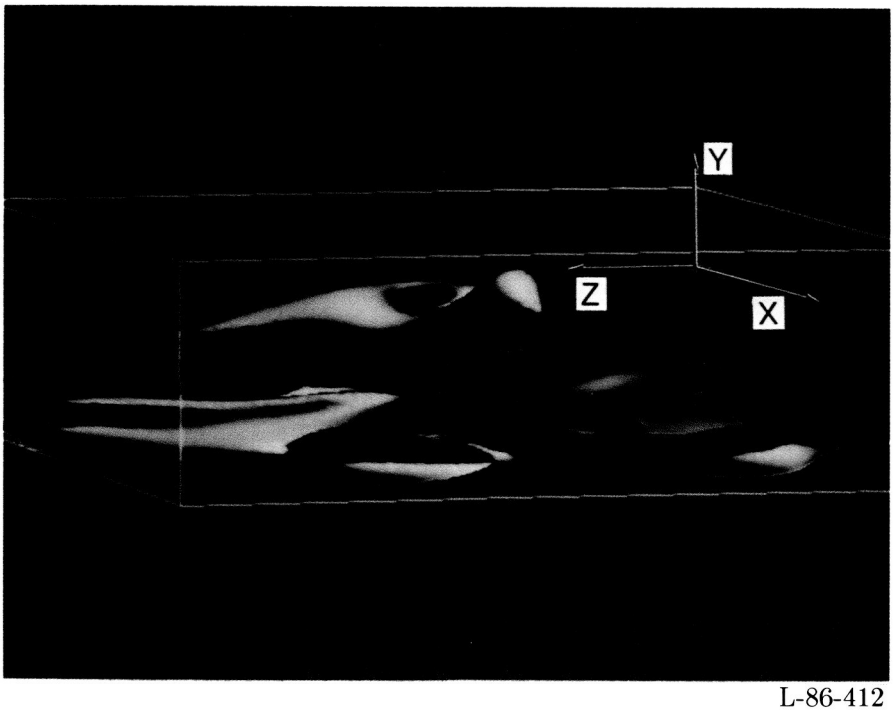

L-86-412

(b) Spanwise vorticity component.

Figure 4. Vorticity components of the $R = 1500$, K-type transition at $t = 18.75$.

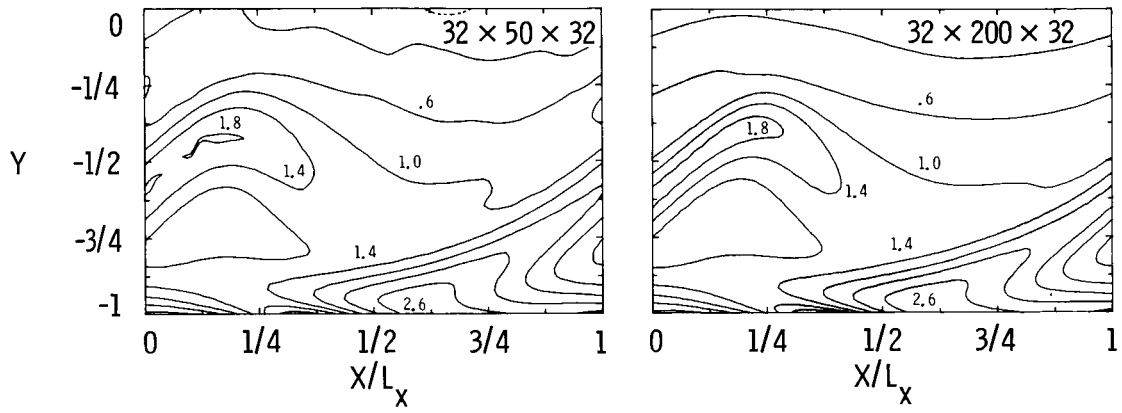

Figure 5. Vertical shear ($\partial u/\partial Y$) in the peak plane ($Z/L_z = 1$) at $t = 7.5$ from two FFDM calculations.

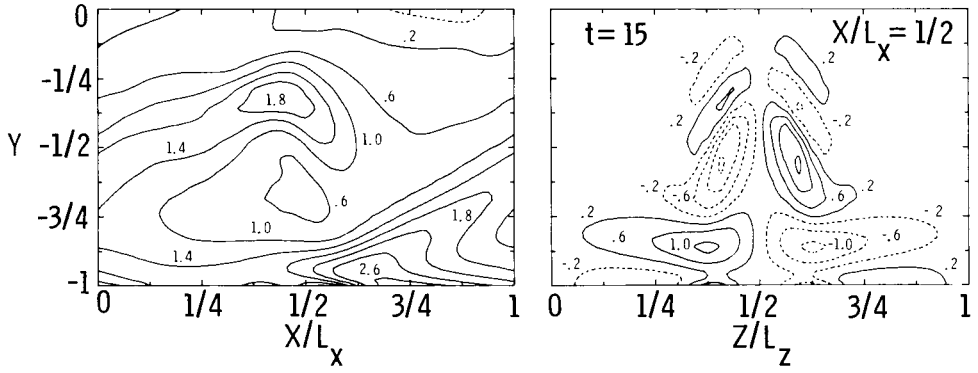

Figure 6. Vertical shear in the peak plane (left) and streamwise vorticity at $X/L_x = 1/2$ (right) from a FFDM calculation on a $32 \times 50 \times 32$ grid at $t = 15$.

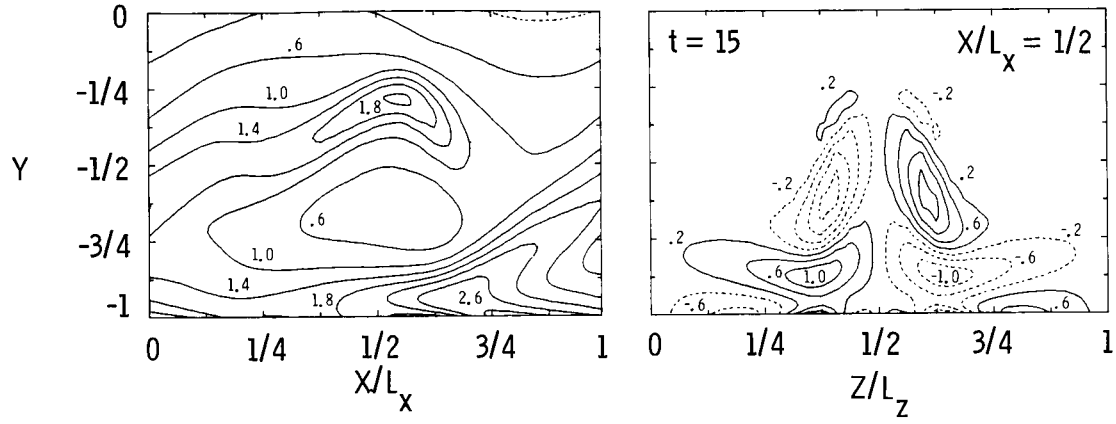

Figure 7. Vertical shear in the peak plane (left) and streamwise vorticity at $X/L_x = 1/2$ from a FFDM calculation on a $32 \times 200 \times 32$ grid at $t = 15$.

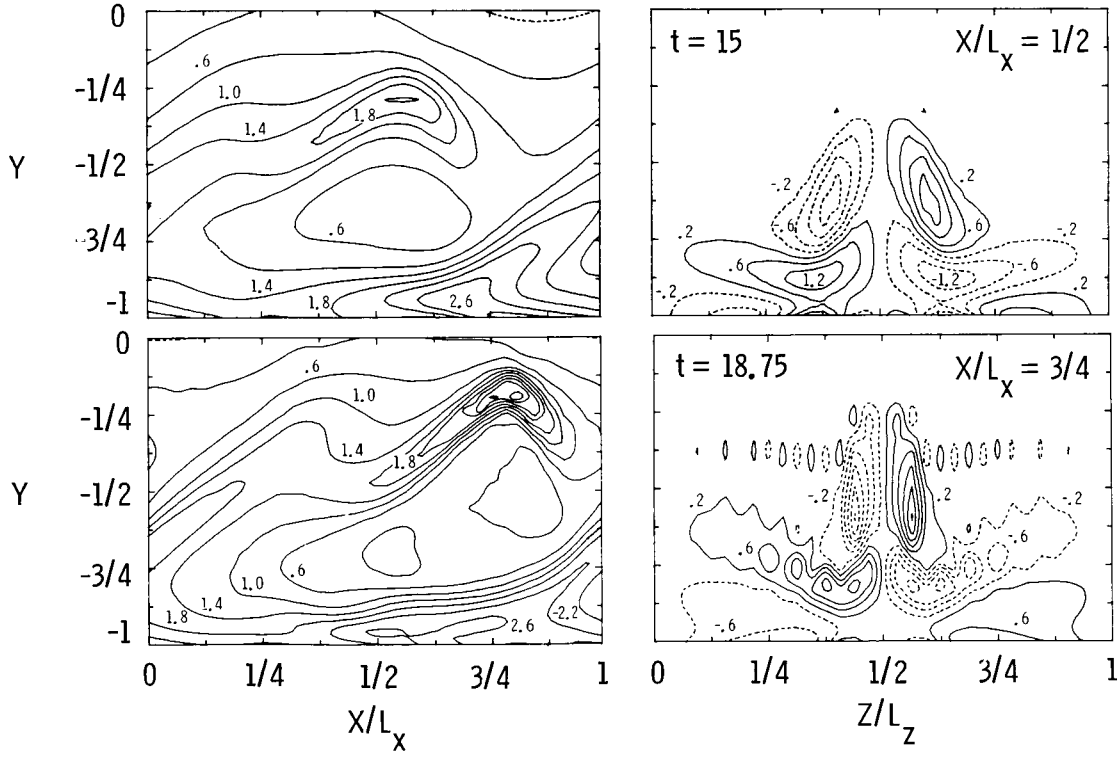

Figure 8. Vertical shear in the peak plane (left) and streamwise vorticity near the tip of the vortex loop (right) from a FCBM calculation on a $32 \times 64 \times 32$ grid.

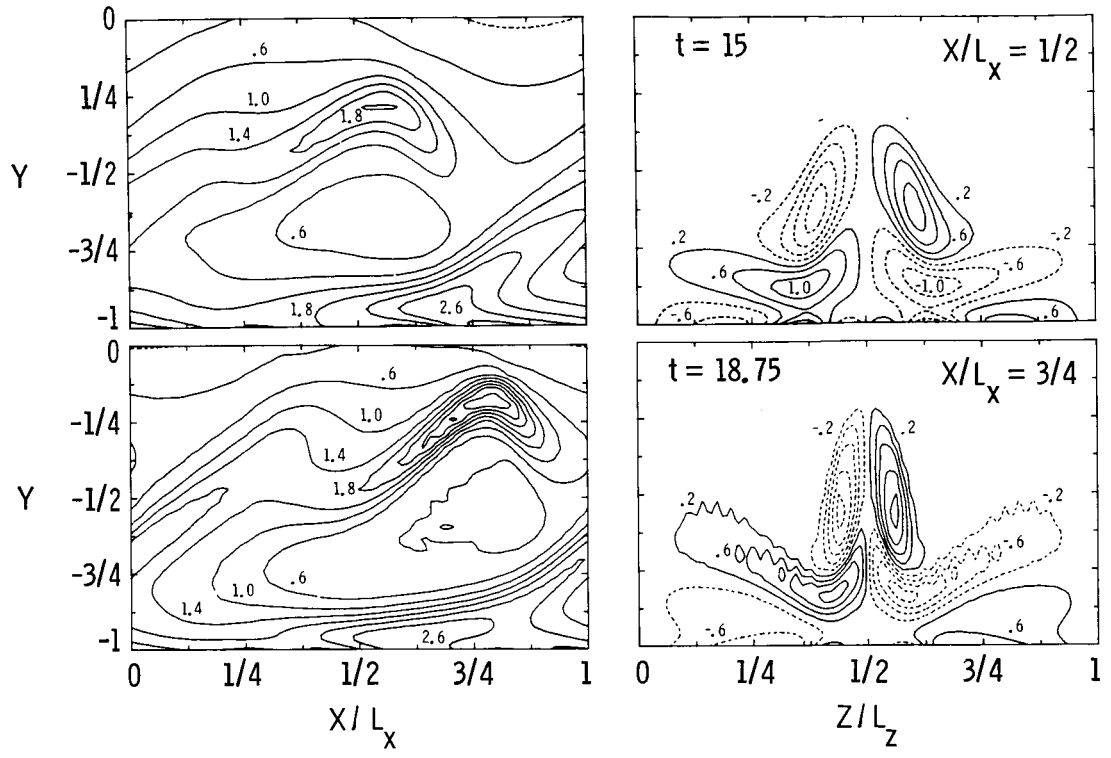

Figure 9. Vertical shear in the peak plane (left) and streamwise vorticity near the tip of the vortex loop (right) from a FCBM calculation on a 64^3 grid.

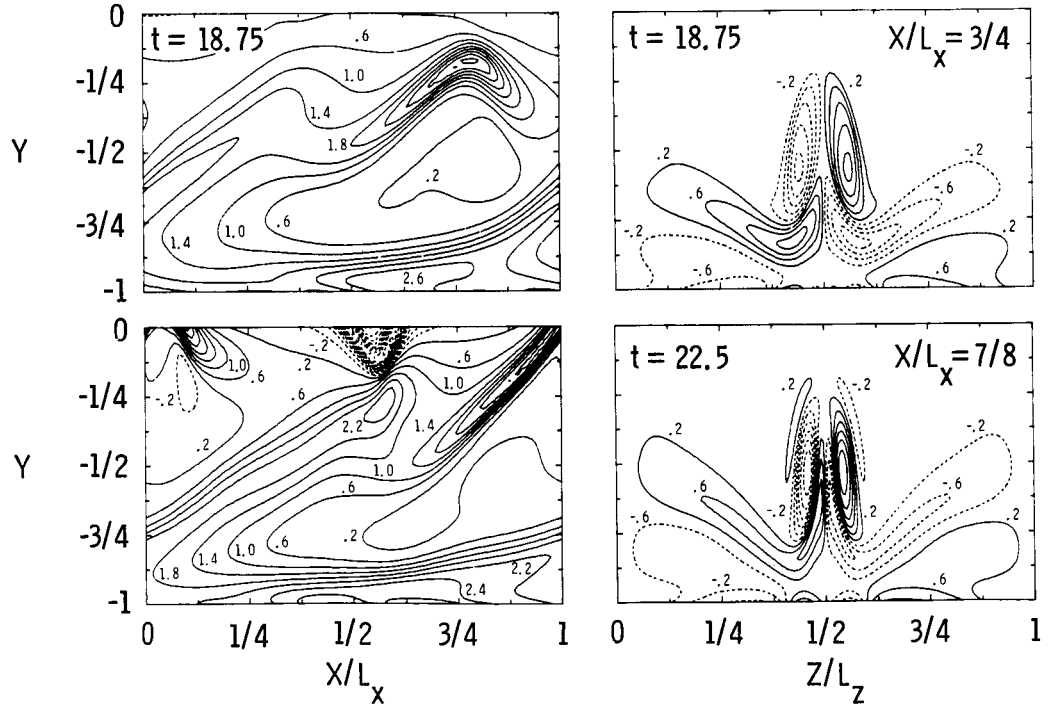

Figure 10. Vertical shear in the peak plane (left) and streamwise vorticity near the tip of the vortex loop (right) from a FCBM calculation on a $96 \times 128 \times 162$ grid at $t = 18.75$ and on a $96 \times 128 \times 216$ grid at $t = 22.5$.

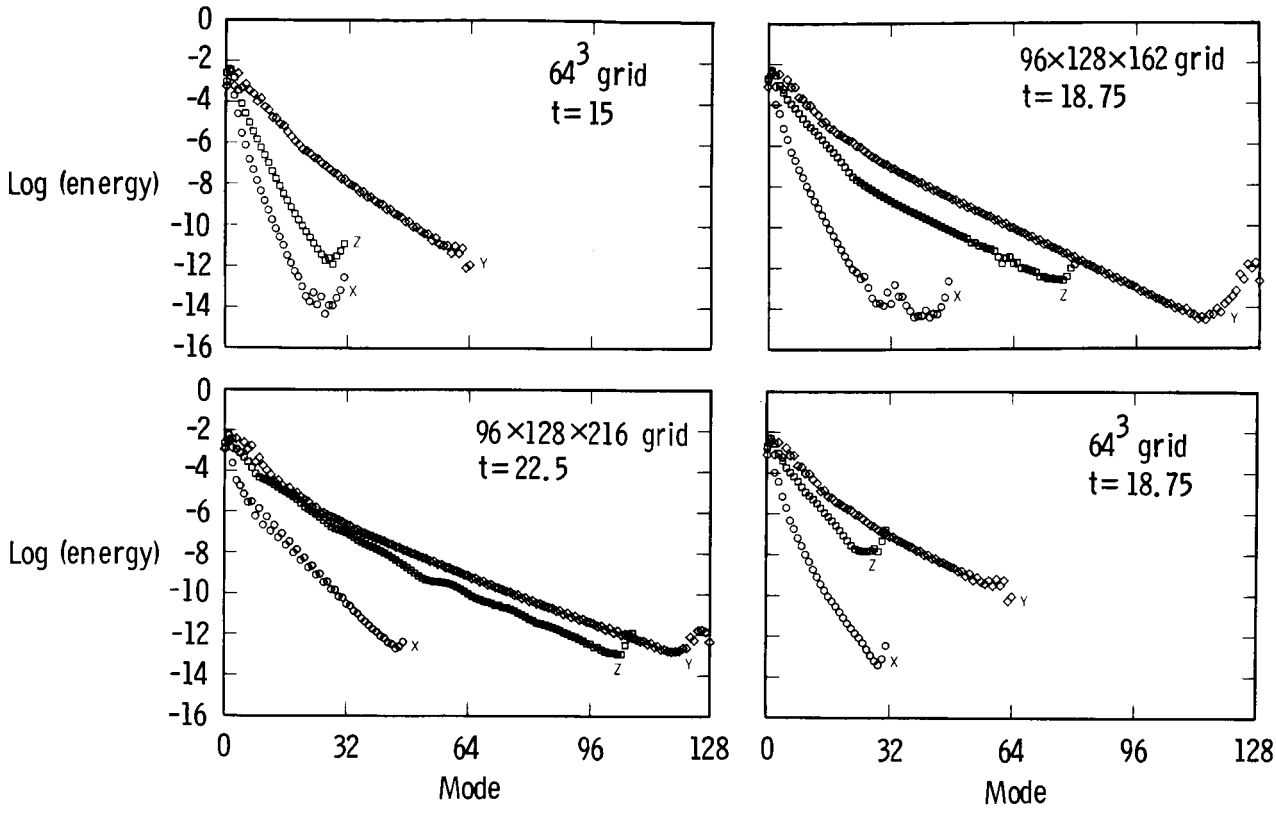

Figure 11. Energy spectra in each of the coordinate directions for the FCBM calculations.

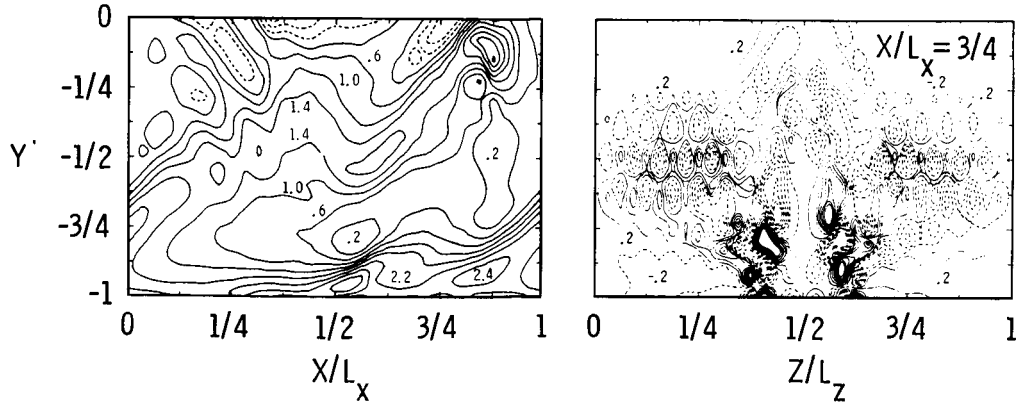

Figure 12. Vertical shear in the peak plane (left) and streamwise vorticity at $X/L_x = 3/4$ (right) from a FFDM calculation on a $32 \times 50 \times 32$ grid at $t = 22.5$.

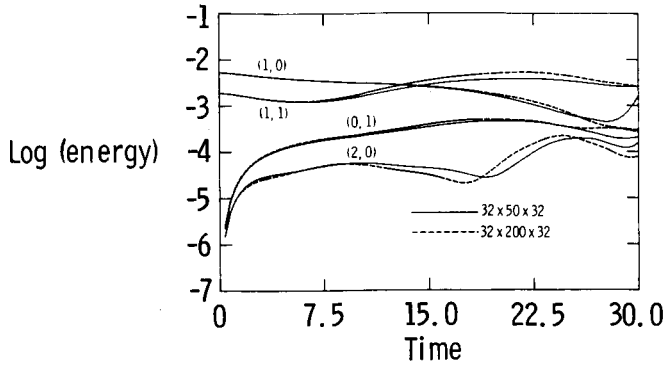

Figure 13. Kinetic energy in several (k_x, k_z) harmonics for the two FFDM calculations.

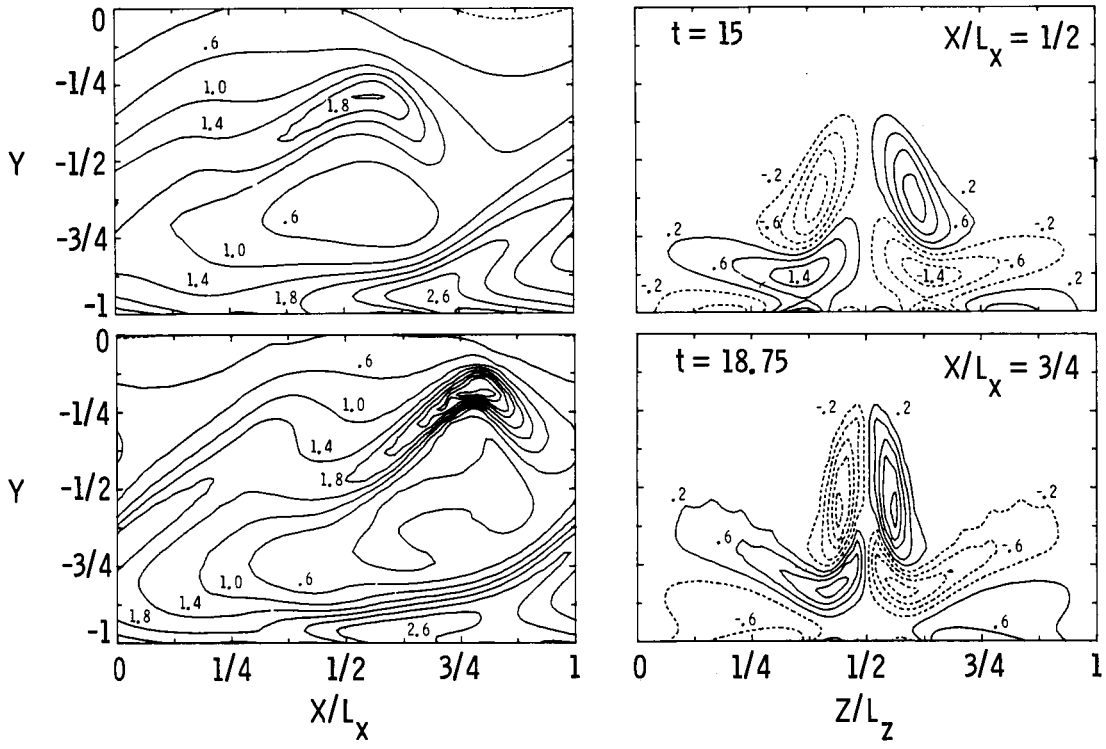

Figure 14. Vertical shear in the peak plane (left) and streamwise vorticity near the tip of the vortex loop (right) from a horizontally de-aliased FCBM calculation on a $48 \times 64 \times 48$ grid.

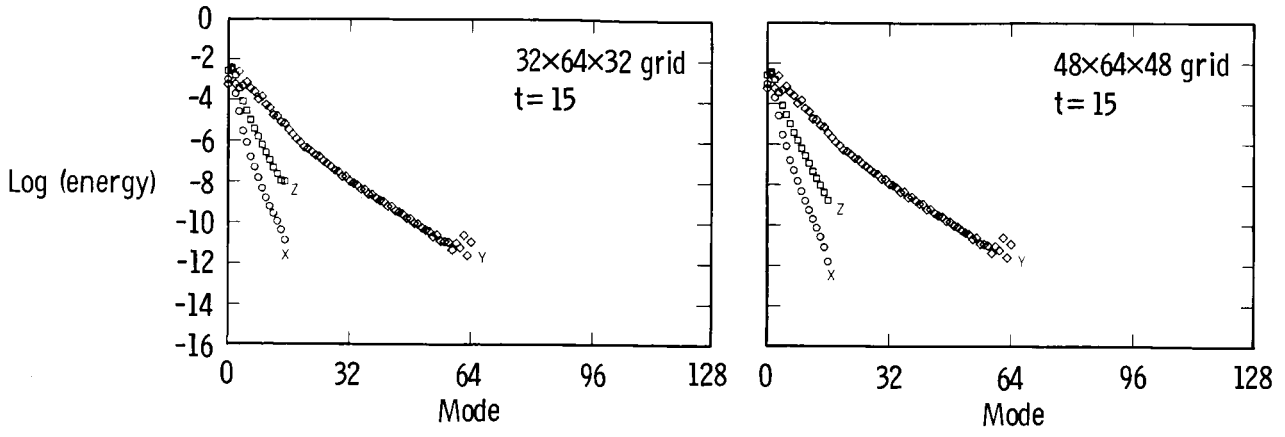

Figure 15. Energy spectra in each of the coordinate directions for a $32 \times 64 \times 32$ FCBM calculation and a horizontally de-aliased $48 \times 64 \times 48$ FCBM calculation.

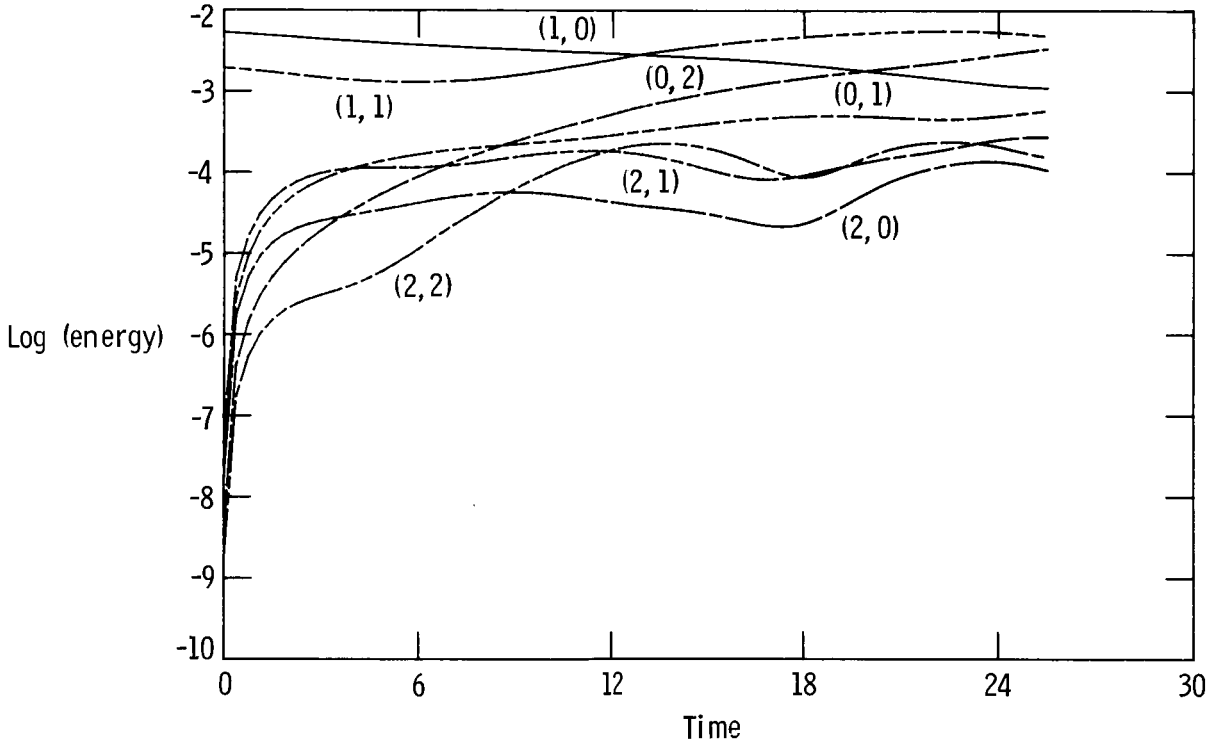

Figure 16. Kinetic energy in several (k_x, k_z) harmonics for the $R = 1500$, K-type transition.

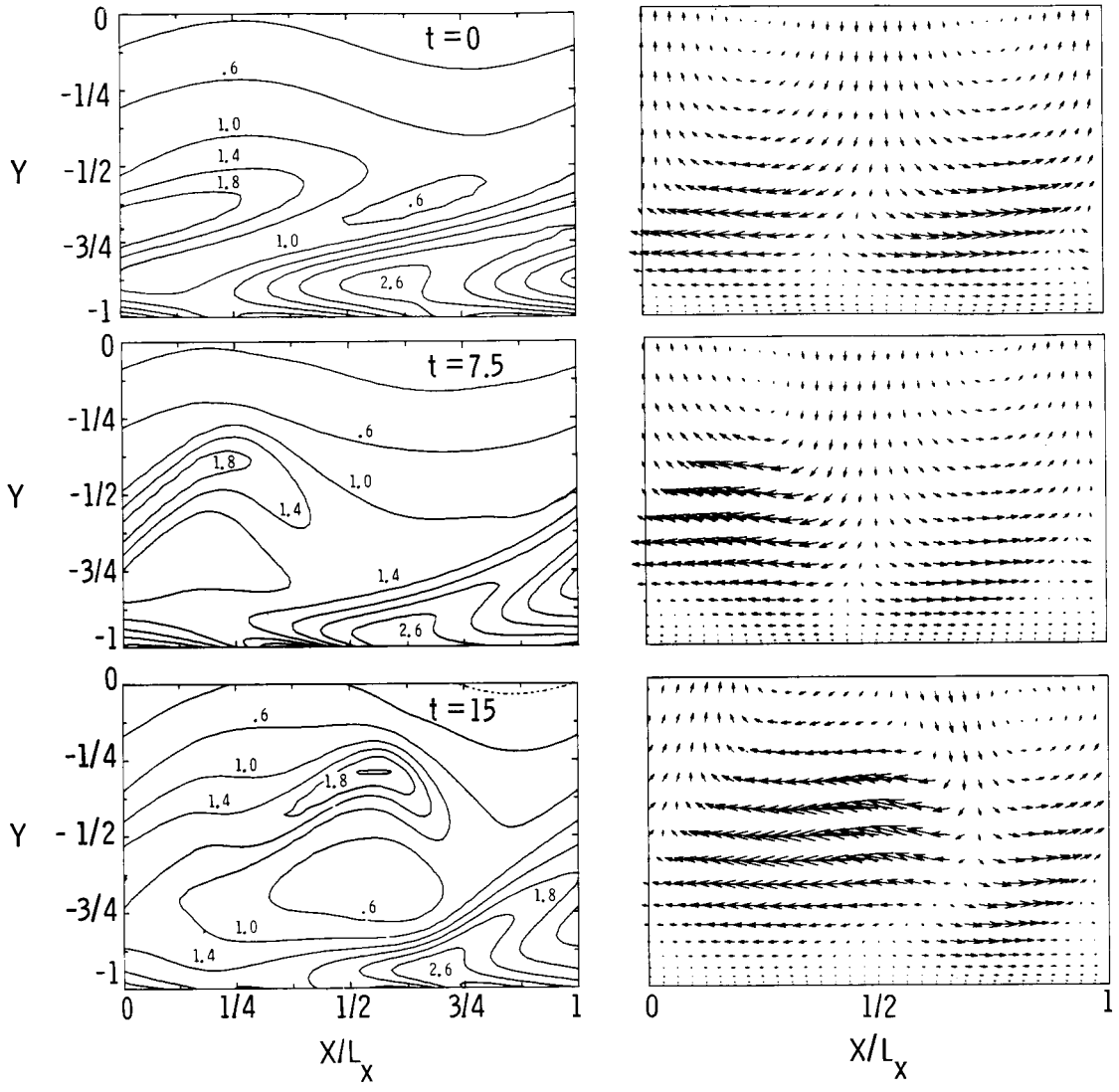

Figure 17. Vertical shear (left) and perturbation u-v velocity vector (right) in the peak plane for the $R = 1500$, K-type transition.

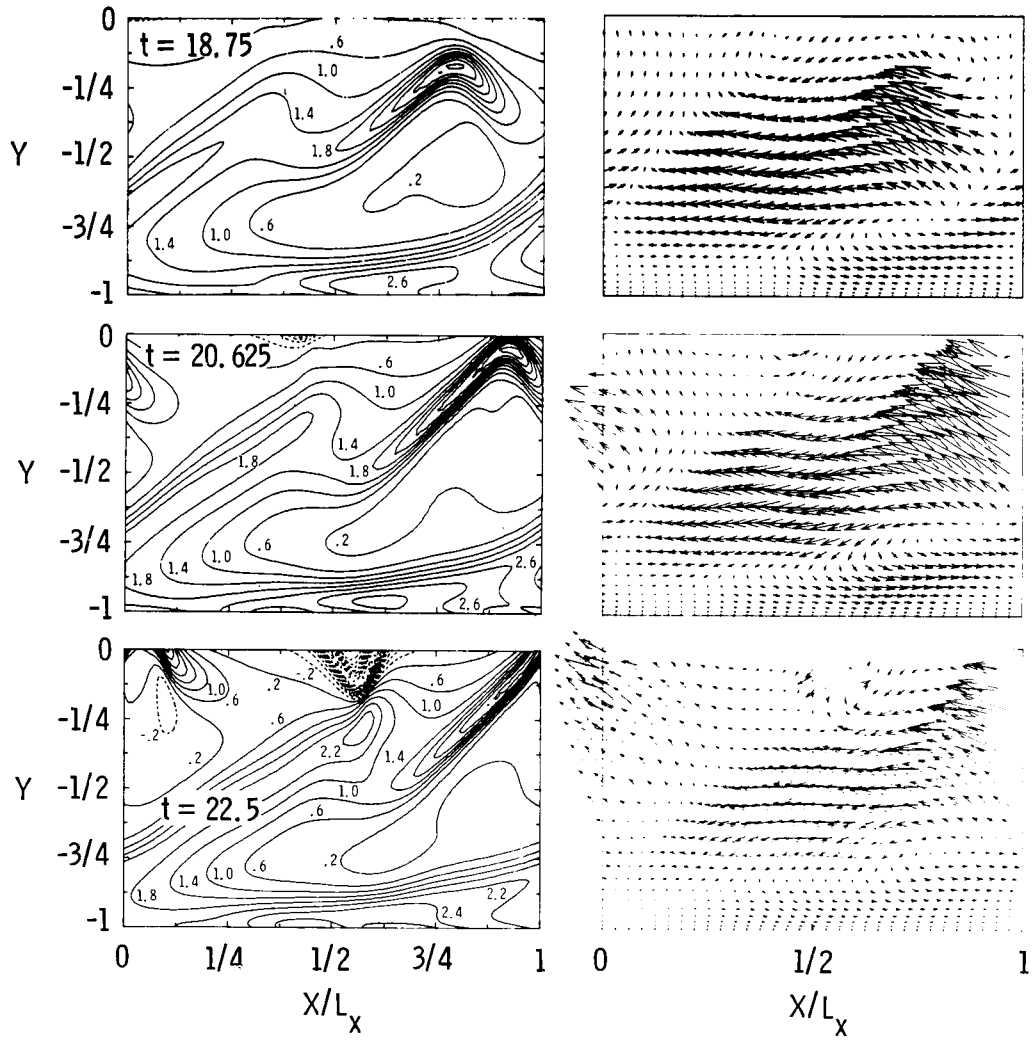

Figure 17. Concluded.

ORIGINAL PAGE IS
OF POOR QUALITY

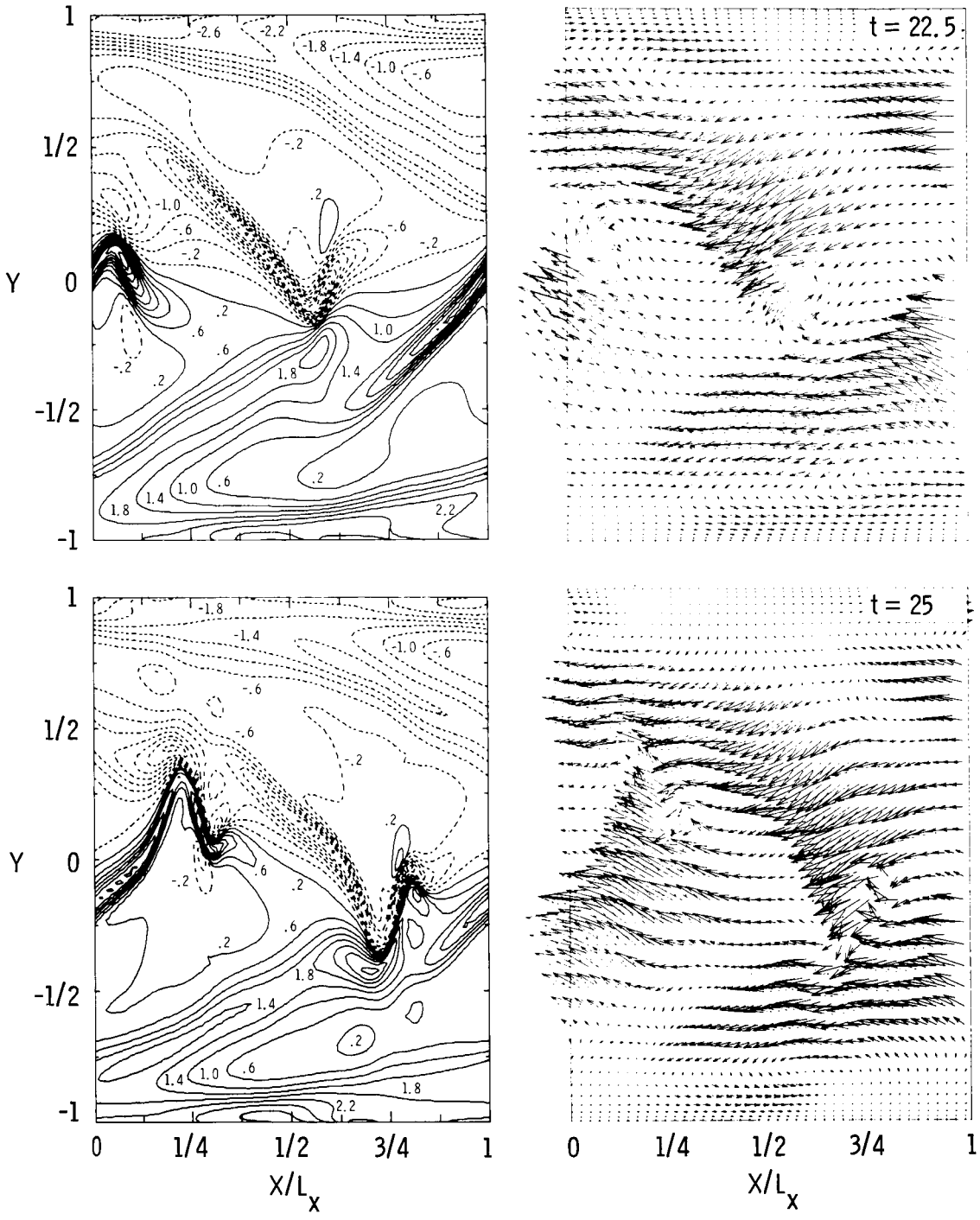

Figure 18. Full channel vertical shear (left) and perturbation u-v velocity vector (right) in the peak plane for the $R = 1500$, K-type transition.

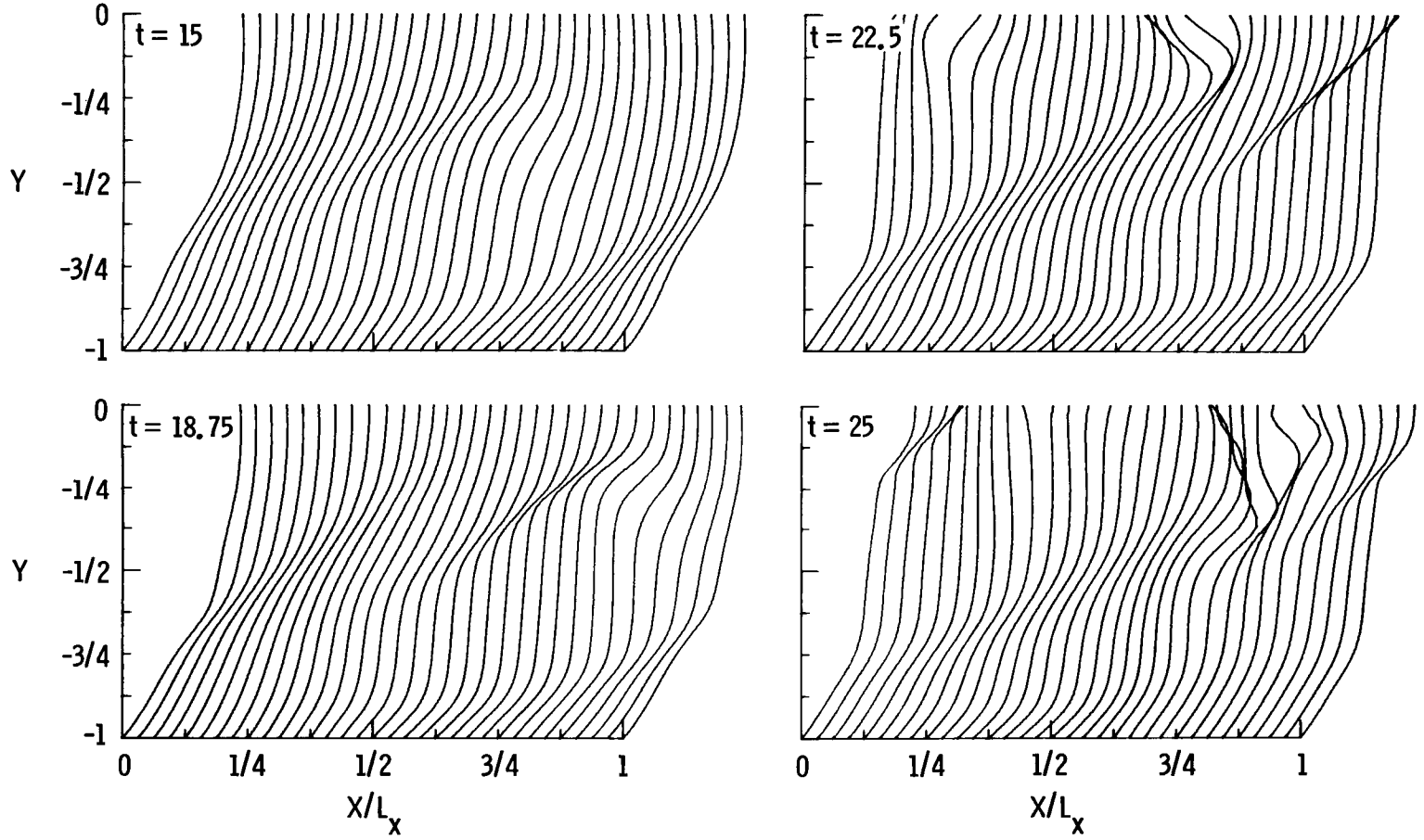

Figure 19. Streamwise velocity profiles in the peak plane for the $R = 1500$, K-type transition.

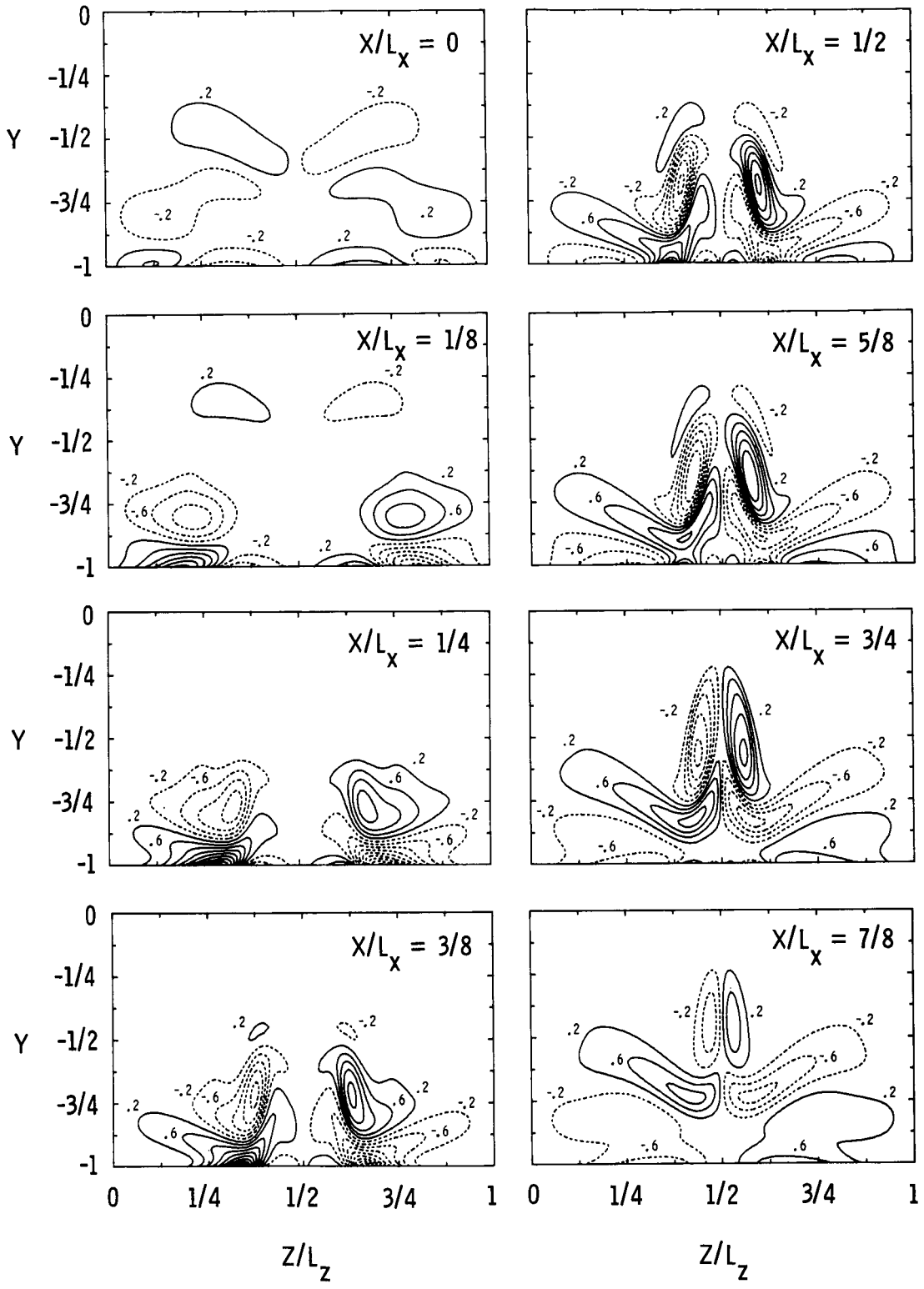

(a) Streamwise vorticity.

Figure 20. Vorticity contours for the $R = 1500$, K-type transition at $t = 18.75$.

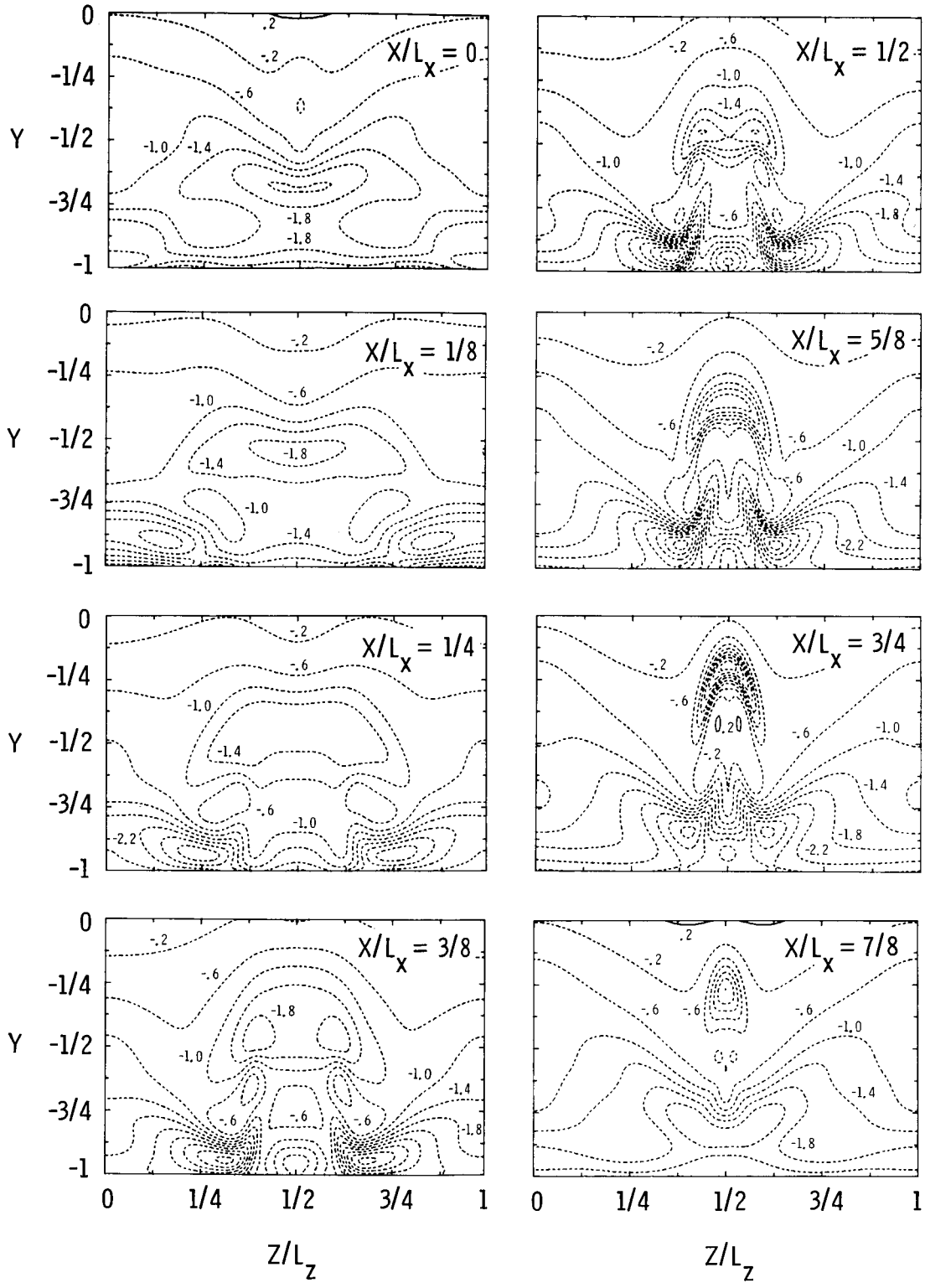

(b) Spanwise vorticity.

Figure 20. Concluded.

ORIGINAL PAGE IS
OF POOR QUALITY

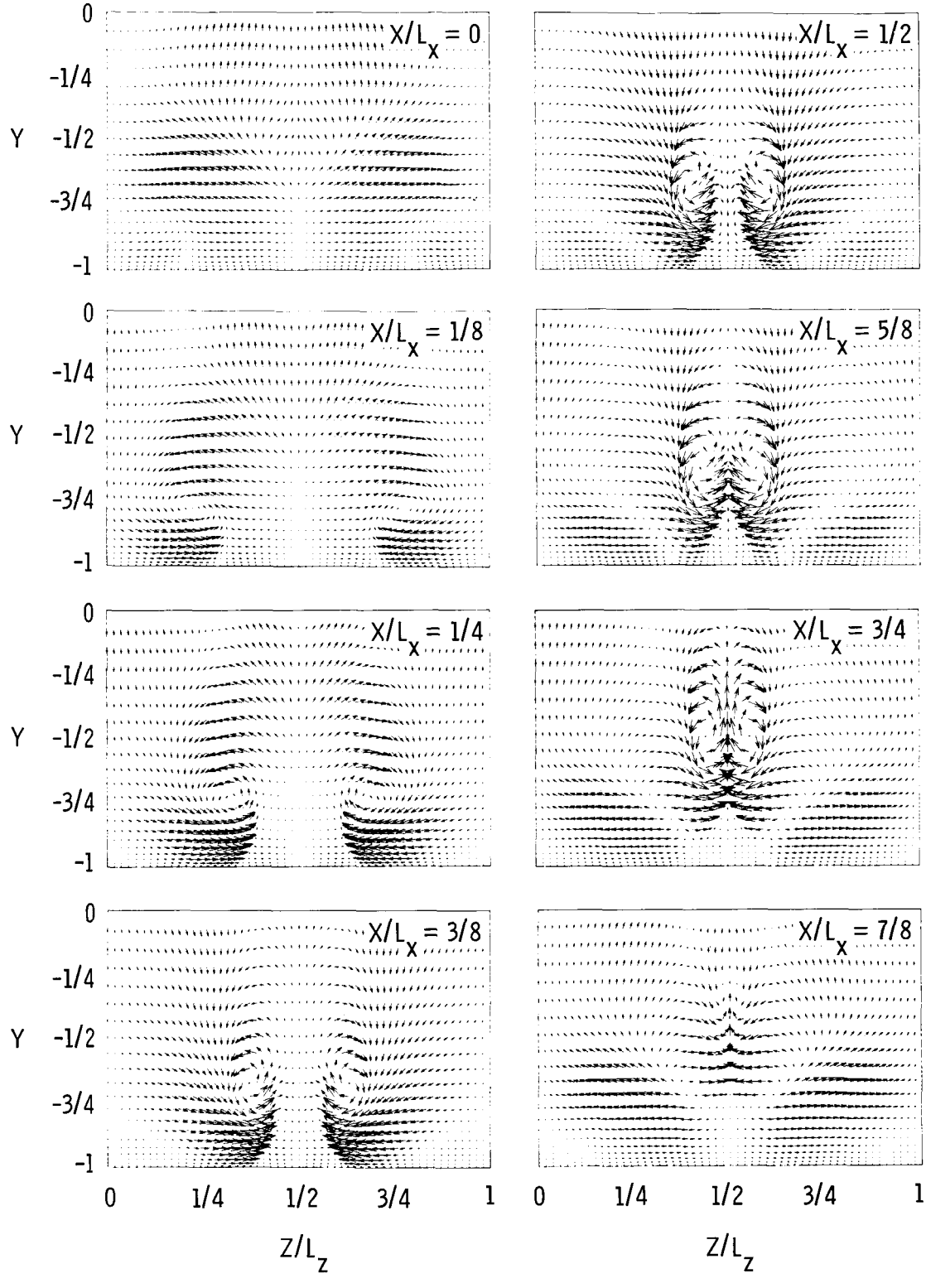

Figure 21. Cross-stream (v-w) velocity vectors for the $R = 1500$, K-type transition at $t = 18.75$.

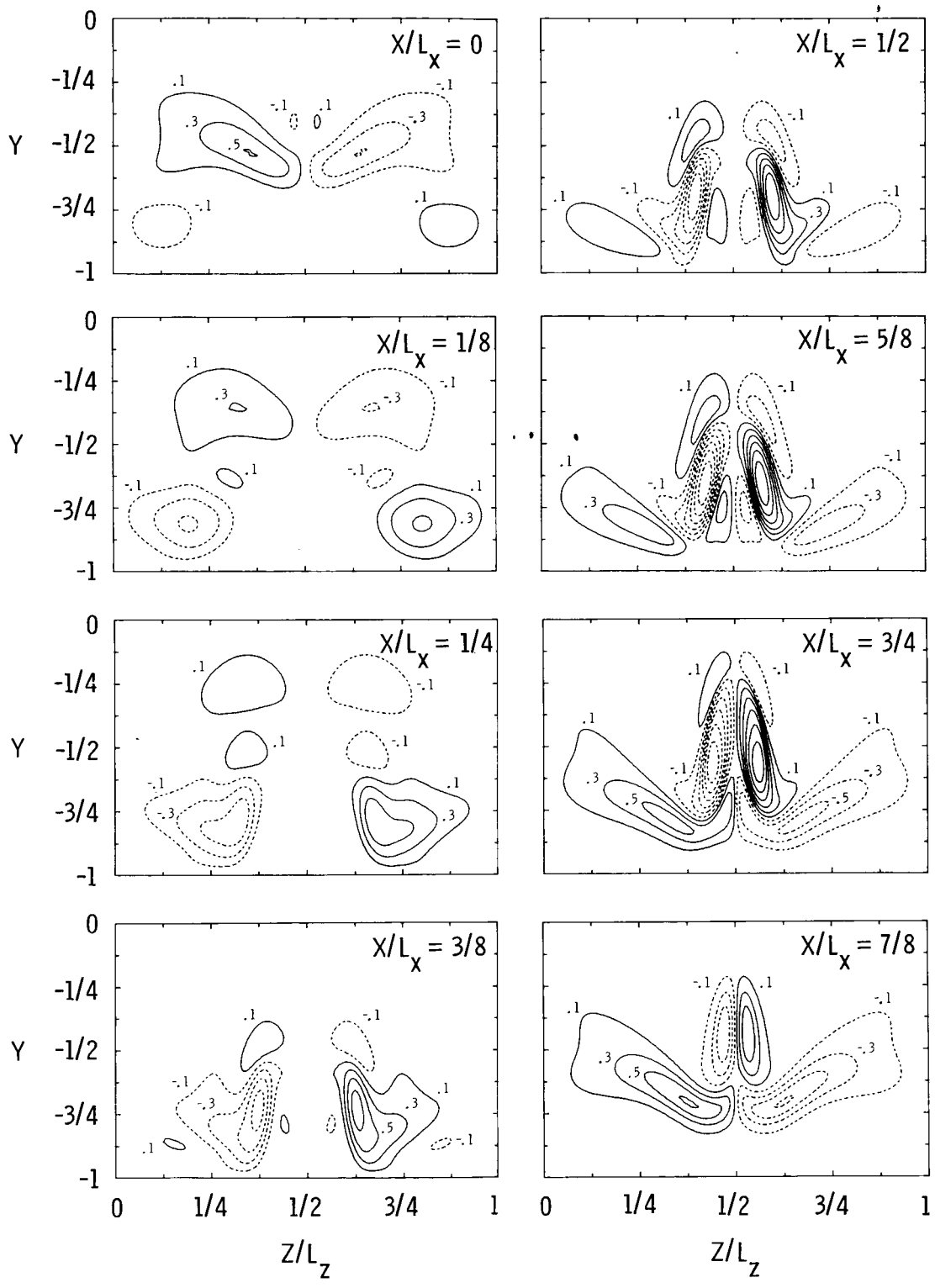

Figure 22. Helicity contours of the $R = 1500$, K-type transition at $t = 18.75$.

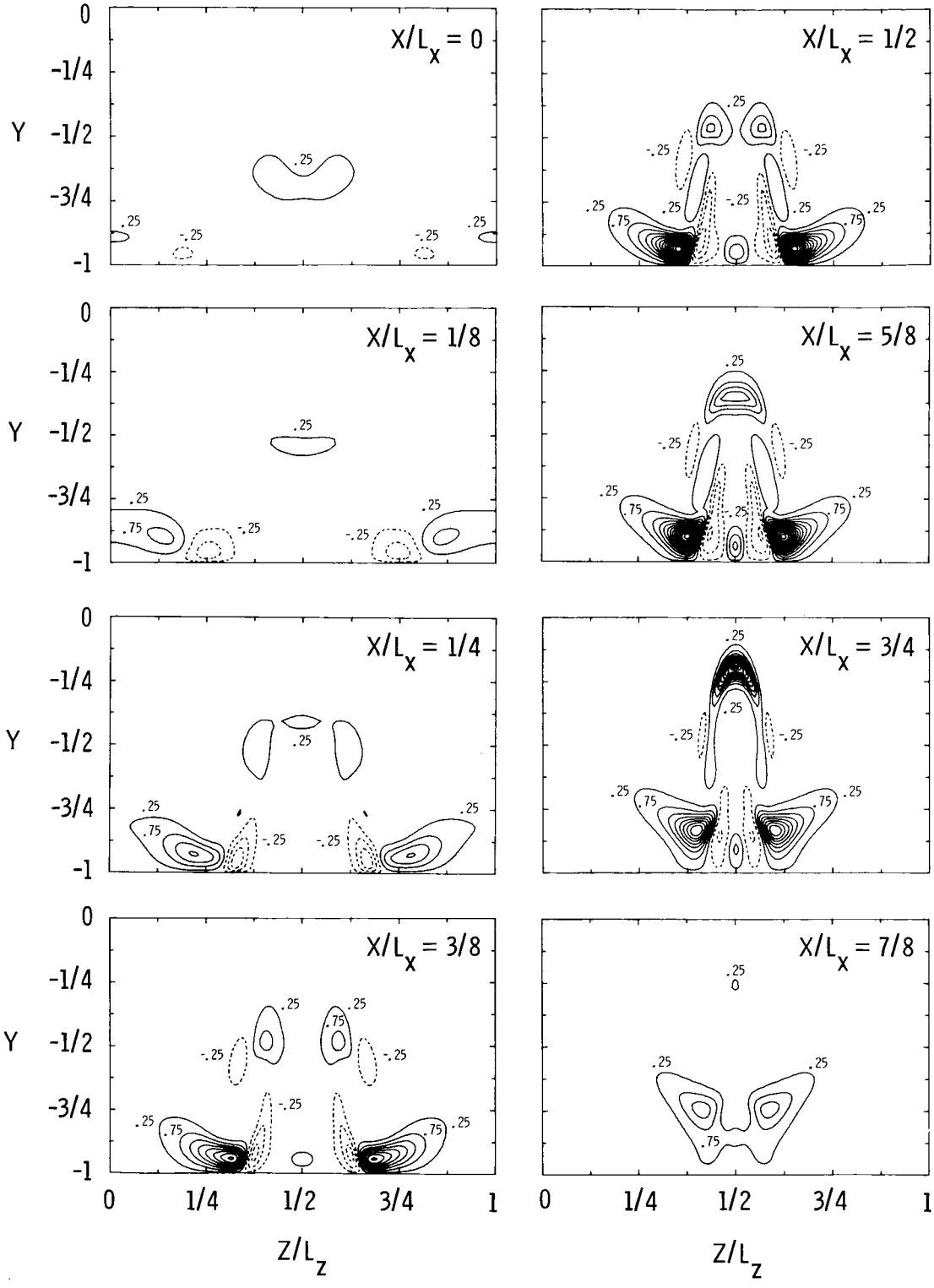

(a) Vortex stretching rate.

Figure 23. Vortex stretching and diffusion contours of the $R = 1500$, K-type transition at $t = 18.75$.

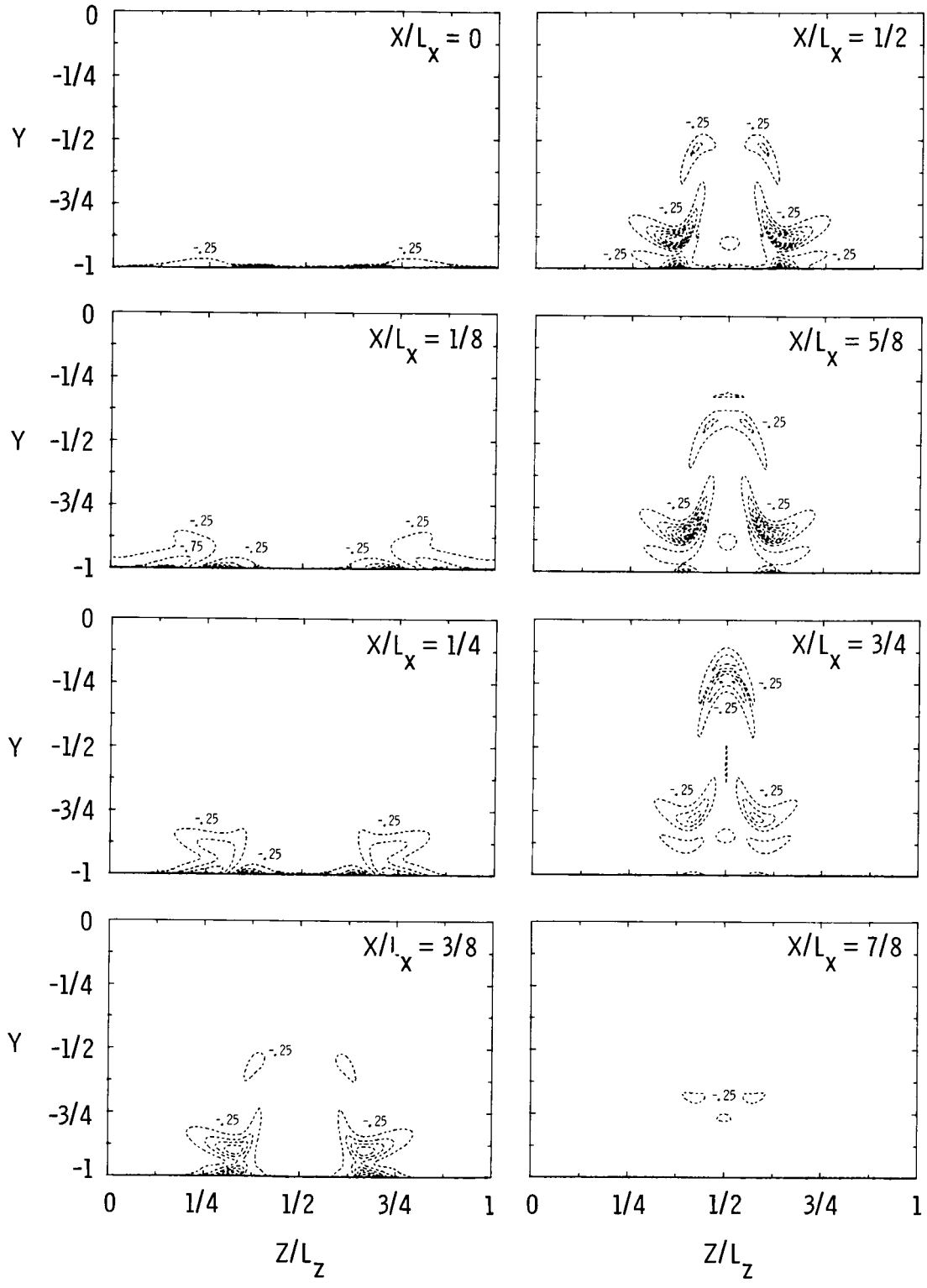

(b) Vortex diffusion rate.

Figure 23. Concluded.

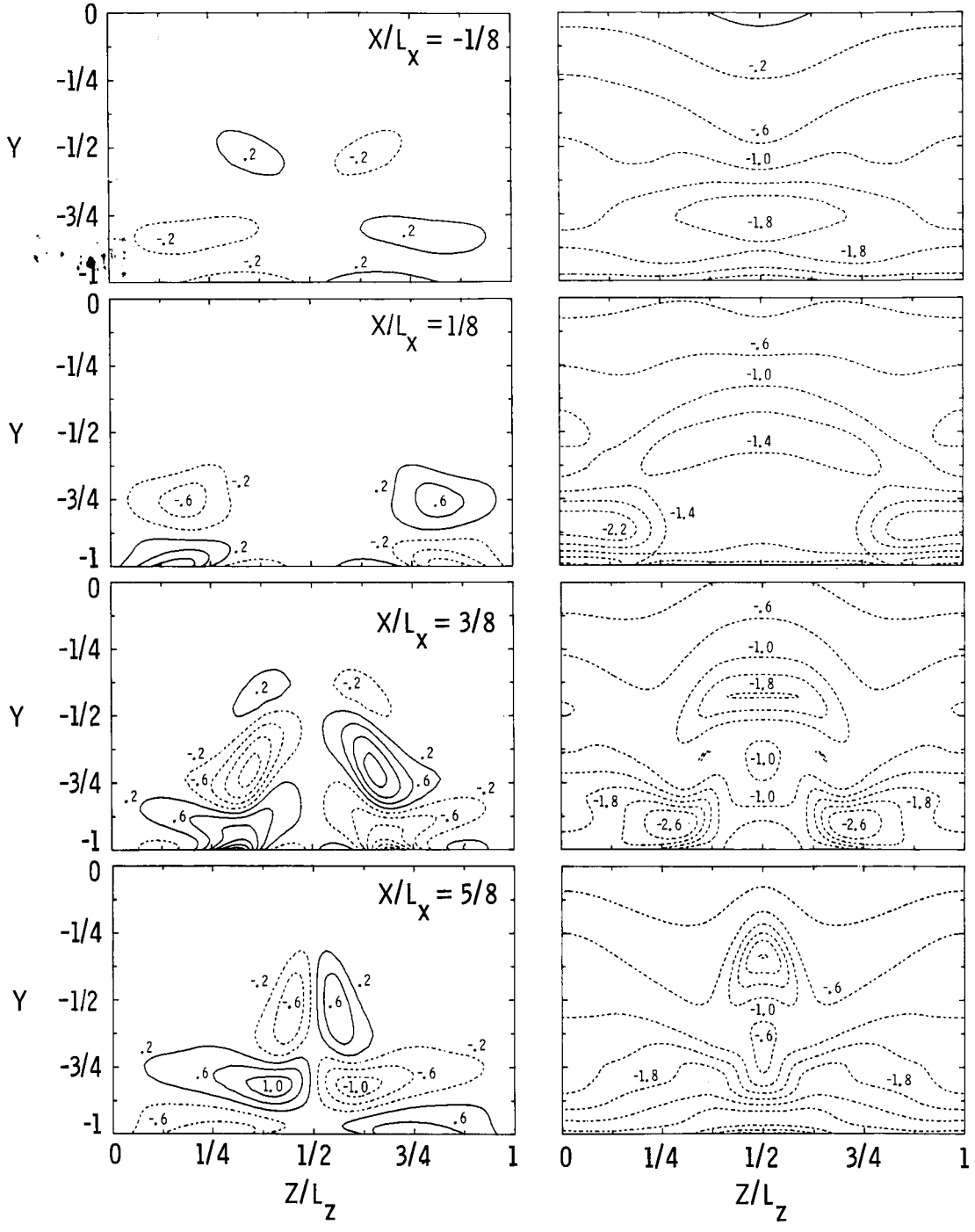

Figure 24. Streamwise vorticity (left) and spanwise vorticity (right) contours for the $R = 1500$, K-type transition at $t = 15$.

ORIGINAL PAGE IS
OF POOR QUALITY

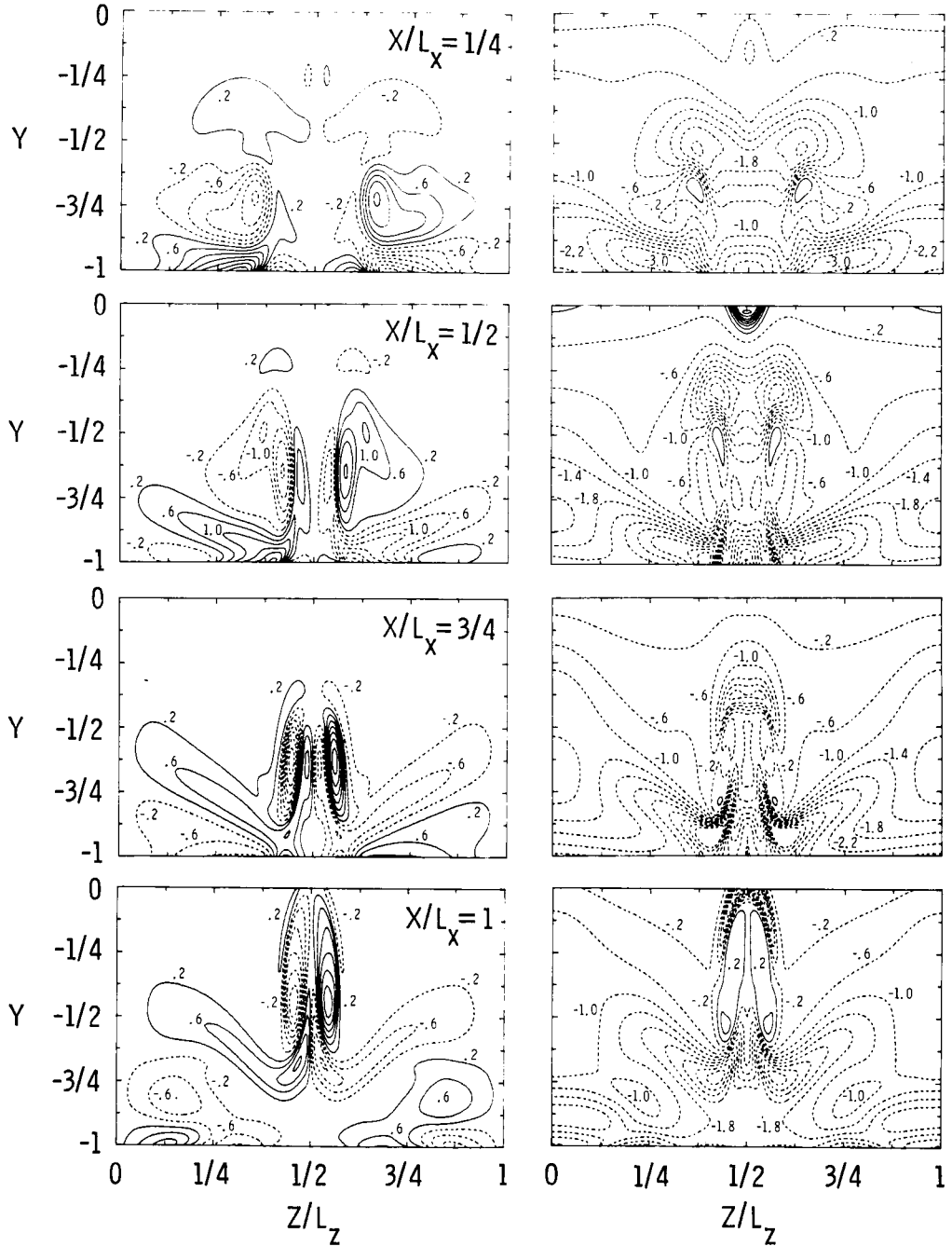

Figure 25. Streamwise vorticity (left) and spanwise vorticity (right) contours for the $R = 1500$, K-type transition at $t = 22.5$.

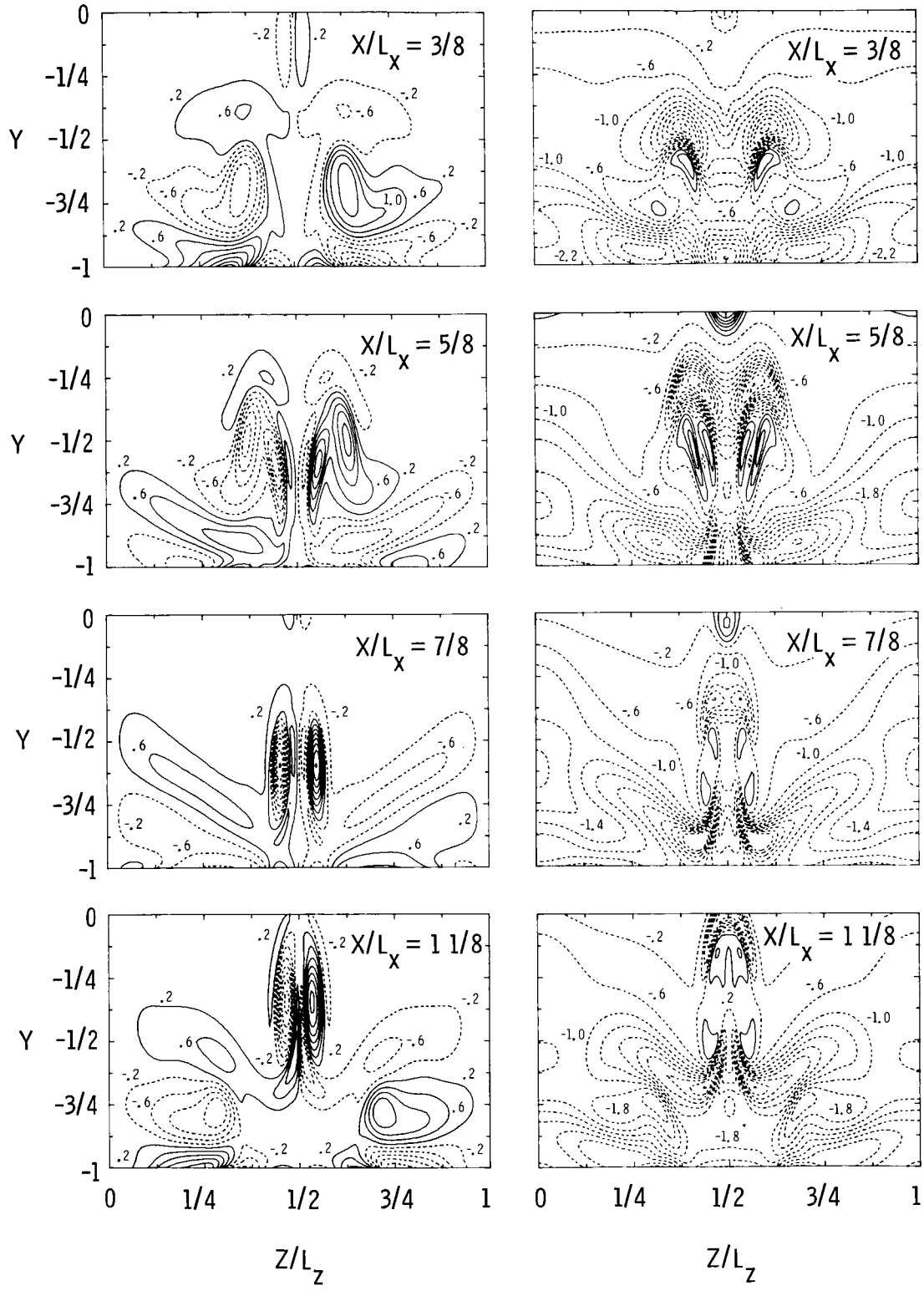

Figure 26. Streamwise vorticity (left) and spanwise vorticity (right) contours for the $R = 1500$, K-type transition at $t = 25$.

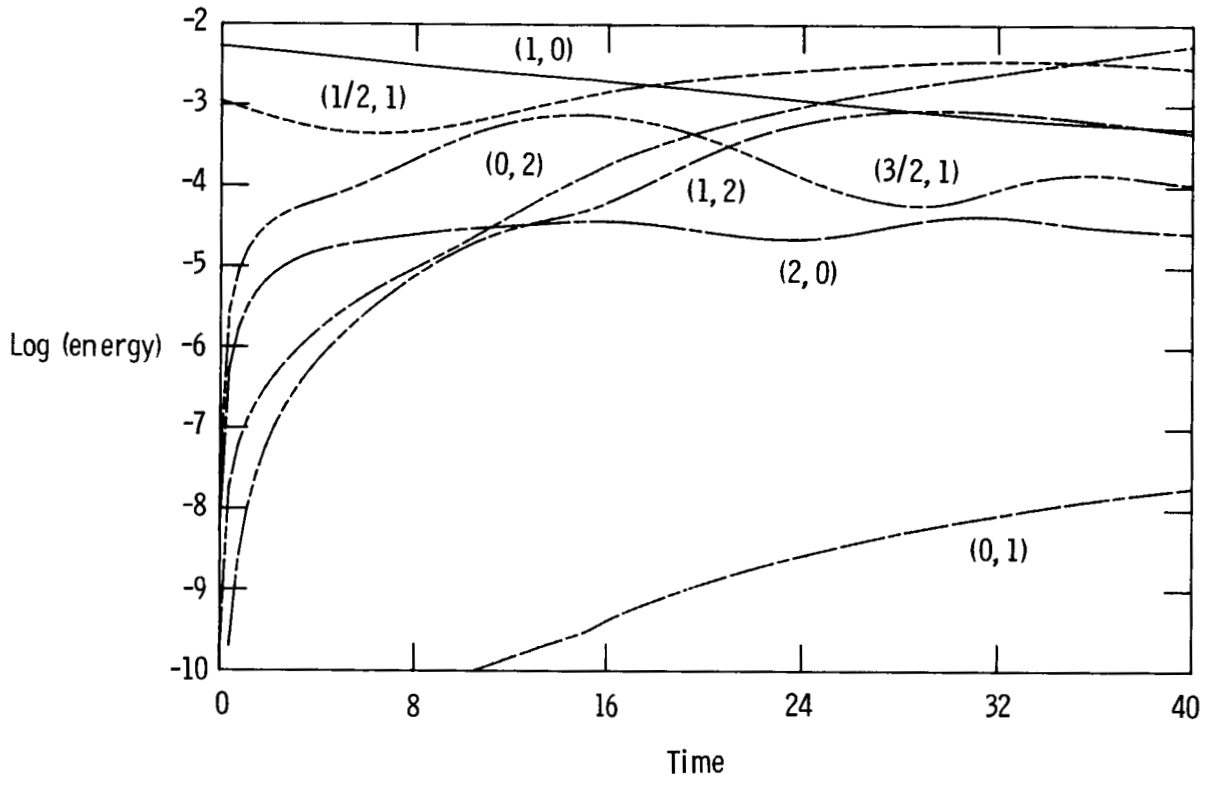

Figure 27. Kinetic energy in several (k_x, k_z) harmonics for the $R = 1500$, H-type transition.

ORIGINAL PAGE
COLOR PHOTOGRAPH

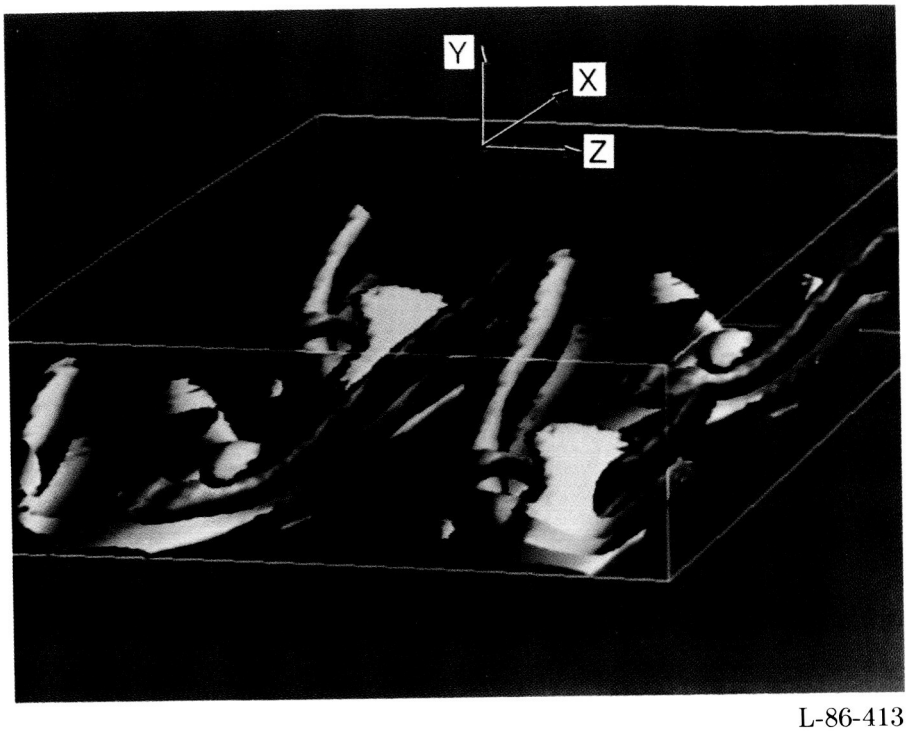

L-86-413

(a) Streamwise vorticity component.

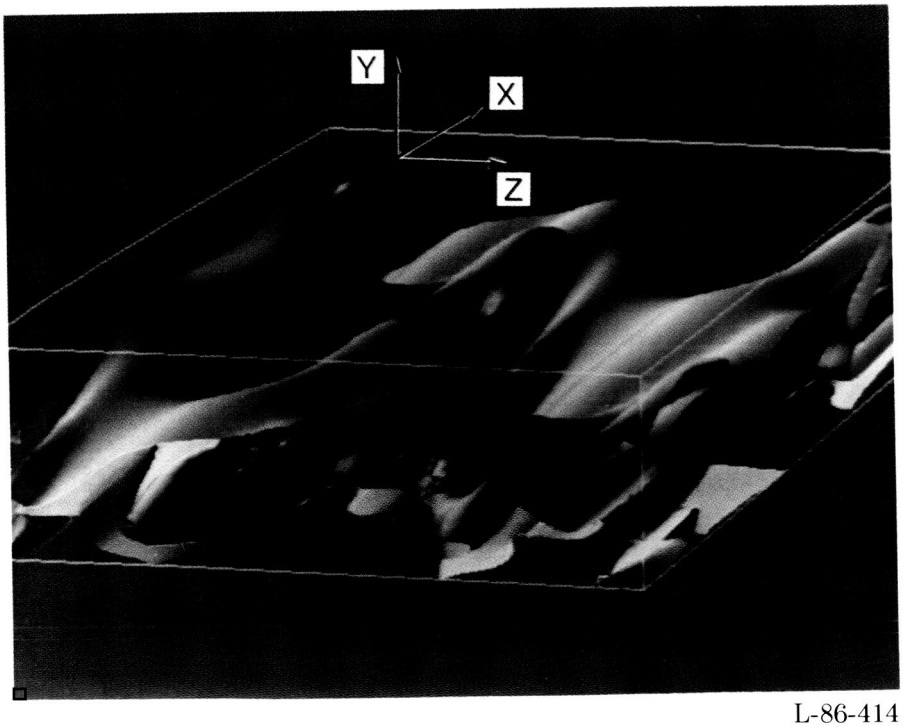

L-86-414

(b) Spanwise vorticity component.

Figure 28. Vorticity components of the $R = 1500$, H-type transition at $t = 30$.

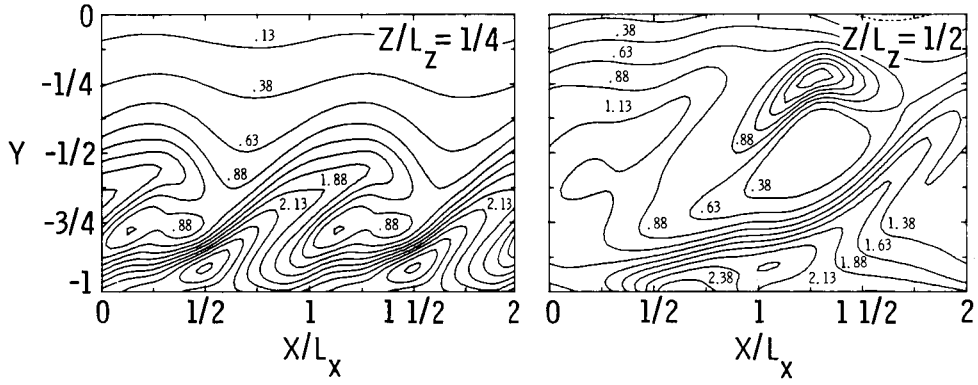

Figure 29. Vertical shear at $Z/L_z = 1/4$ and in one peak plane ($Z/L_z = 1/2$) for the $R = 1500$, H-type transition at $t = 30$.

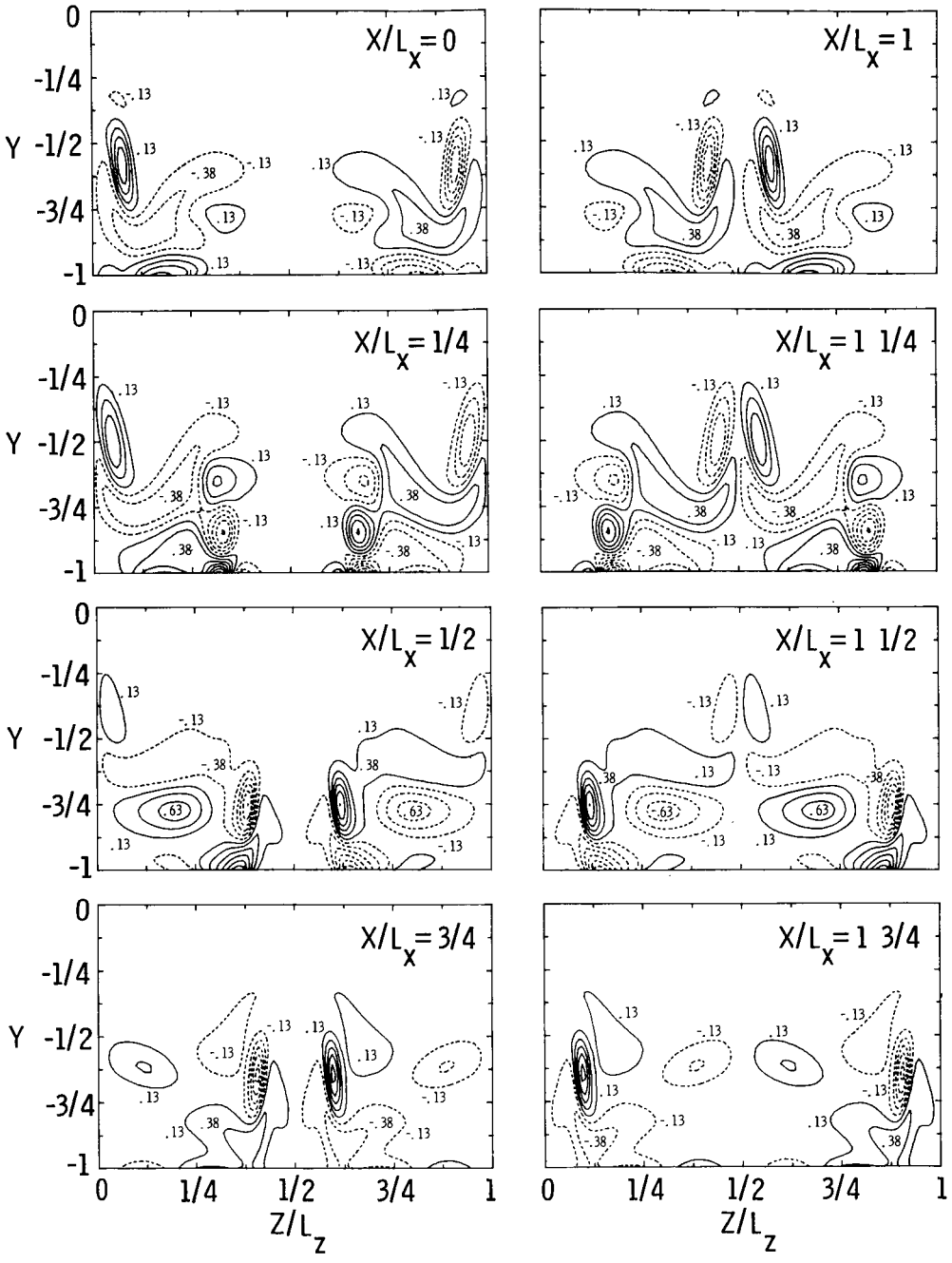

(a) Streamwise vorticity.

Figure 30. Vorticity contours for the $R = 1500$, H-type transition at $t = 30$.

ORIGINAL PAGE IS
OF POOR QUALITY

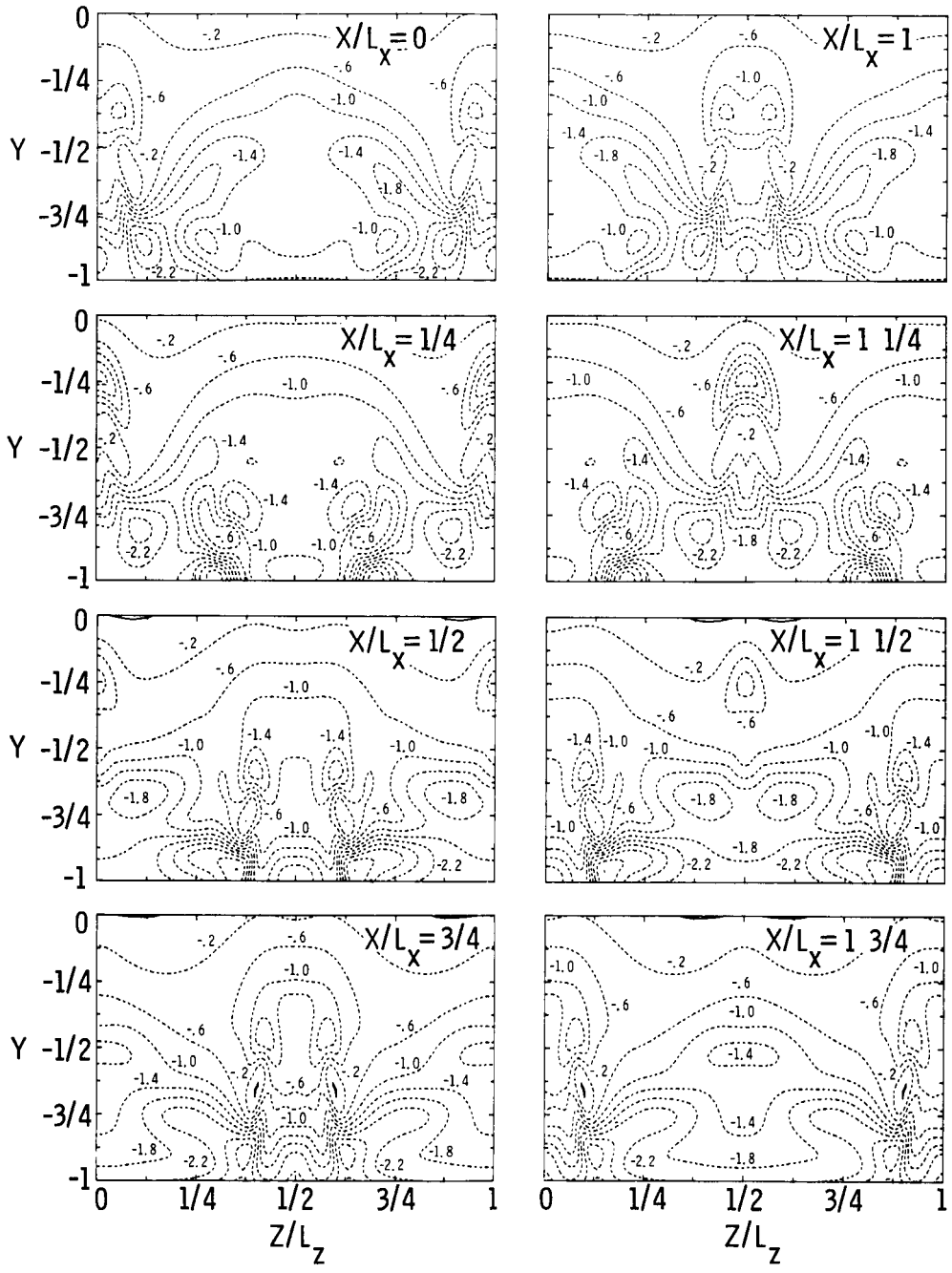

(b) Spanwise vorticity.

Figure 30. Concluded.

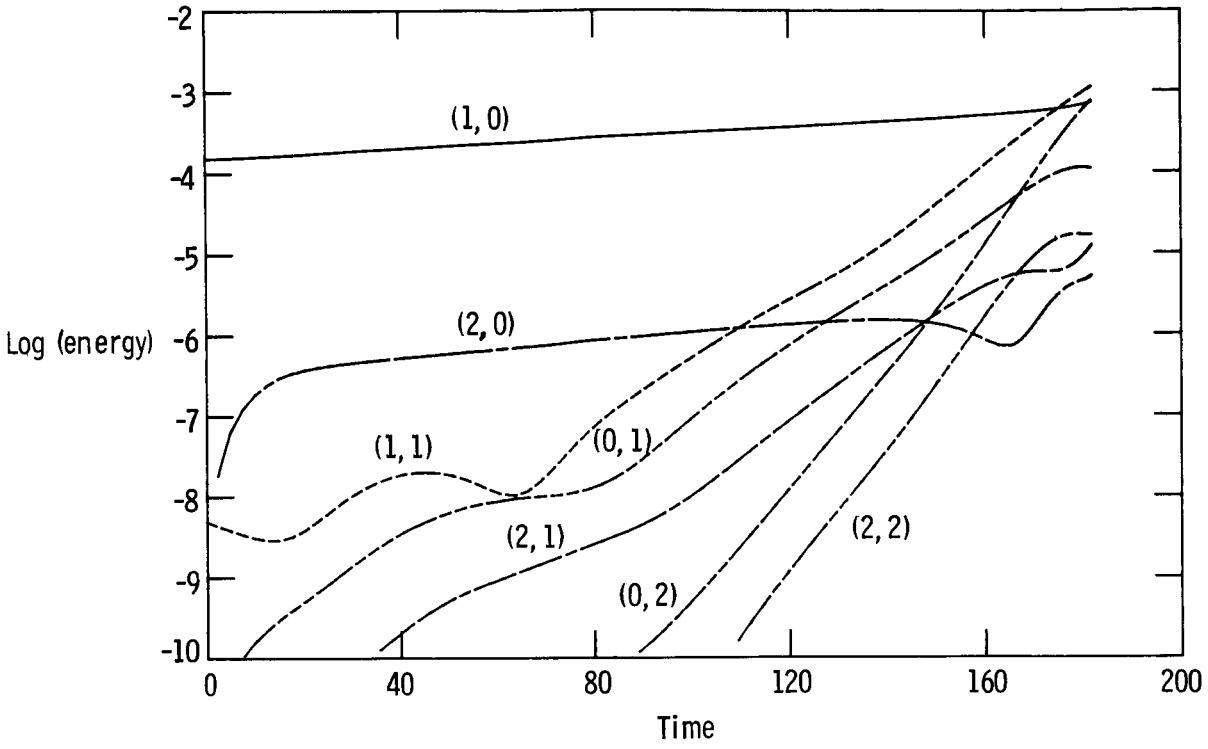

Figure 31. Kinetic energy in several (k_x, k_z) harmonics for the $R = 8000$, K-type transition.

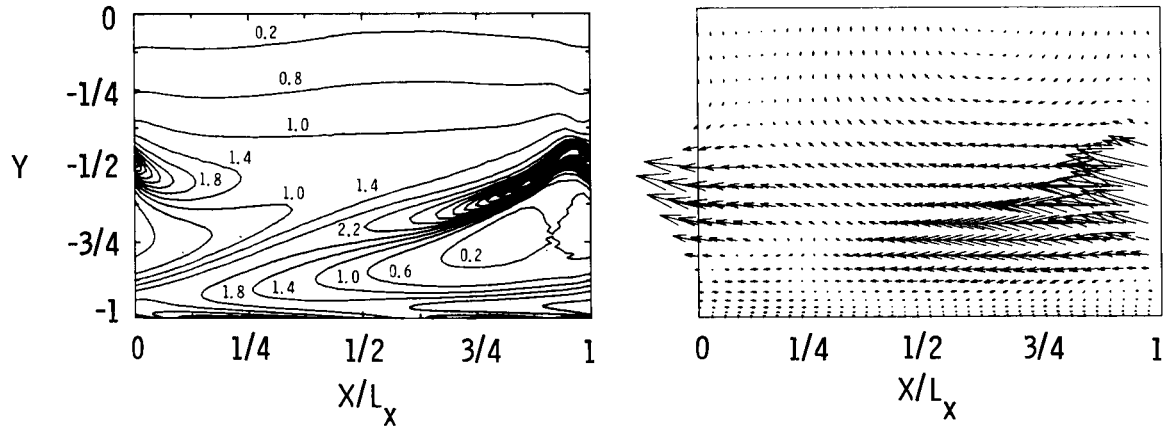

Figure 32. Vertical shear (left) and perturbation u-v velocity vectors (right) in the peak plane for the $R = 8000$, K-type transition at $t = 182.21$.

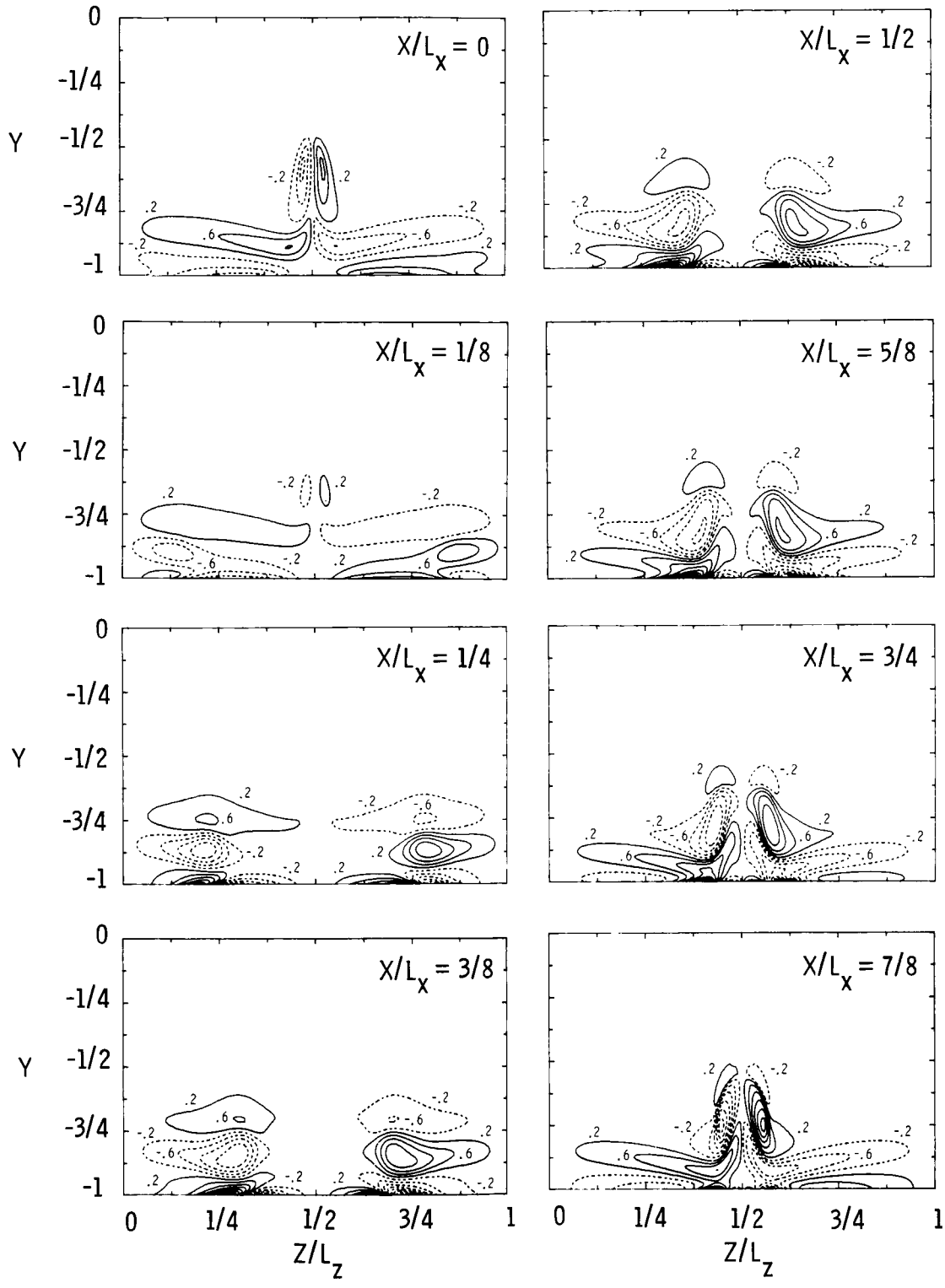

(a) Streamwise vorticity.

Figure 33. Vorticity contours for the $R = 8000$, K-type transition at $t = 182.21$.

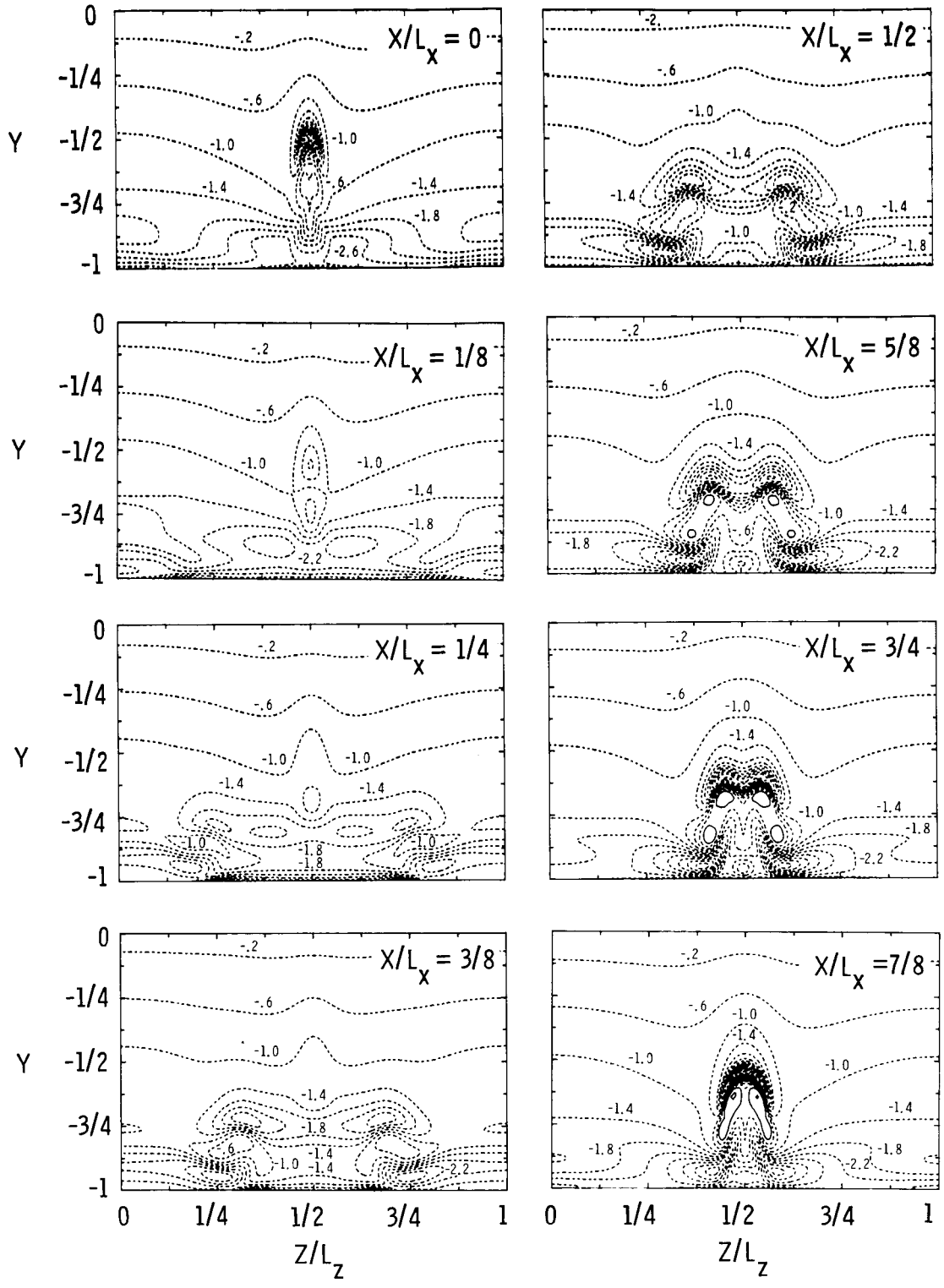

(b) Spanwise vorticity.

Figure 33. Concluded.

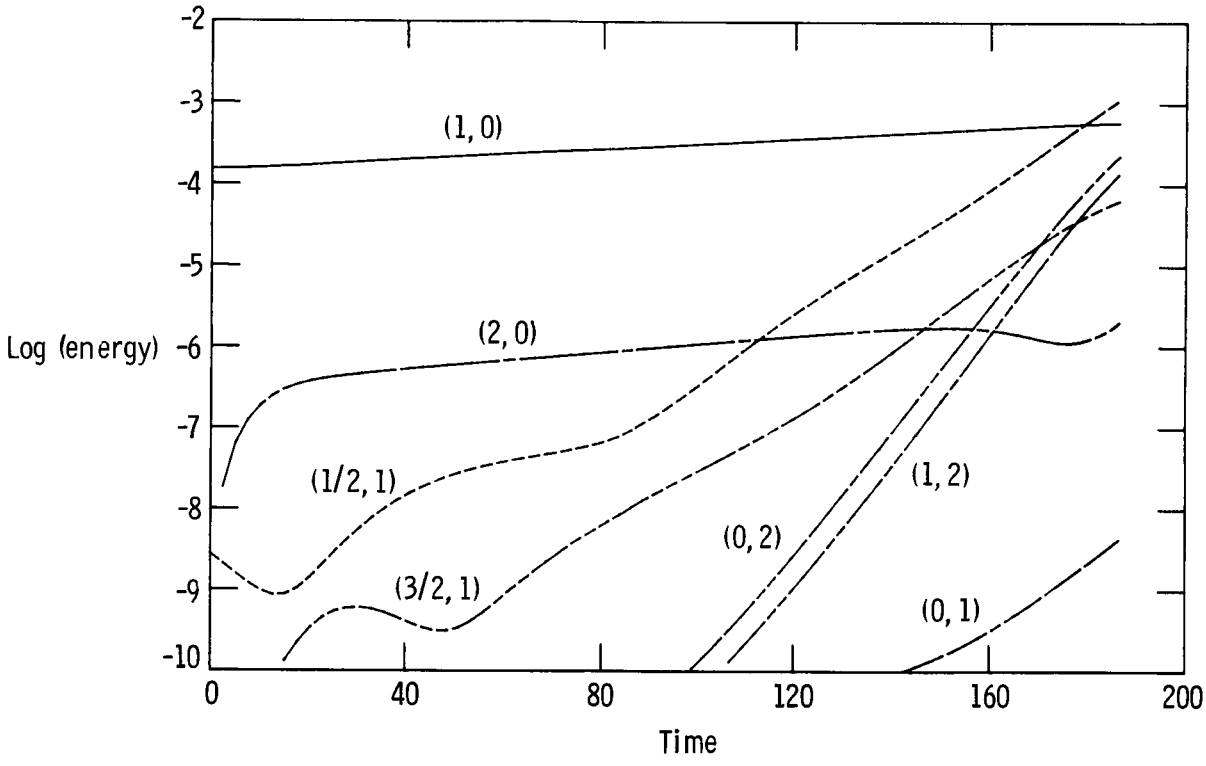

Figure 34. Kinetic energy in several (k_x, k_z) harmonics for the $R = 8000$, H-type transition.

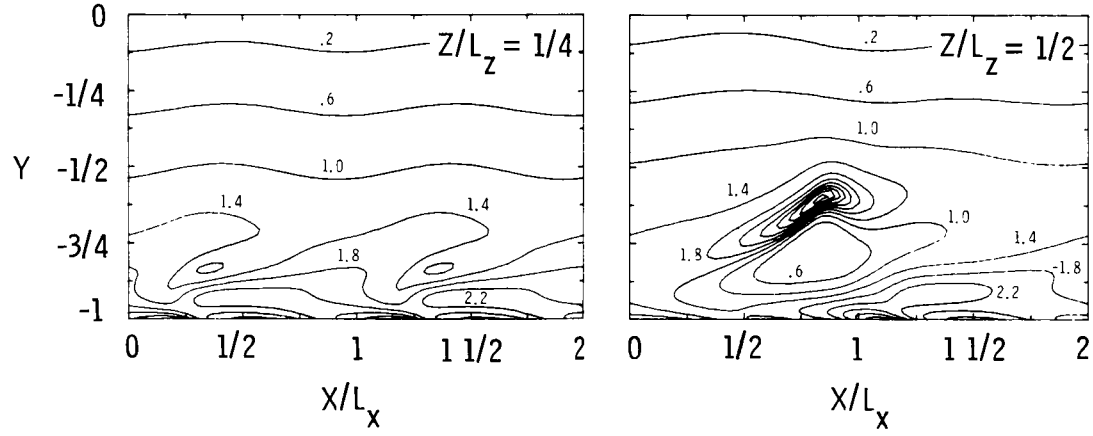

Figure 35. Vertical shear at $Z/L_z = 1/4$ and in one peak plane ($Z/L_z = 1/2$) for the $R = 8000$, H-type transition at $t = 184.45$.

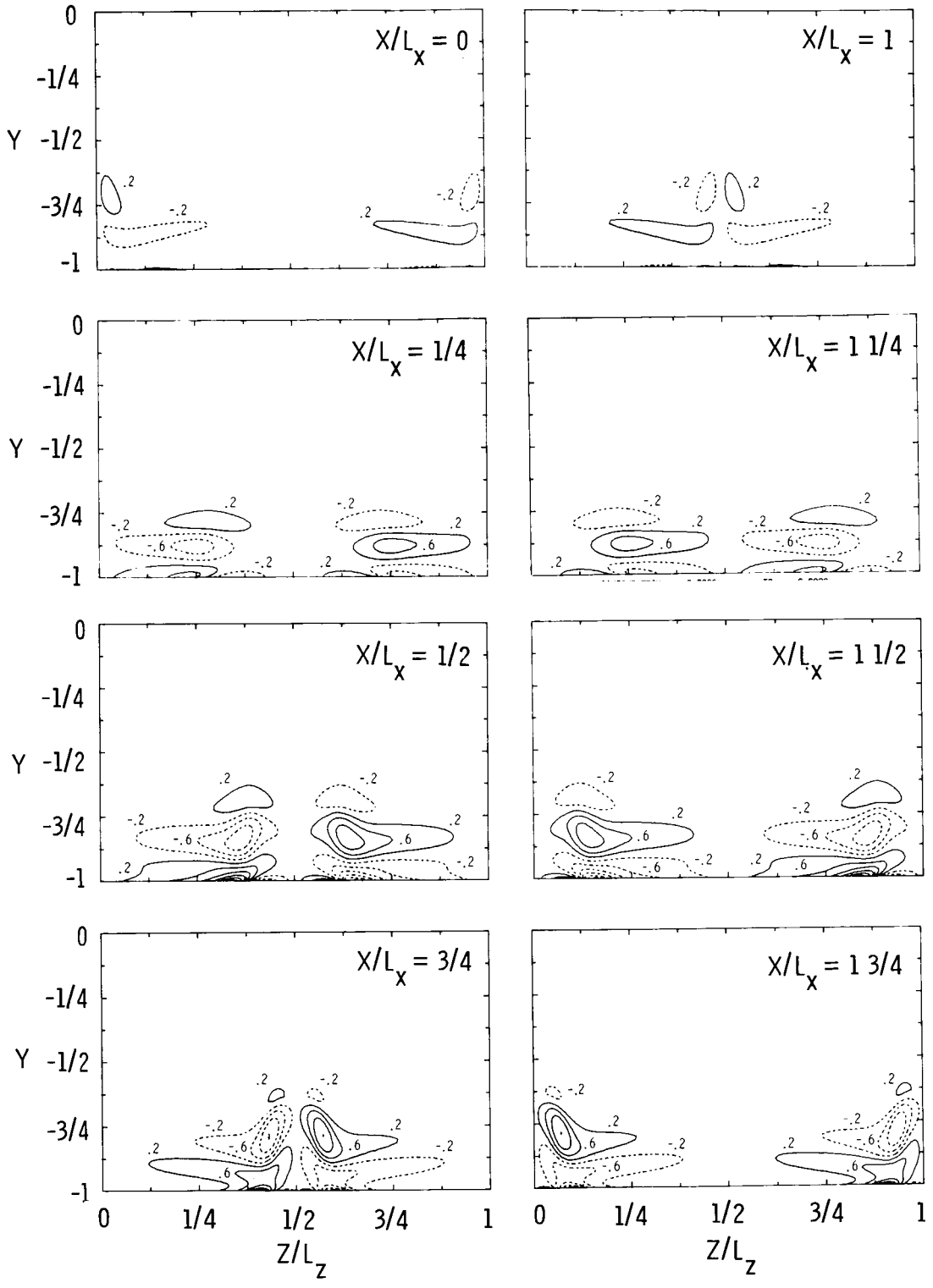

(a) Streamwise vorticity.

Figure 36. Vorticity contours for the $R = 8000$, H-type transition at $t = 184.45$.

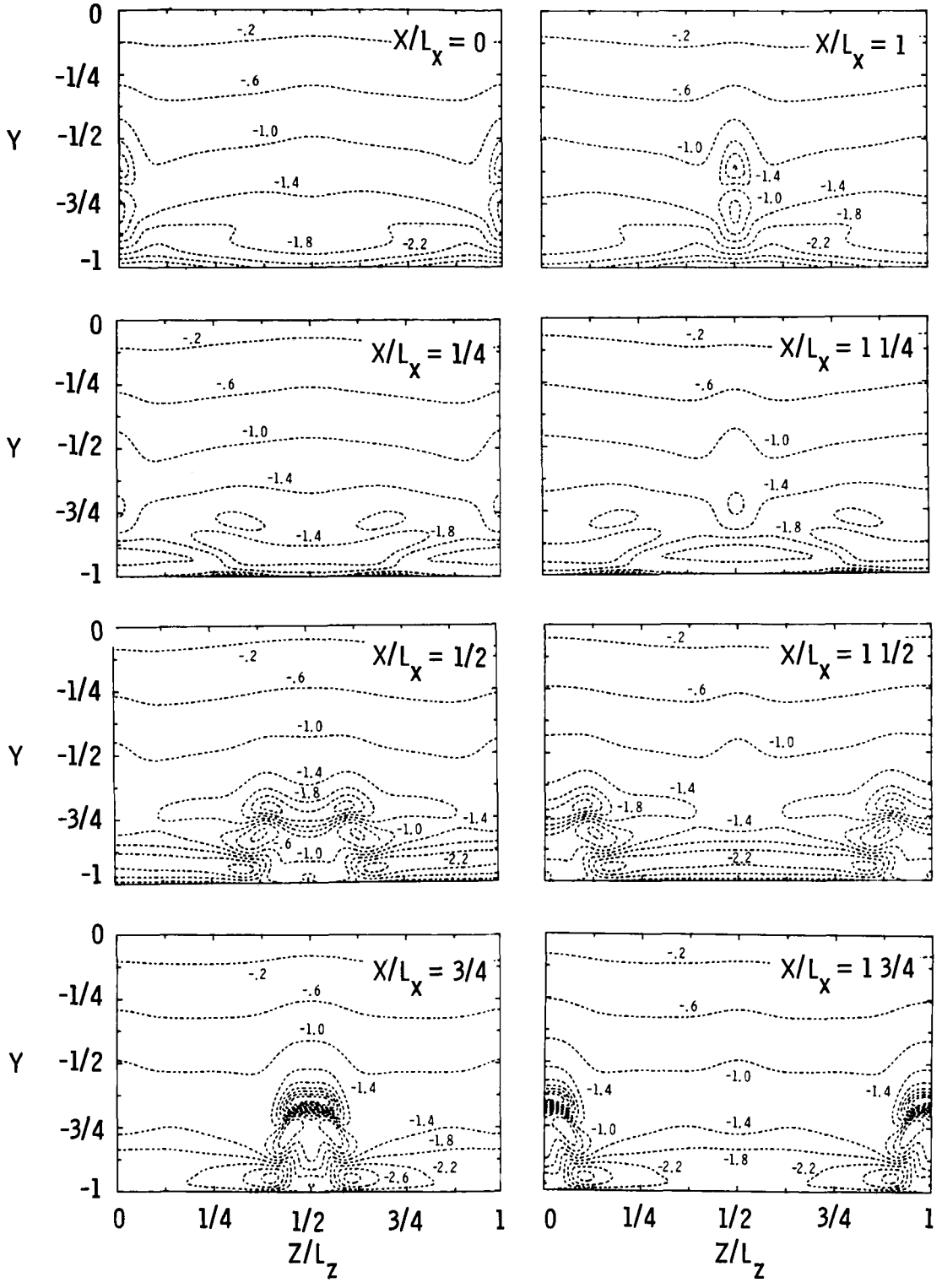

(b) Spanwise vorticity.

Figure 36. Concluded.

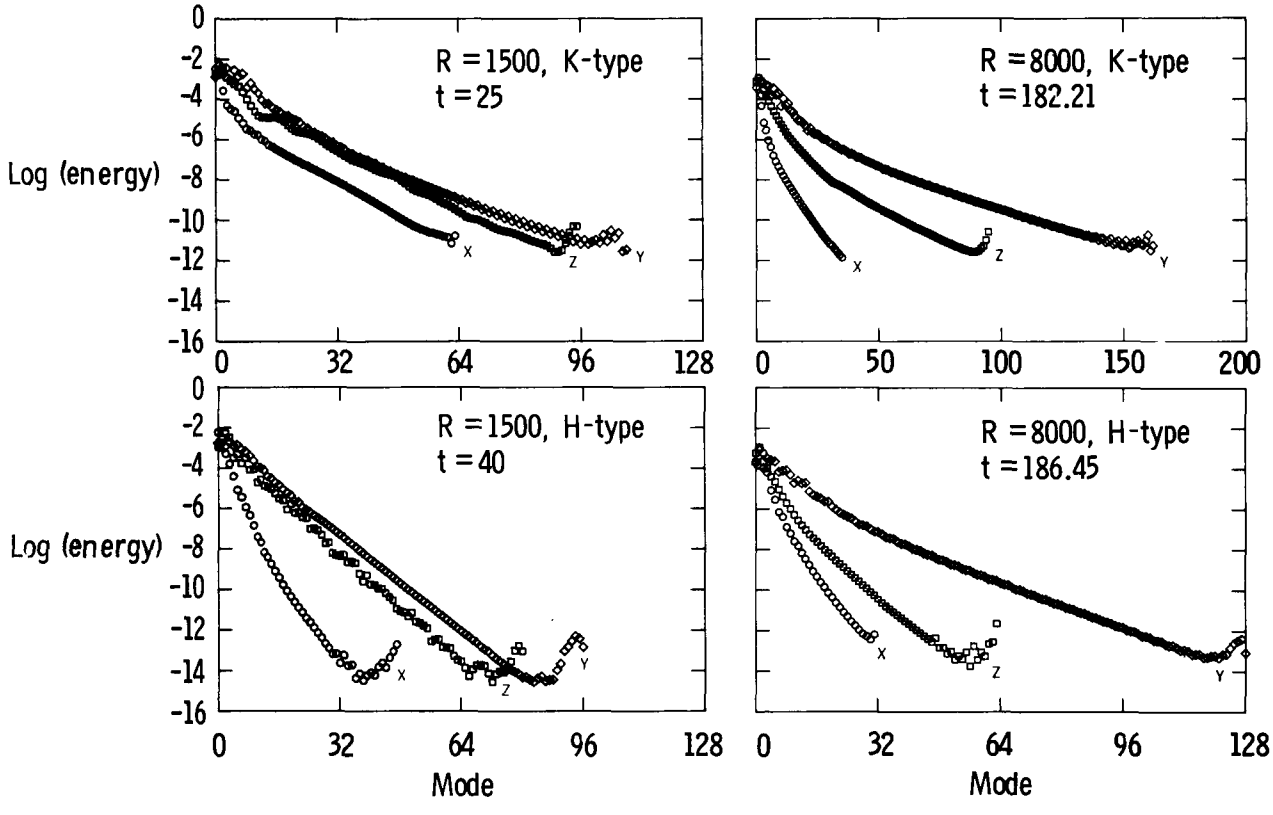

Figure 37. Energy spectra for the four transition simulations.

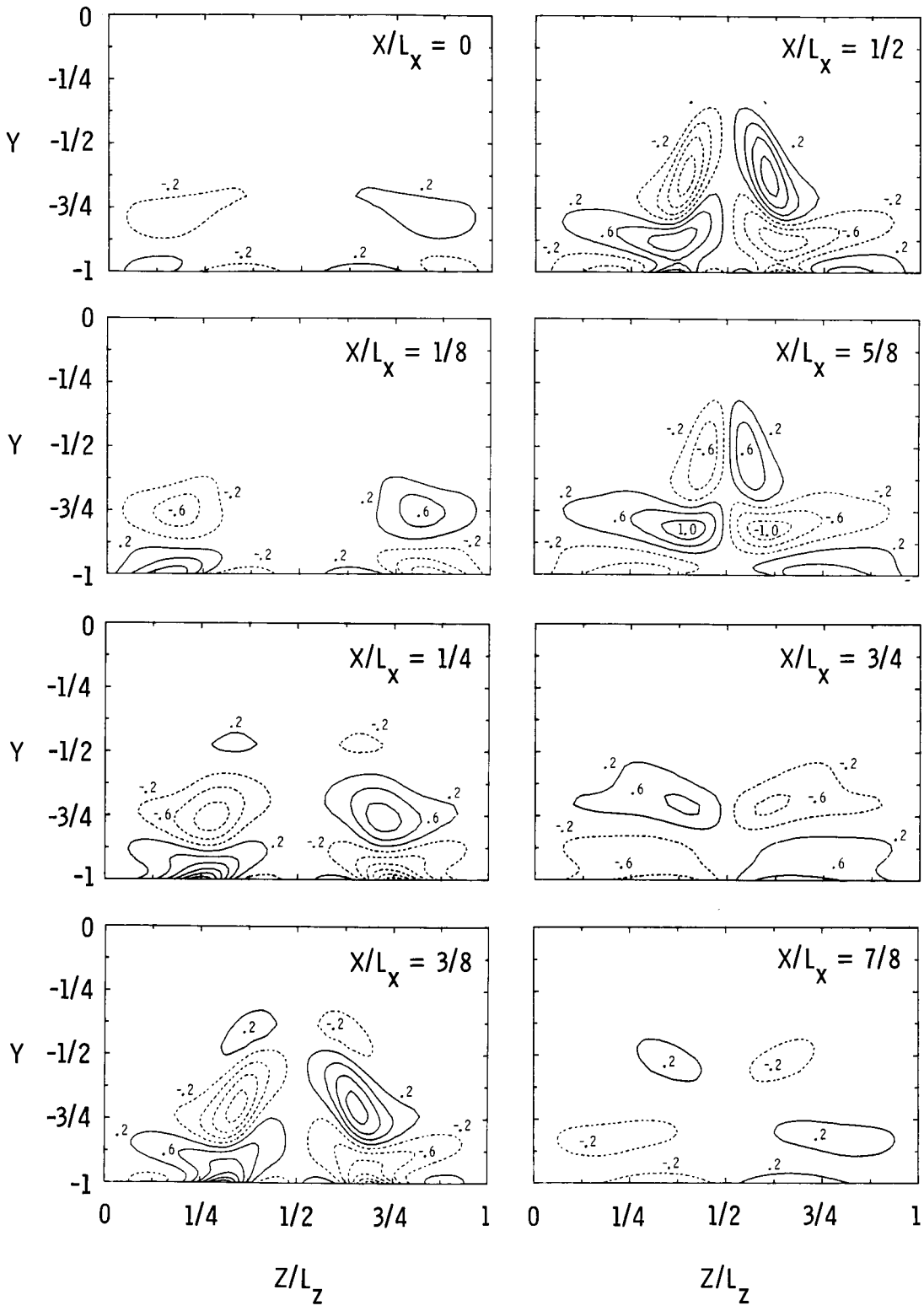

(a) Streamwise vorticity.

Figure 38. Vorticity contours for the $R = 1500$, K-type transition at $t = 15$.

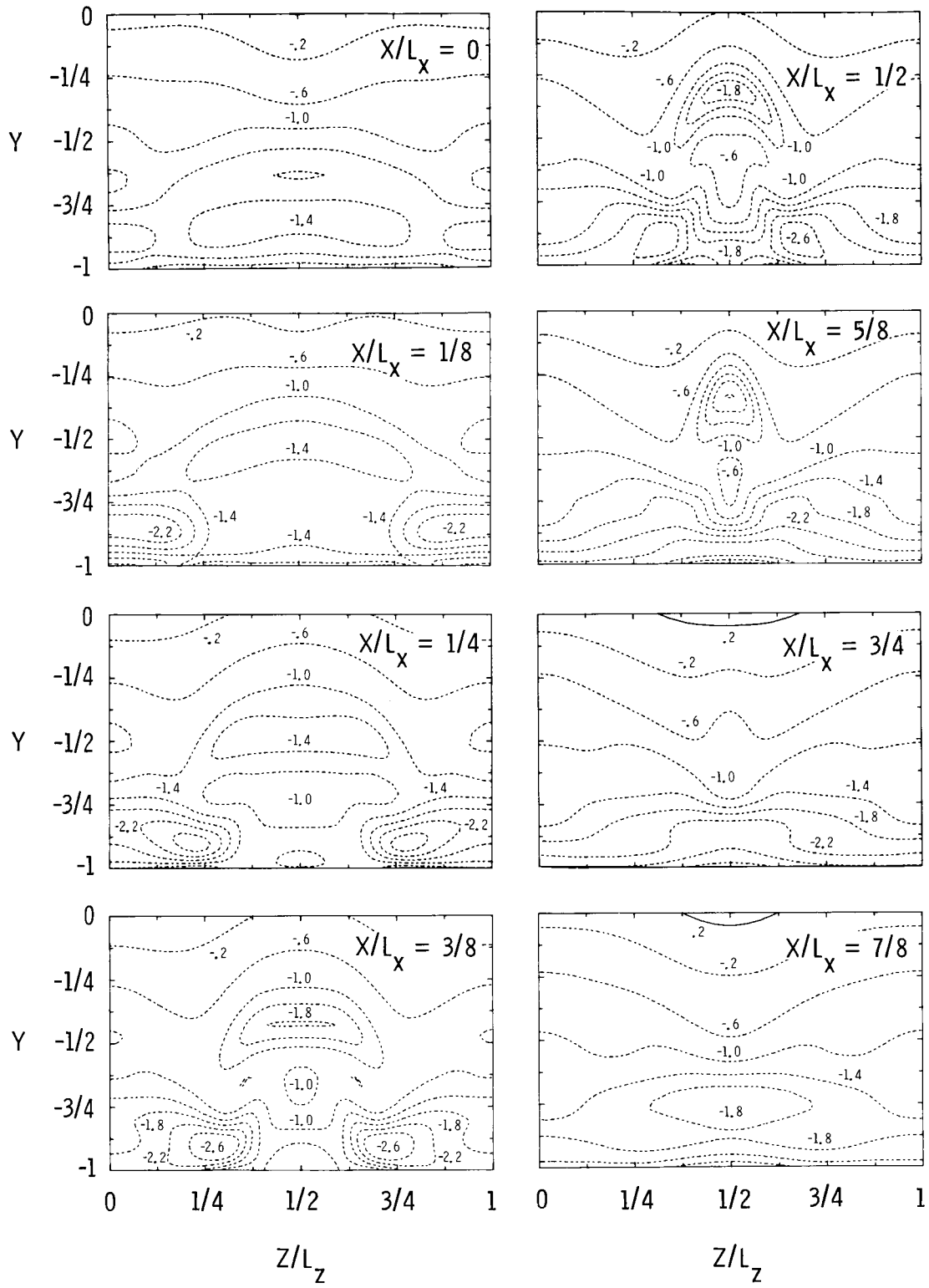

(b) Spanwise vorticity.

Figure 38. Concluded.

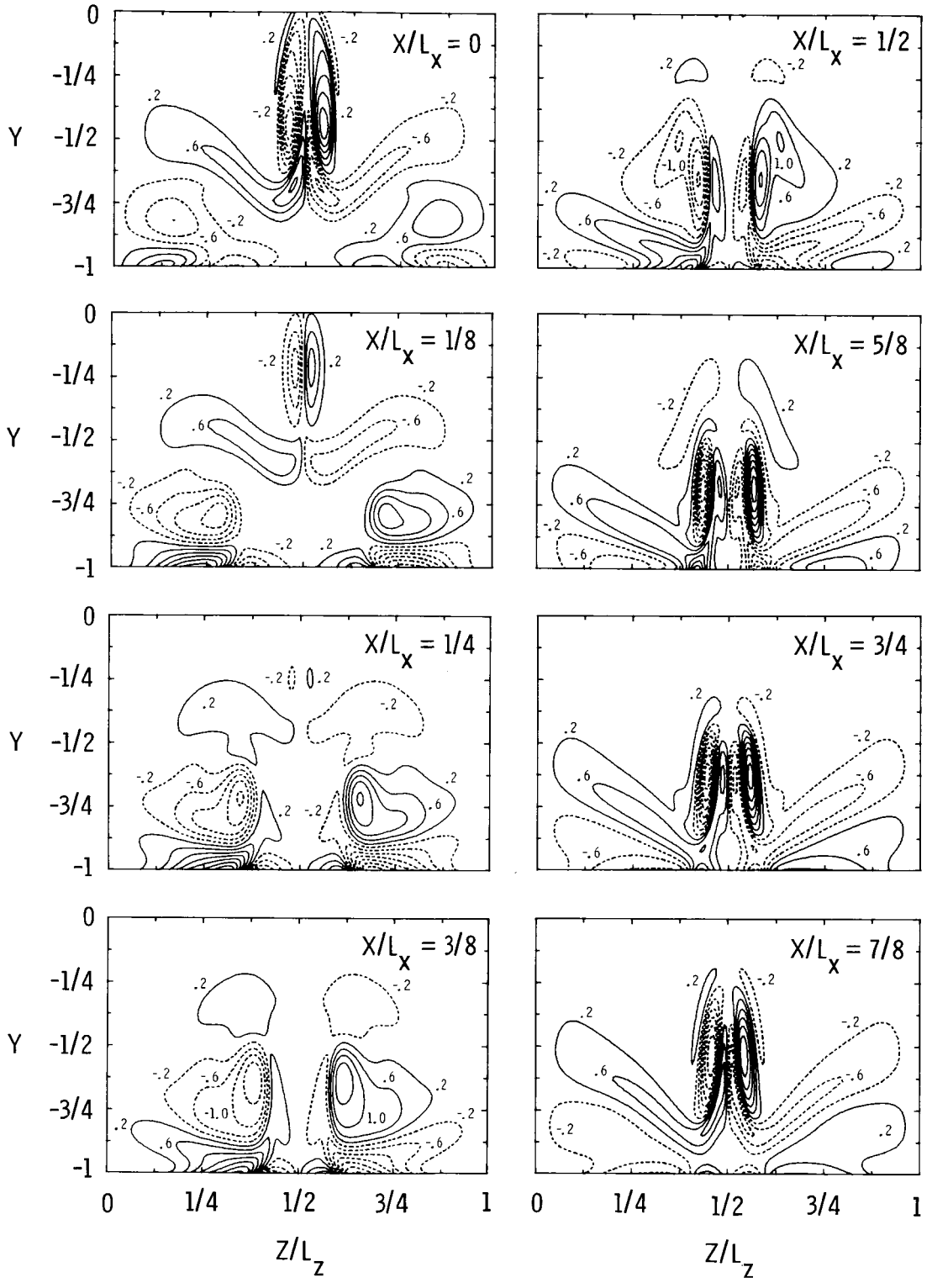

(a) Streamwise vorticity.

Figure 39. Vorticity contours for the $R = 1500$, K-type transition at $t = 22.5$.

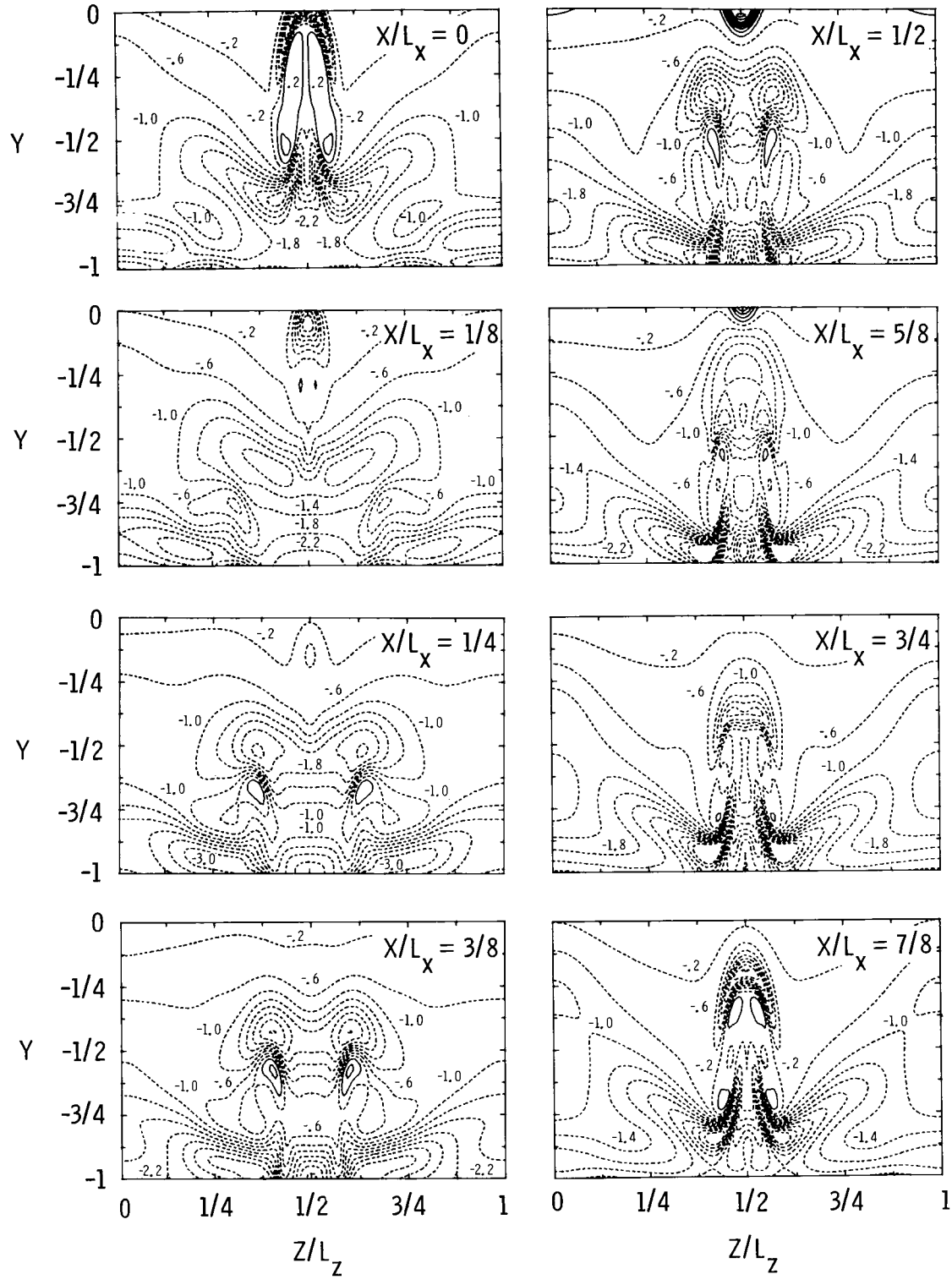

(b) Spanwise vorticity.

Figure 39. Concluded.

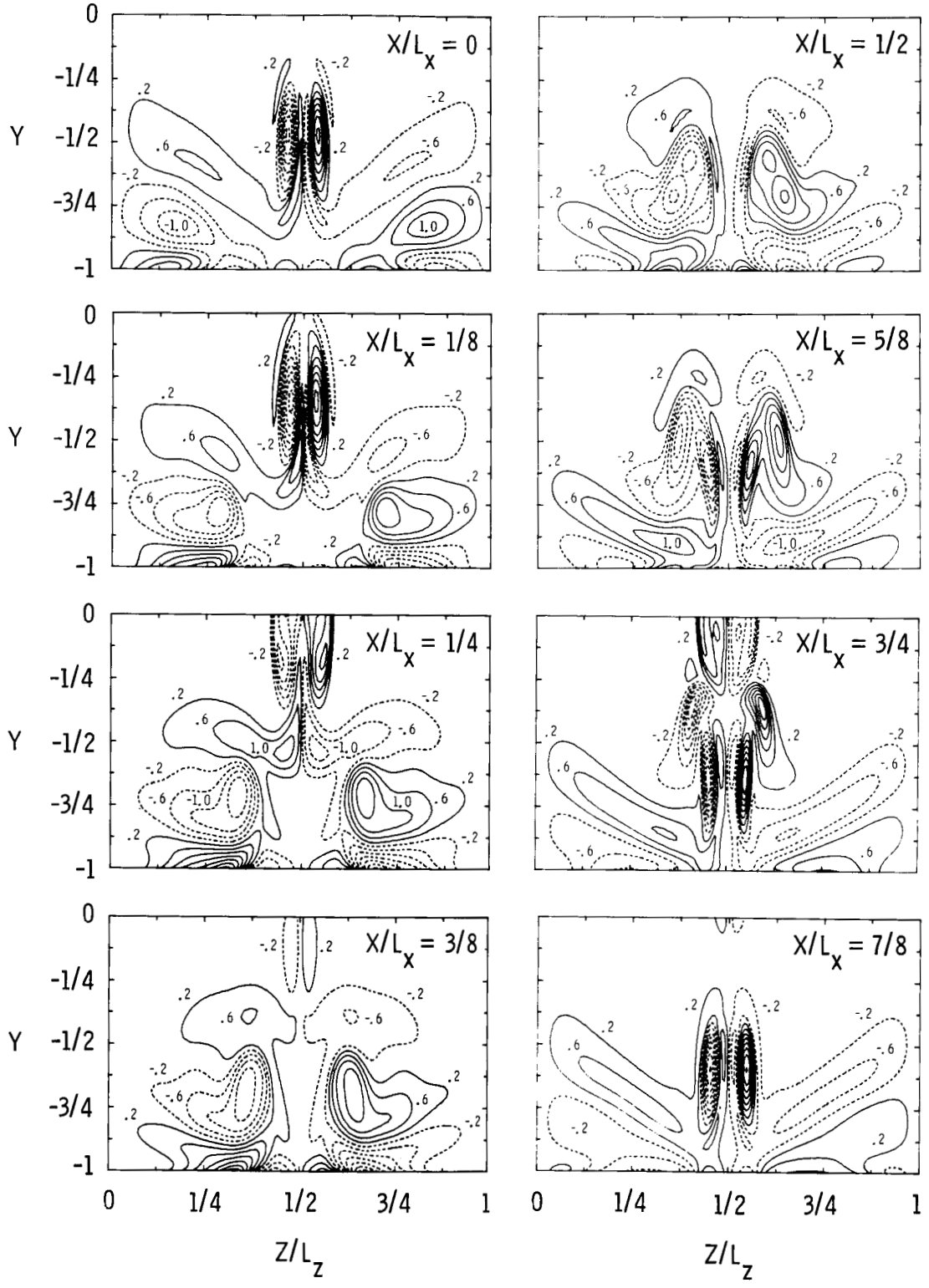

(a) Streamwise vorticity.

Figure 40. Vorticity contours for the $R = 1500$, K-type transition at $t = 25$.

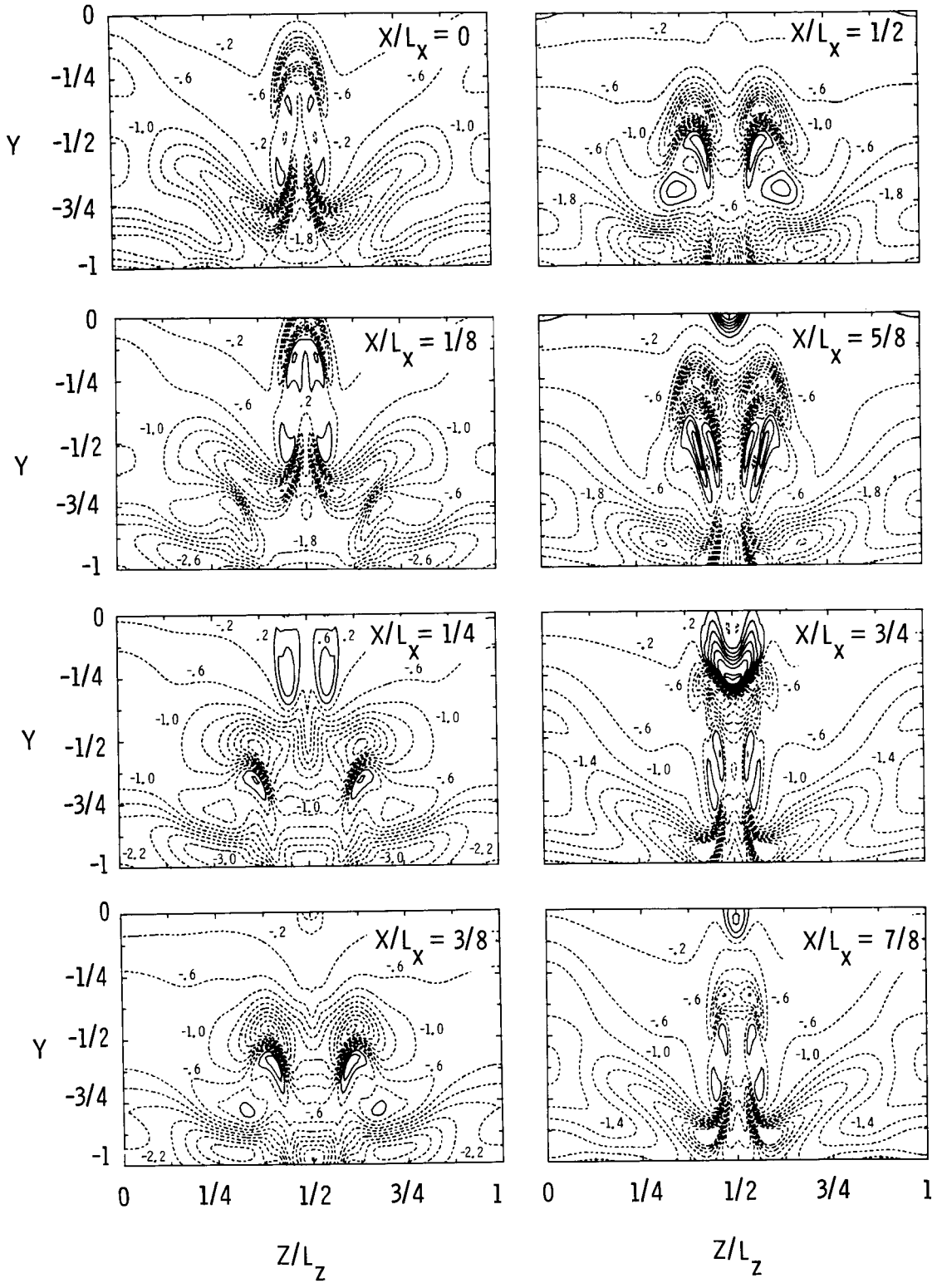

(b) Spanwise vorticity.

Figure 40. Concluded.

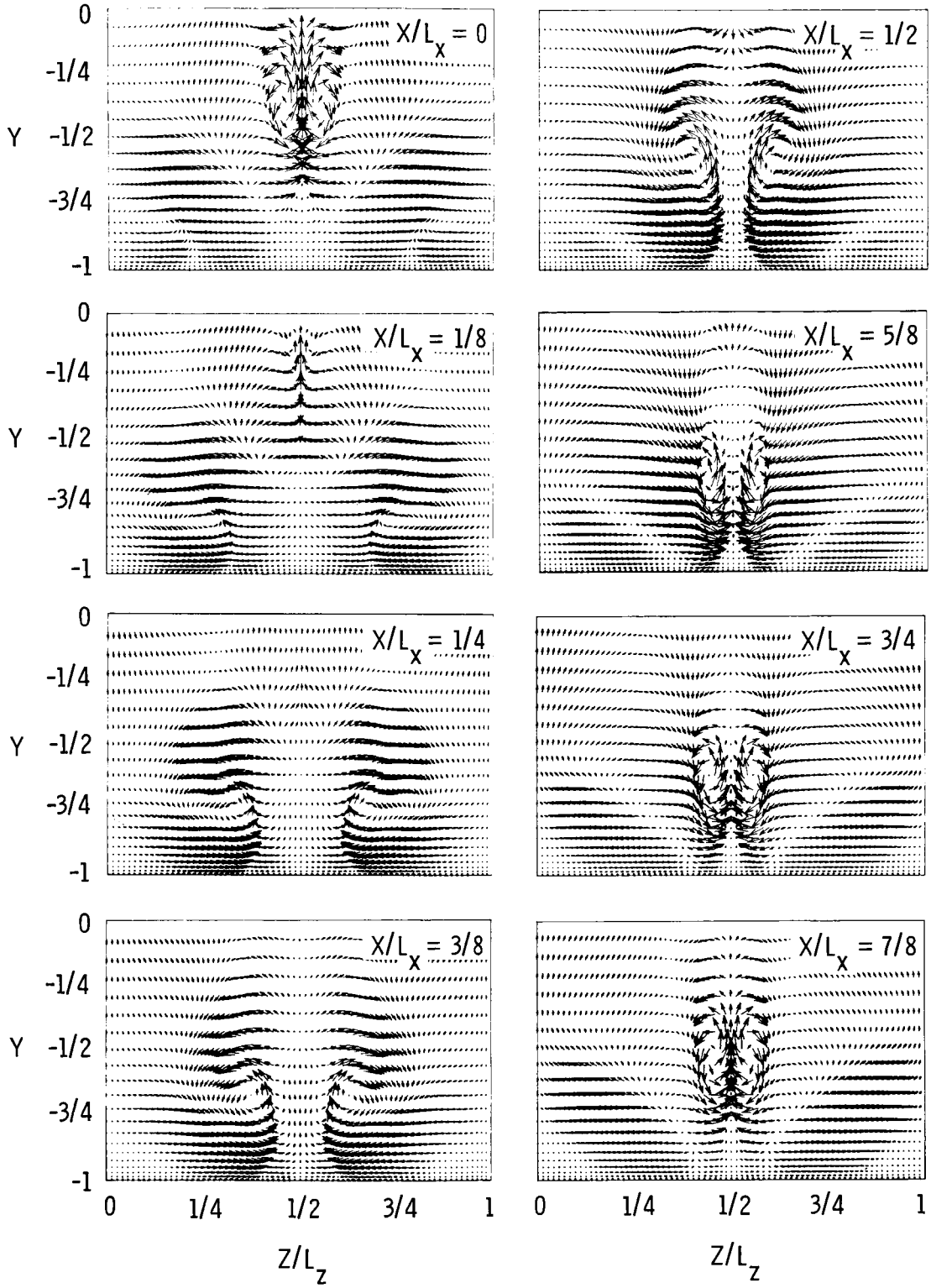

Figure 41. Cross-stream (v-w) velocity vectors for the $R = 1500$, K-type transition at $t = 22.5$.

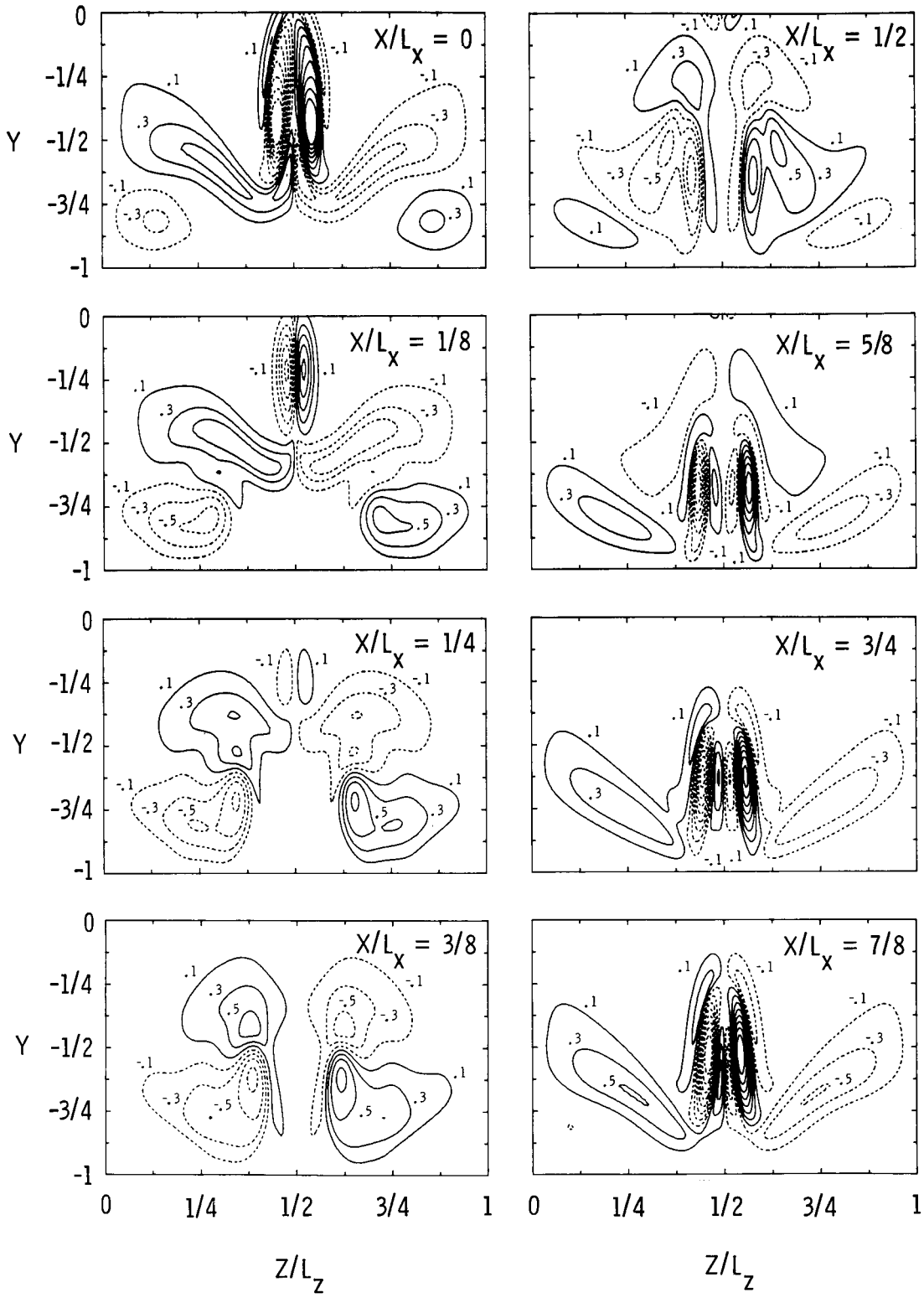

Figure 42. Helicity contours of the $R = 1500$, K-type transition at $t = 22.5$.

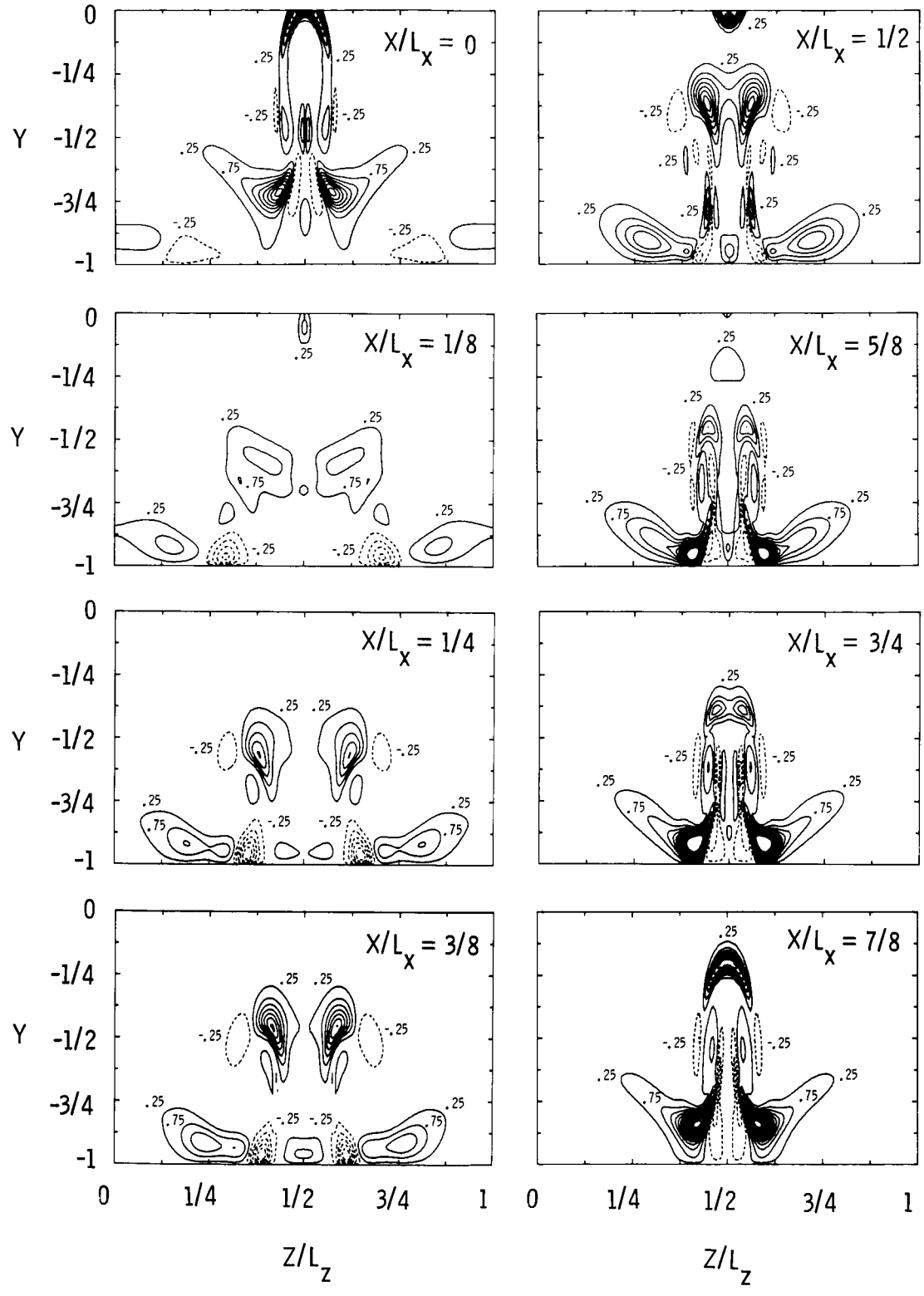

(a) Vortex stretching rate.

Figure 43. Vortex stretching and diffusion contours of the $R = 1500$, K-type transition at $t = 22.5$.

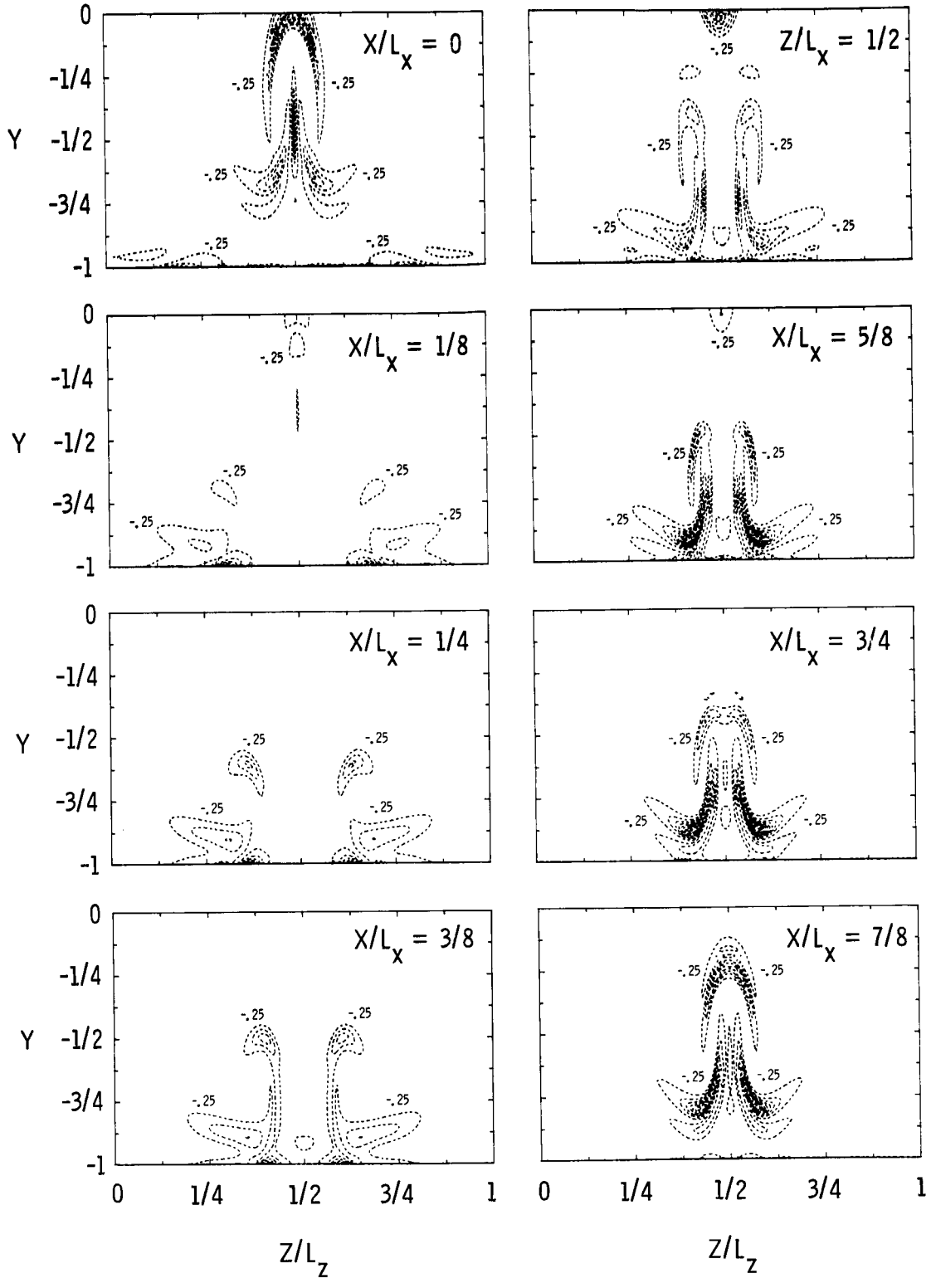

(b) Vortex diffusion rate.

Figure 43. Continued.

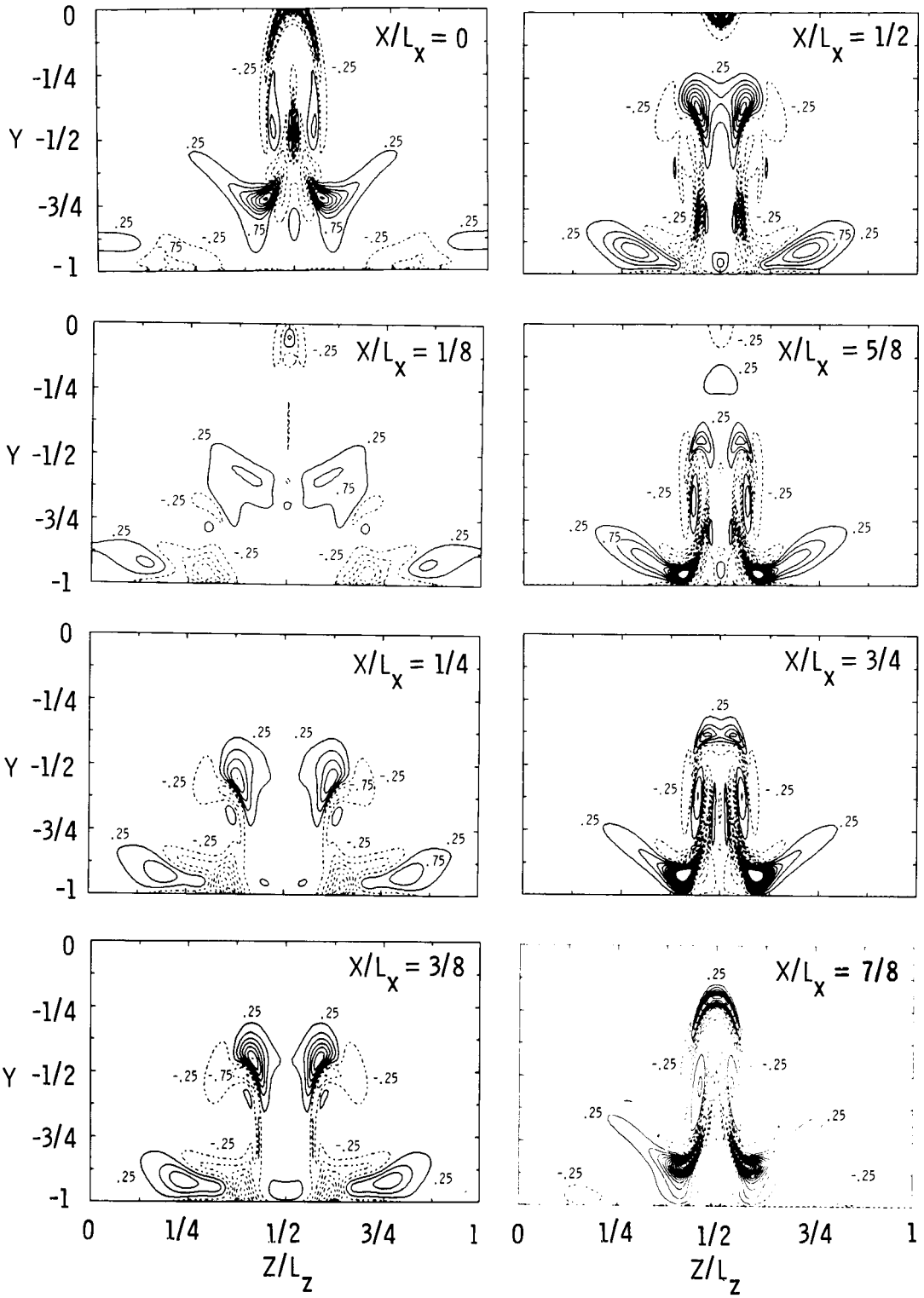

(c) Total vorticity rate of change.

Figure 43. Concluded.

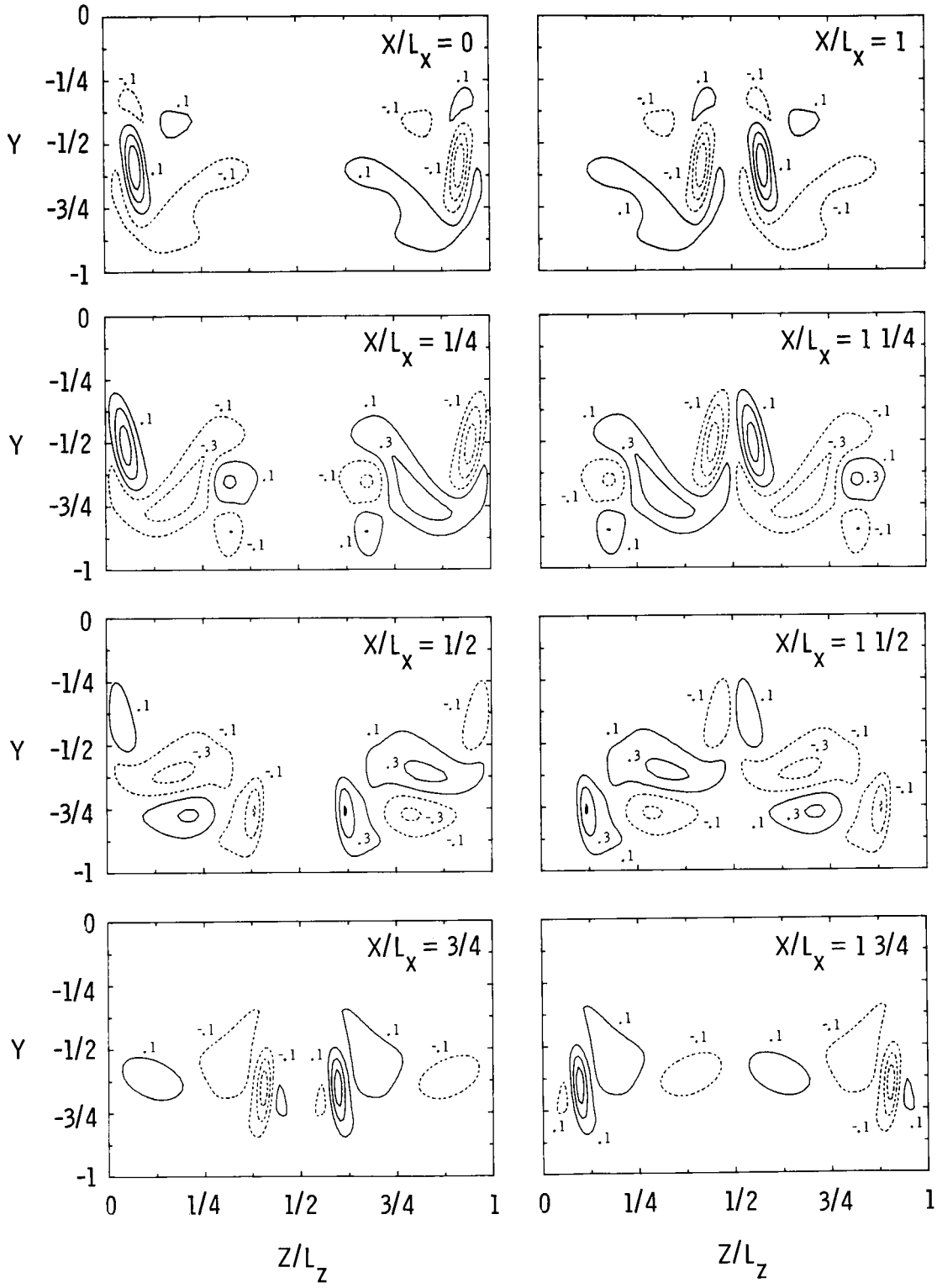

Figure 44. Helicity contours of the $R = 1500$, H-type transition at $t = 30$.

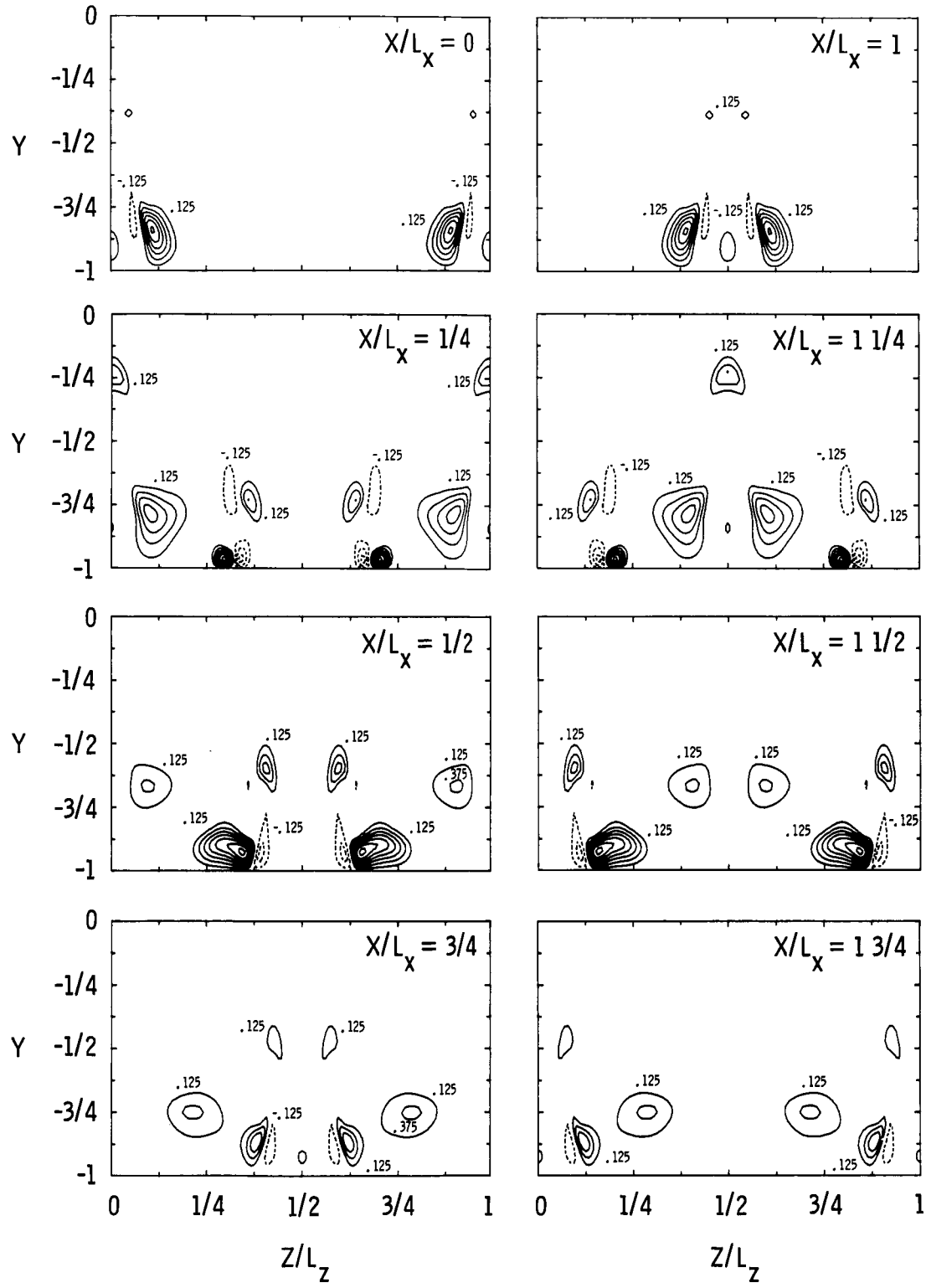

(a) Vortex stretching rate.

Figure 45. Vortex stretching and vortex diffusion of the $R = 1500$, H-type transition at $t = 30$.

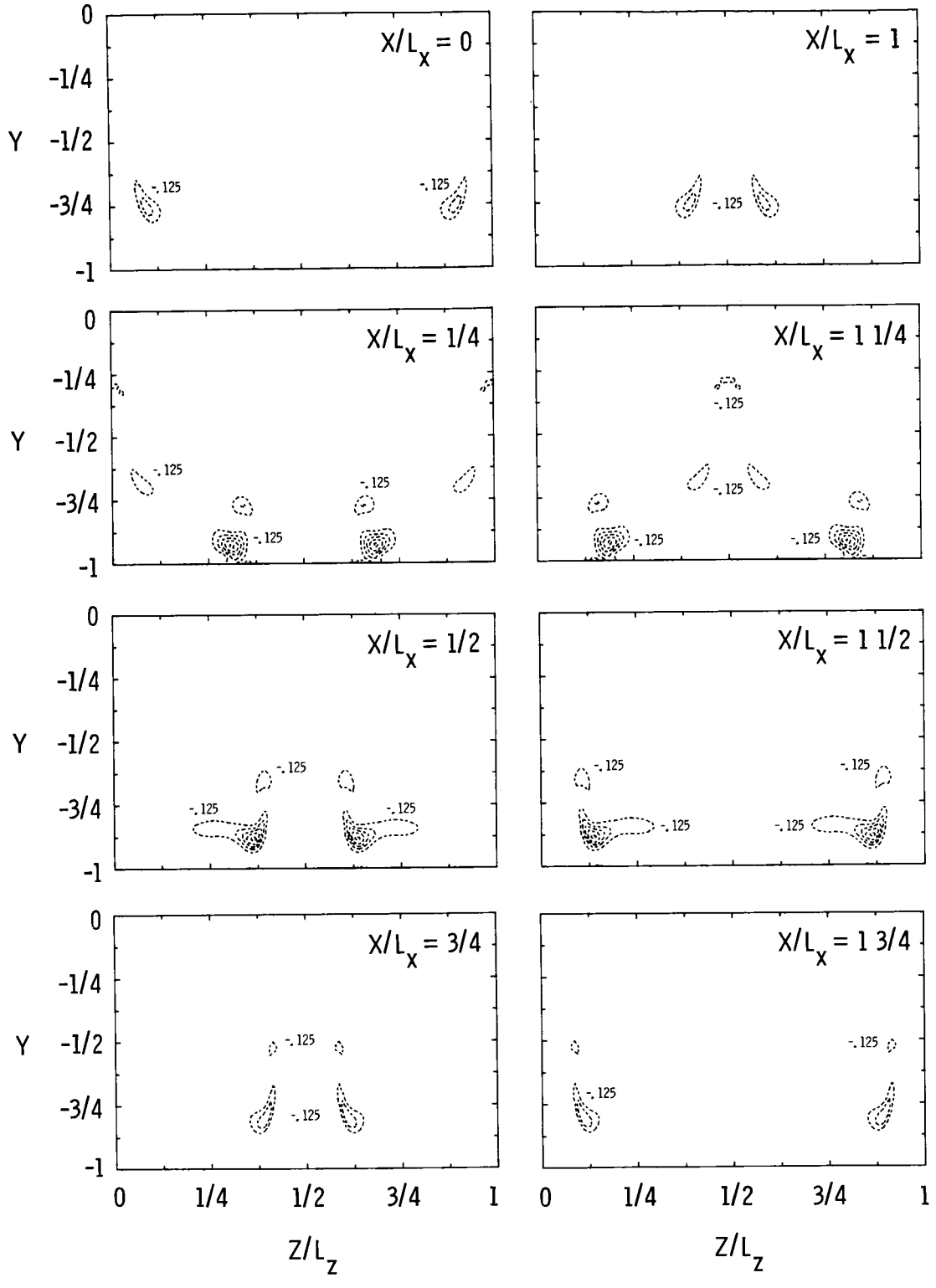

(b) Vortex diffusion rate.

Figure 45. Concluded.

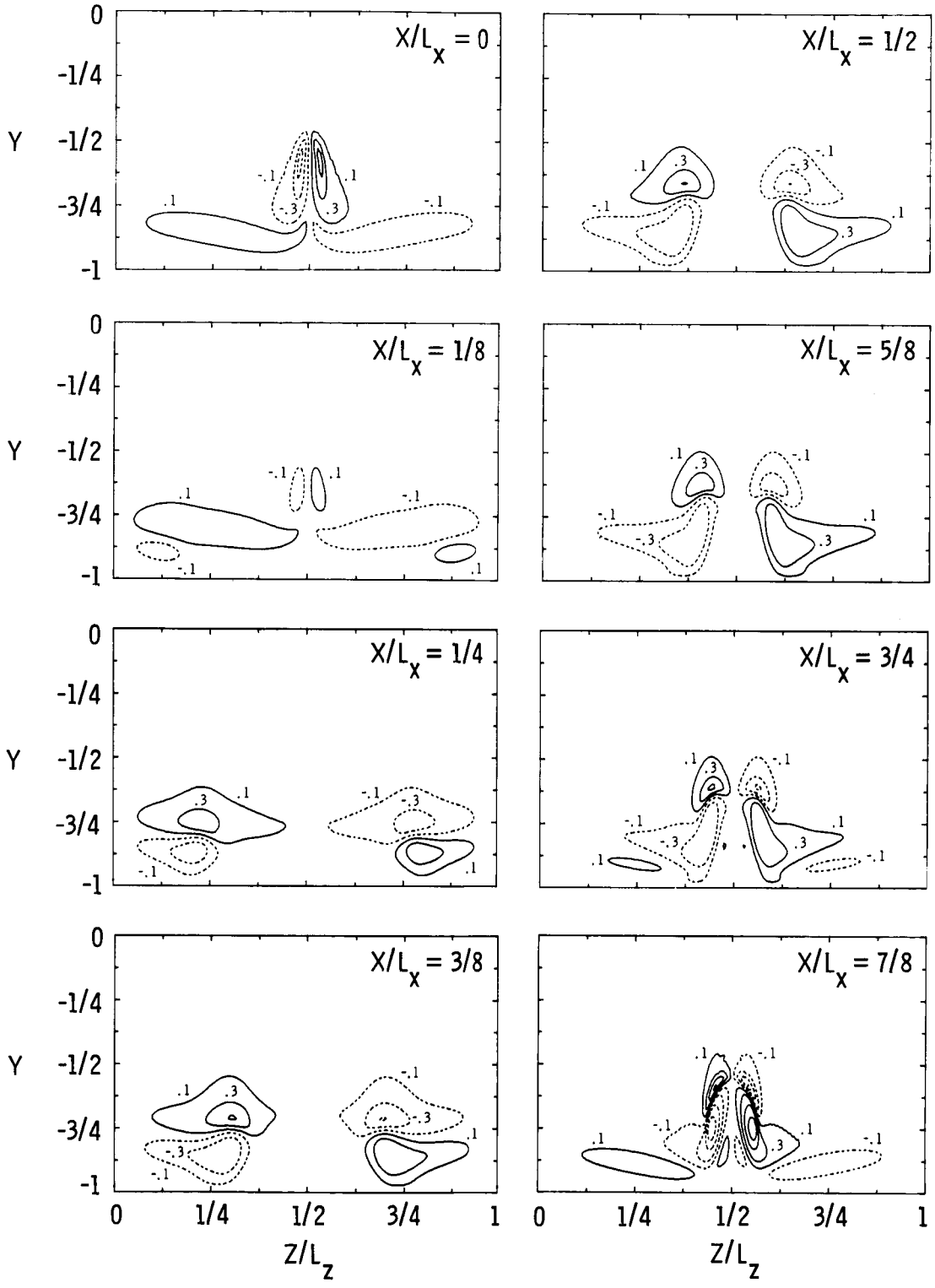

Figure 46. Helicity contours of the $R = 8000$, K-type transition at $t = 182.21$.

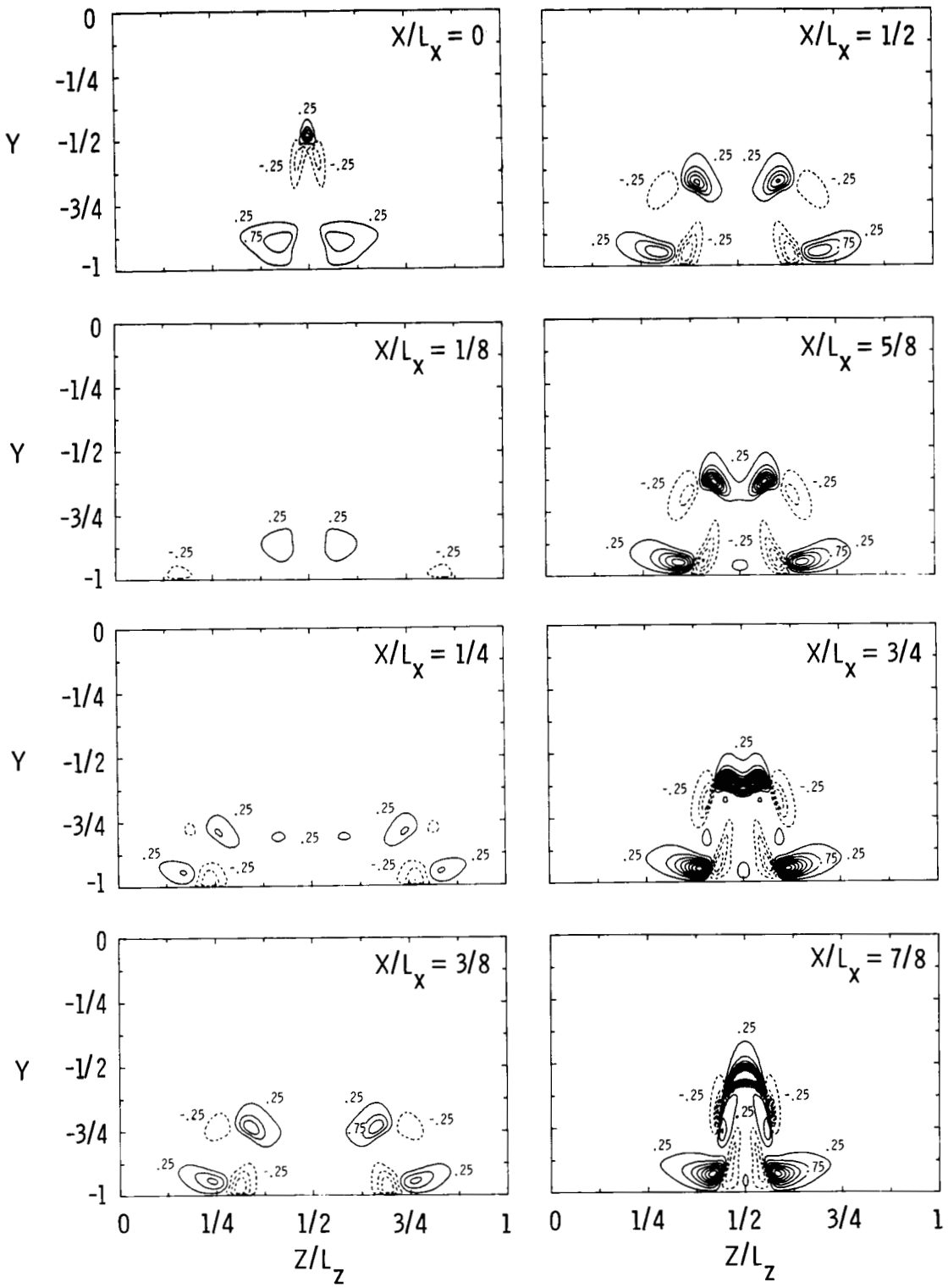

Figure 47. Vortex stretching rate of the $R = 8000$, K-type transition at $t = 182.21$.

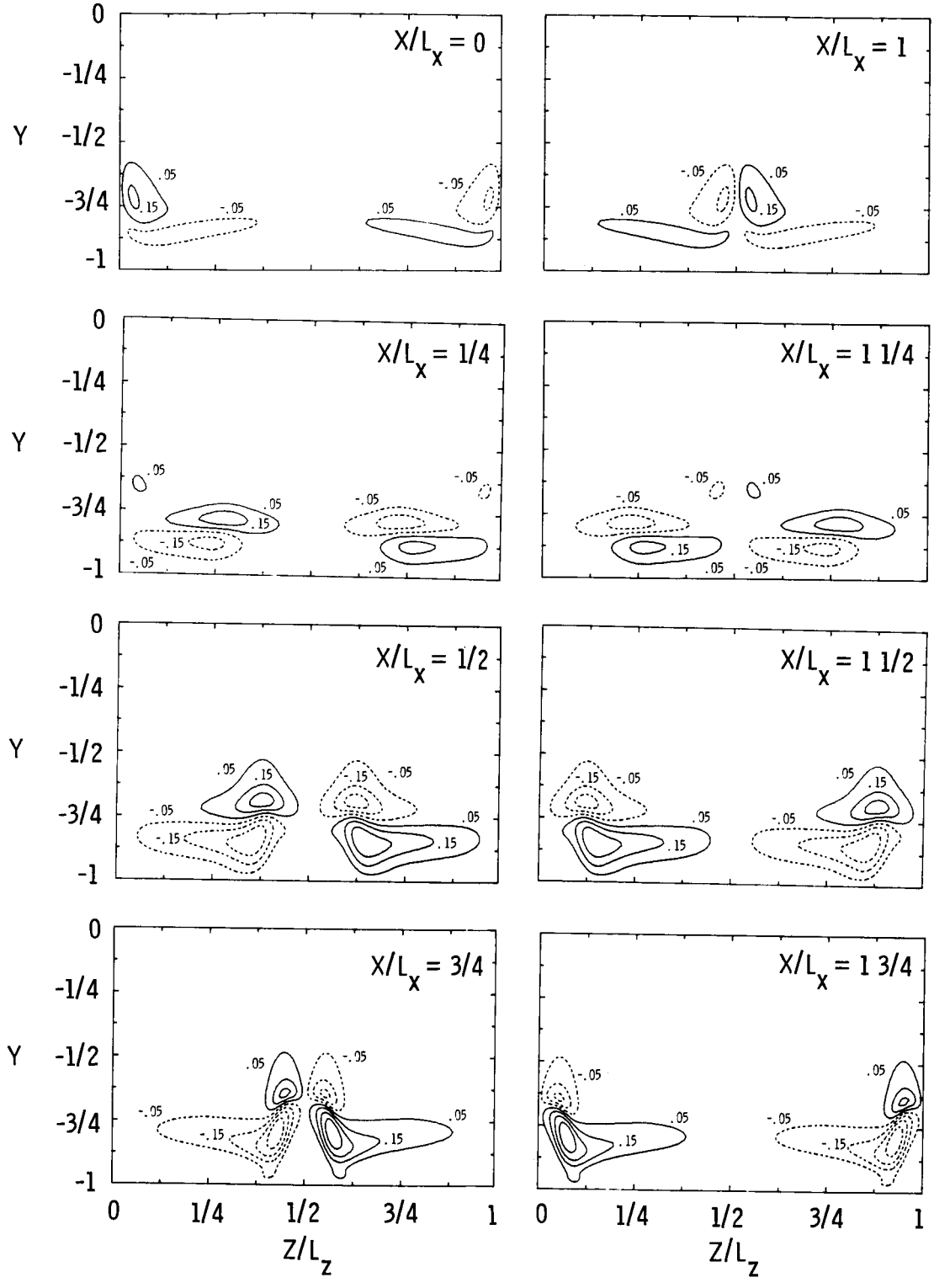

Figure 48. Helicity contours of the $R = 8000$, H-type transition at $t = 184.45$.

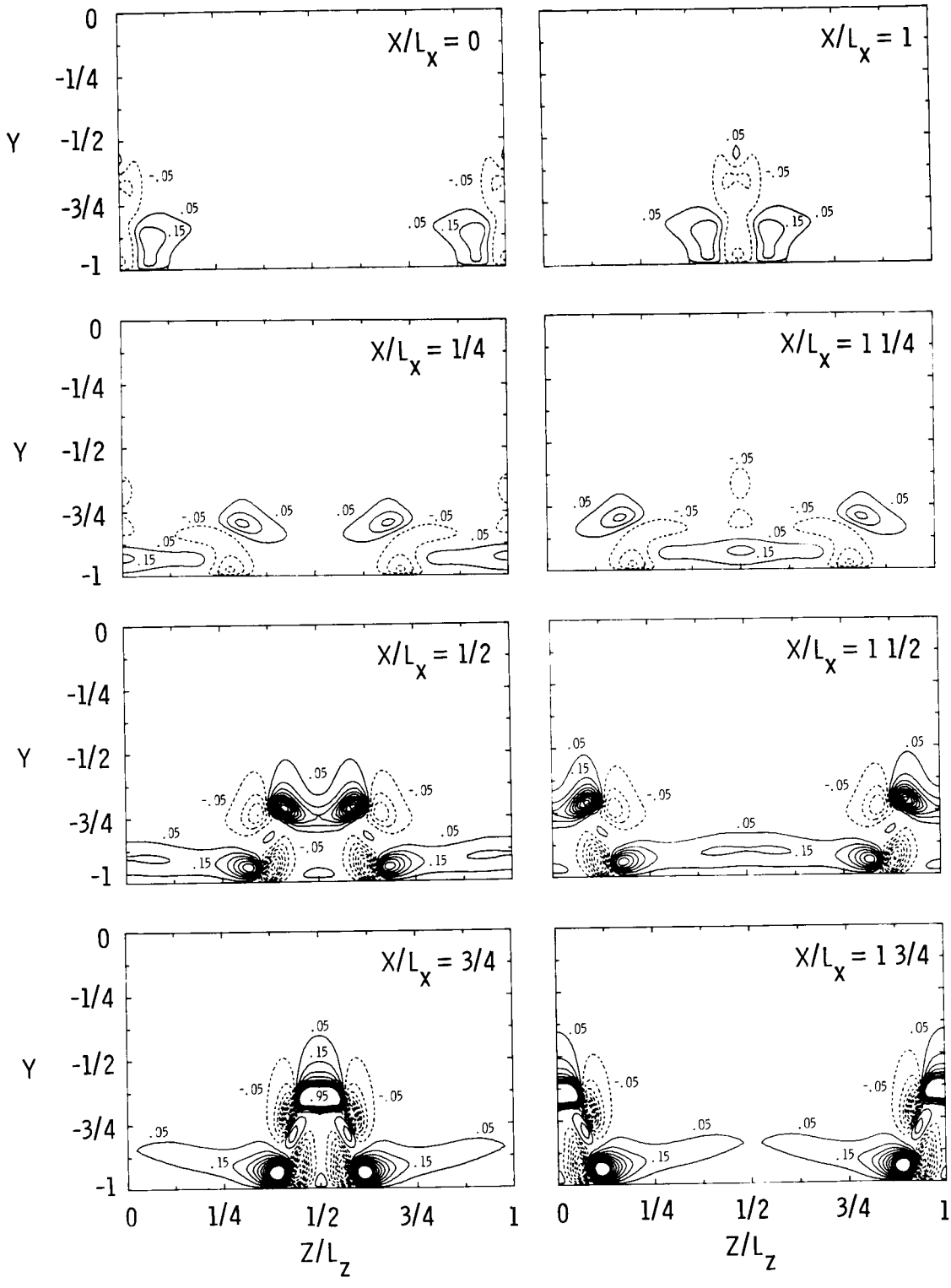

Figure 49. Vortex stretching rate of the $R = 8000$, H-type transition at $t = 184.45$.

Standard Bibliographic Page

1. Report No.	2. Government Accession No.	3. Recipient's Catalog No.
NASA TP-2667		

4. Title and Subtitle	5. Report Date
Numerical Simulation of Channel Flow Transition—Resolution Requirements and Structure of the Hairpin Vortex	April 1987
	6. Performing Organization Code: 505-60-31-05
7. Author(s): Steven E. Krist and Thomas A. Zang	8. Performing Organization Report No.: L-16204
9. Performing Organization Name and Address: NASA Langley Research Center, Hampton, VA 23665-5225	10. Work Unit No.
	11. Contract or Grant No.
12. Sponsoring Agency Name and Address: National Aeronautics and Space Administration, Washington, DC 20546-0001	13. Type of Report and Period Covered: Technical Paper
	14. Sponsoring Agency Code

15. Supplementary Notes

Steven E. Krist: The George Washington University, Joint Institute for Advancement of Flight Sciences, Langley Research Center, Hampton, Virginia.
Thomas A. Zang: Langley Research Center, Hampton, Virginia.

16. Abstract

Three-dimensional, nonlinear numerical simulations are presented for the K-type and H-type transitions in channel flow. The paper has two objectives. The first is to establish firmly the resolution requirements for the various stages in the transition process. Comparisons between calculations on various grids suggest a set of guidelines for maintaining a physically meaningful calculation. The second objective is to map out the structure of the hairpin vortices which arise in K-type and H-type transitions in channel flow, to the latest stage currently feasible. Flow field details are presented for both a subcritical Reynolds number of 1500 and a supercritical Reynolds number of 8000. The diagnostics include illustrations of the vertical shear, streamwise and spanwise vorticity, helicity, vortex stretching, and vortex diffusion fields.

17. Key Words (Suggested by Authors(s))	18. Distribution Statement
Boundary-layer transition Stability Spectral methods	Unclassified—Unlimited Subject Category 02

19. Security Classif.(of this report)	20. Security Classif.(of this page)	21. No. of Pages	22. Price
Unclassified	Unclassified	67	A04

For sale by the National Technical Information Service, Springfield, Virginia 22161

NASA-Langley, 1987